Volume XCIII, No. 2, November 2023

Proceedings of the Danish Society for Structural Science and Engineering

Published by

Danish Society for Structural Science and Engineering

COPENHAGEN 2023

ISSN 1601-6548 (online)

PROCEEDINGS OF THE DANISH SOCIETY FOR STRUCTURAL SCIENCE AND ENGINEERING
Edited and published by the Danish Society for Structural Science and Engineering
Volume 93, No. 2, 2023.

Numerical study of ocean wave behaviour and statistics of the wave induced loads under influence of the direct effect of wind

Viktor Madsen[1,3]
Mathias Renberg[2,3]

Abstract

To design offshore structures to withstand wave-induced loading during their lifetime, statistics of the load are necessary. This is generally obtained by numerical simulations or by more costly experimental investigations of various sea states. However, due to the high degree of nonlinearity of breaking waves, there are still to this day significant uncertainties involved with the estimation of the statistics of wave-induced loads. One of the subjects, that is lacking knowledge is the influence of wind on wave-induced loads.

The present thesis investigates, by aid of numerical simulations in a potential flow model, OceanWave3D, the wind effect on unidirectional, irregular, nonlinear waves. The aim is to estimate how the wave characteristics for extreme wave events are altered under the presence of wind and how the wave-induced load is changed as a result. Simulated surface elevation and load from the numerical model are compared to measurements from previously conducted experiments for two sea states to verify the model.

The effect of wind on the wave-induced load is investigated on a large scale by analysing simulations for three different sea states, each with three different wind speeds. The parameters for the sea states are based on recent observations of extreme seas. The size of the numerical domain is 14,565 x 1 x 90 metres, however, with one sea state having a depth of 300 metres. At least 1000 waves are generated based on the JONSWAP spectrum for each sea state for all wind speeds. Based on this data, exceedance probability curves for crest height, line force, and depth-integrated force are obtained.

The study finds that the wind effect modelled with Jeffreys's sheltering mechanism alters the crest height, steepness, number of breaking waves and thus the wave-induced load. The most extreme wave events, in other words, the waves with the lowest exceedance probability, is seen to be the most influenced.

The initially least steep sea state obtained increased steepness for all wind speeds, while the remaining two sea states decreased or experienced no change. For these two sea-states, the number of breaking waves were, however, increased significantly with the introduction of wind and further increased when the wind speed was increased.

[1] Rambøll A/S
[2] COWI A/S
[3] Aarhus University

For the least steep sea state, the most extreme event of the depth-integrated force was seen to experience an increase of 71 % with the introduction of wind.

1. Introduction

With ever-rising energy demands combined with the goal of the European Commission of climate neutrality by 2050, a large increase in demand for renewable energy has been formed over the last decades, \citet{Boosting97:online}. Offshore wind has excelled by experiencing a tremendous reduction in Levelized Cost of Energy (LCoE), \citet{Oerstedreport}.

During their lifetime, offshore wind turbine structures are likely to be subjected to harsh weather conditions, including strong winds, ice, current, and perhaps most importantly, waves. Extreme sea states can undermine the integrity of offshore structures, to an extent where much attention must be paid to load assessment, \citet{marino2011influence}.

In recent years, there has been an increase in the detection of rogue waves. For this wave type, the classical design tools fail to accurately predict the wave-induced forces, \citet{marino2011influence}. This is partly because the present design practice is based on linear wave theory for irregular waves and regular wave theory for nonlinear waves, \citet{65d4ad2c9c8e4e1d9117e63124e6ce55}. However, numerical solvers, like OceanWave3D, allows for fast computation of fully nonlinear irregular waves.

1.1 Motivation

1.1.1 Renewable energy

The IEA established a new case in their Energy Outlook 202$, called Net Zero Emissions by 2050 (NZE2050). This case proposes that the demand for primary energy is to fall by 17 % between 2019 and 2030, thus reaching levels similar to 2006, \citet{Achievin3:online}. To enable this decrease in primary energy, electrification and efficiency gains combined with behaviour change are essential. Especially the electrification will make up a big part of the transition, as the EU is planning to change the present energy mix by boosting the share from electricity from less than a quarter to at least 50 % by 2050, \citet{Windener52:online}. As a result, the case of NZE2050 predicts an increase in the renewable's share of global electricity supply from 27 % in 2019 to 60 % in 2030. This must, of course, be seen in the light of historically ever-increasing electricity demand on top of the percentage increase. Between 1990 and 2018, the global electricity consumption has risen 227 %, with only the year 2009 not experiencing a growth compared to the year before. Hence, the renewable's share of the global electricity supply is not only covering a more significant percentage but a larger percentage of ever-increasing demand.

The different renewable energy sources within the EU, especially the wind industry, have excelled in the last decades. Currently, the wind is meeting 16 \% of Europe's electricity demand, and the EU Commission expects wind to make up half of Europe's electricity demand by 2050, \citet{Windener52:online}. Particularly offshore wind is expected to grow tremendously. Hence this will be further investigated.

1.1.2 Wind energy

Wind energy presents itself as a cornerstone to this ongoing green transition. The International Energy Agency (IEA) expects wind to become the largest source of power in the EU by 2027, \citet{Windener52:online}. This projection is substantiated by the EU Strategy on Offshore Renewable Energy, presented on the 19th of November 2020. The strategy proposes to increase Europe's offshore wind capacity from its current 12 GW to at least 60 GW by 2030, and to 300 GW by 2050.

While onshore wind still present itself as the cheapest source of power generation in most of Europe, offshore wind has experienced a drastic decrease in terms of LCoE, \citet{Oerstedreport}. This is visualized on Figure 1. A key driver in decreasing the LCoE of offshore wind is increasing installment. Over the past decades, the large increasing volumes of offshore wind construction have been instrumental in driving the overall cost down. Studies suggest that every time the installed capacity of offshore wind is doubled, the LCoE has decreased by 18 %, \citet{Oerstedreport}. The overall trend is seen on Figure 2. The figure shows how the global LCoE has been more than halved within ten years, between 2010 and 2020.

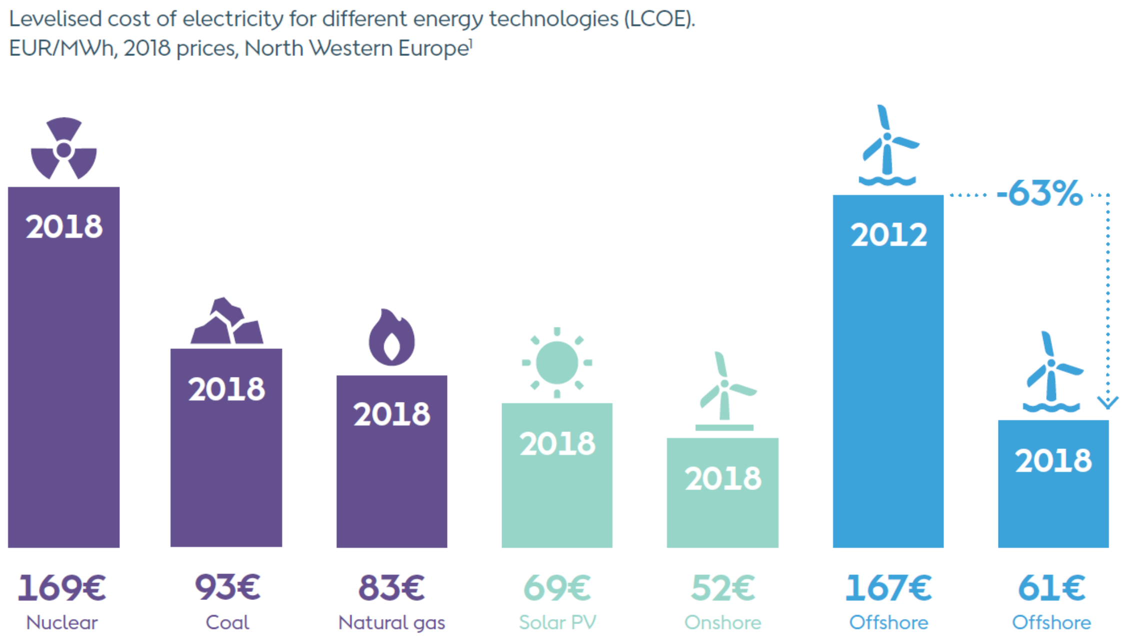

Figure 1: LCoE for different energy technologies. Source: \citet{Oerstedreport}.

On this basis, it is reasonable to expect that offshore wind, for some geographical regions, will overtake onshore wind to become the cheapest form of renewable energy. This is in particular expected for some parts of the North Sea, where the European association, WindEurope, expects that the LCoE for offshore wind will decrease to a level below 50 EUR/MWh by the year 2030. Figure 3 shows the LCoE ranges for the North Sea. The calculation is based on wind speed, distance to shore, and water depth of areas of 5 x 5 kilometres. Further, the calculation is based on 15 MW turbines.

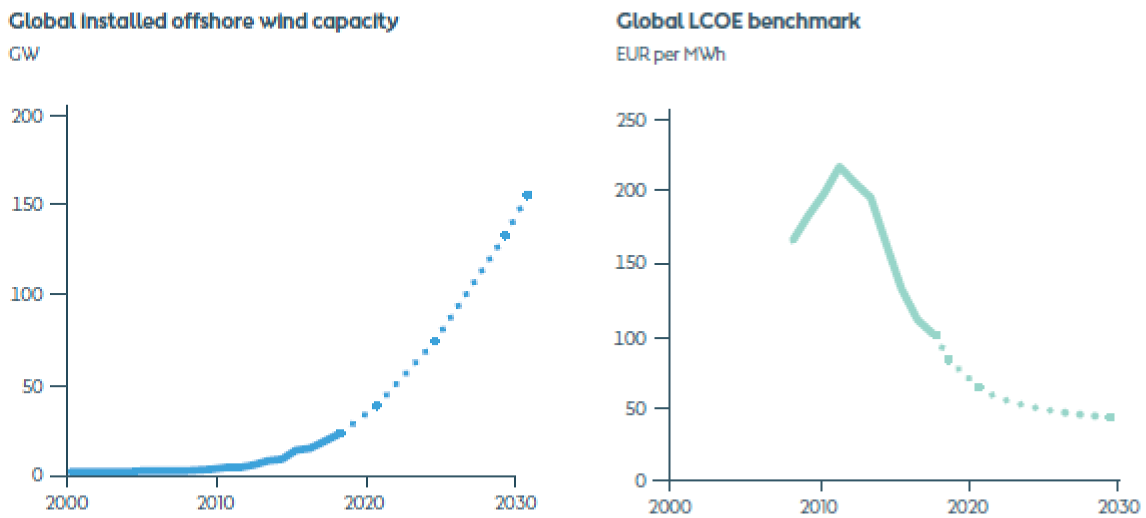

Figure 2: Global scale installed offshore wind capacity and the global LCoE benchmark. Source: \citet{Oerstedreport}.

On the figure, the specification *very low* refers to a LCoE below 50 EUR/MWh in 2030, and *high LCoE* refers to above 80 EUR/MWh in 2030.

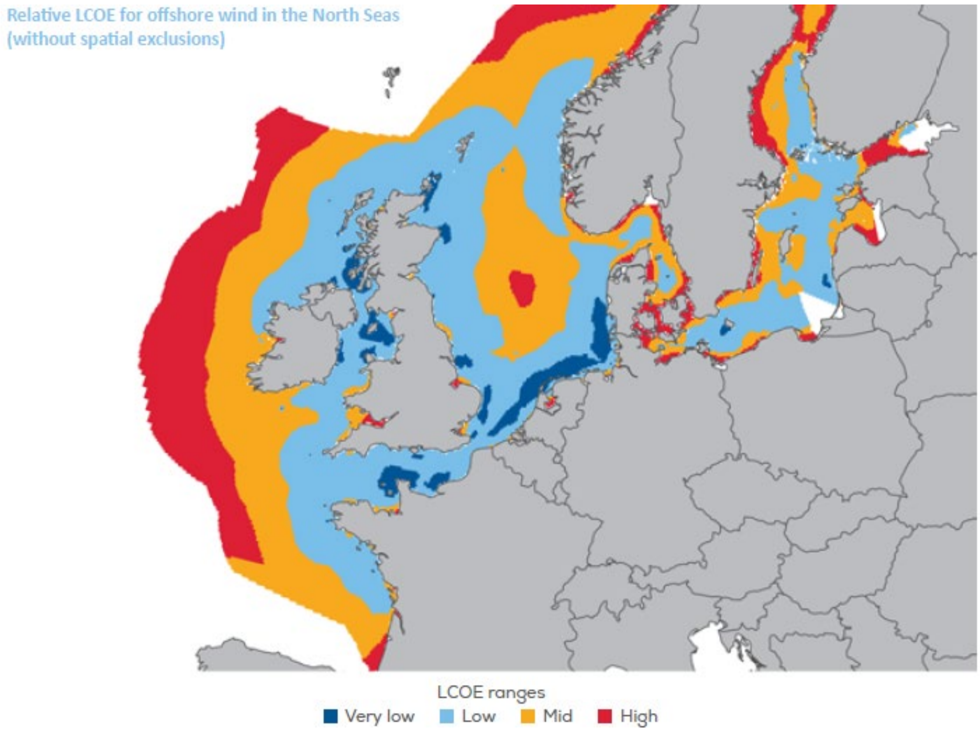

Figure 3: Relative LCoE for offshore wind in the North Seas. Source: \citet{windeuropereport}.

One of the most influential factors in terms of decreasing the LCoE and increasing power production is the size, and thus the capacity, of the wind turbines. The wind turbine industry continues to make more and more powerful wind turbines, with an average increased capacity of 16 % every year since 2014, \citet{windeuropearticle}. Larger wind turbines have a larger capacity. Hence fewer turbines are needed for the same power output, resulting in fewer offshore foundations, which helps drive down the cost of deployment. Figure 4 shows the yearly average of newly installed wind turbine capacities from 2009 to 2019.

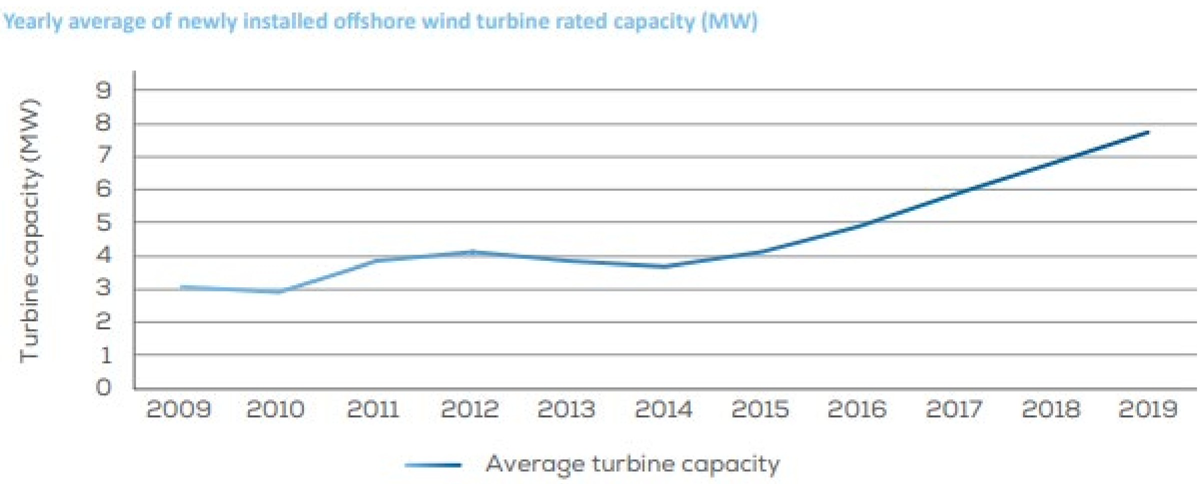

Figure 4: Yearly average of newly installed offshore wind turbine rated capacity in MW Source: \citet{windeuropearticle}.

The trend is expected to continue, at least for the coming years. Especially in the light of a news release from danish based Vestas, planning to launch a new 15 MW wind turbine, for which the company hopes to have a prototype ready for testing as soon as 2022, \citet{VestasCo93:online}.

Another significant trend in the offshore market is the increasing distance from the offshore wind parks to shore. Wind farms are moving further offshore and into deeper waters. The explanation shall be found in more stable wind resources and the depletion of near-shore locations, \citet{windeuropearticle}. Figure 5 shows the development of shore distance and water depth of the offshore wind parks that has been installed between 2000 and 2018. While a constant increase in both depth and shore distance is not present from year to year, the overall tendency of the two is clear. Both shore distance and water depth have significantly increased, with shore distance reaching maximum in 2016 and water depth continuing the increase and showing maximum values for 2018.

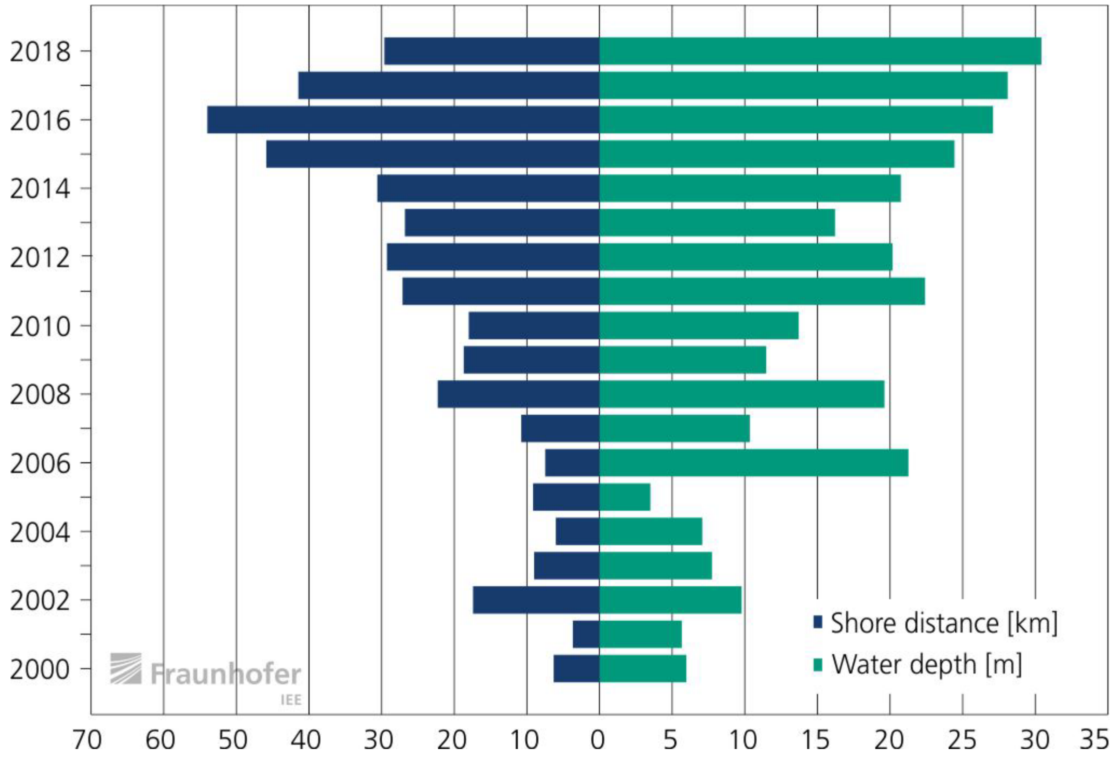

Figure 5: Development of shore distance and water depth of newly installed offshore wind parks. Source: \citet{Distance43:online}.

However, while the overall power output increases due to the more stable wind further offshore, the increased size of the turbines and the installment depth results in the wave forcing becoming more prominent and increasingly influential in the design of the foundations. As the wind turbine tower and foundation increases alongside the water depth, the water column, in which the water exerts force, increases, and so does the moment arm relative to the mudline, \citet{PhDSchl}.

One way to reduce the earlier discussed LCoE of offshore wind is by reducing foundation costs. To do this, the number of uncertainties in the design must be reduced, especially in relation to the hydrodynamic loading. As the water depths of the offshore wind farms increase, the hydrodynamic loads become increasingly important relative to the aerodynamics loads, and the uncertainty concerning the wave-induced loading more and more significant. The following section will discuss the current design practice and the inherent flaws and uncertainties.

1.2 Design Practice

The calculation and design of offshore loads and structures is a complex job, where the design standard tries to provide rules and guidelines for the engineers to follow. \citet{henderson2004hydrodynamic} provides a general overview of the procedures needed to calculate the wave-induced loading from extreme events:

i) Determining the design wave or wave climate
ii) Selecting an appropriate wave load calculation procedure
iii) Determining the effect on the structure

The aim of a standard should be to provide design guidelines for a safe and cost-effective structure. As the wave load from extreme events in some cases can be governing for the offshore structure, \citet{bredmose2016derisk}, any uncertainties in the calculation of the wave-induced loads can contribute negatively to LCoE.

Standard procedures for extreme wave design include the use of regular stream function wave theory. This is usually coupled to a linear representation of the background irregular wave climate, \citet{bredmose2016derisk}. This method is widely used due to its simplicity and fast calculations. However, the method is limited in its accuracy due to assumptions stemming from stream function theory. These assumptions cover the 2D wave motion, flatbed of the ocean bottom, periodicity assumption, and symmetry around the crest. These assumptions can potentially lead to notable discrepancies between the real-life extreme wave events and what is used for design purposes, as extreme waves usually propagate with a non-constant form, have non-symmetric crests, and tend to break. Another suggested method to assess the design load is to use fully nonlinear computations for a specified sea state. The dilemma with this is that the former lacks accuracy and might not capture the actual extent of the highly extreme waves, and the latter is computationally too demanding for engineers to use in practice, \citet{pierella2020derisk}.

This section will give a short overview of the present design practice to understand how design standards define the wave loads, with particular attention paid to wind effects on waves. Here the design practice in mind will be the Det Norske Veritas (DNV), where the focus will be on DNVGL-ST-0437 *Loads and site conditions for wind turbines* (Edition November 2016). The focus within this report will be on the parts of the standard with relation to wave climate and loads. Besides the standard, comments will be made on the DNVGL-RP-C205 *Environmental conditions and environmental loads* (Edition September 2019), RP being short for recommend practice, as DNVGL-ST-0437 refers to this practice.

In DNVGL-ST-0437, the wave load is the second load to be described, where the main load, of course, is the wind. Reading through the standard, it becomes clear that the wind and wave conditions are found individually and then combined through load cases.

When describing the wave climate, several sea states are defined. A sea state is characterized by the wave height, wave period, and direction of the waves. A wave spectrum may also represent a short-term sea state. A wave spectrum can be generated using either site-specific data or a wave spectrum such as the JONSWAP spectrum. For each of the sea states defined in the standard, a concurrent mean wind speed must be determined to combine in the load cases. If site-specific data is available, the data must fulfil a list of basic parameters, and the relation between the wind and waves must be established. Besides this, observations of preferably 10 years or more are required. The standard states that the wave and wind climate are correlated, as the waves usually are wind-generated, which must be accounted for.

Wind-generated waves can be understood as short-period waves. These waves are generated as the wind exceeds a critical value and thus causes ripples in the surface, which over time, and under continued action of wind, will grow in height, length, and period, \citet{svendsen1976hydrodynamics}. In this thesis, the wind-generated waves will be referred to as waves where the indirect effect of wind is included. Using a

JONSWAP spectrum to generate the wave spectrum, the indirect effect of the wind is taken into account, \citet{JCKInPress}.

To calculate the hydrodynamic loads, the standard states that the forces should be calculated using a recognized wave theory, which is selected considering the depth of the site. The selected wave theory is then used to calculate the wave kinematics. The wave kinematics can then be used in a force model, for instance, the Morison equation for slender structural members. For the wave kinematics, the reader is referred to DNVGL-RP-C205. Both the wave kinematics for regular and irregular waves are defined, and to describe these, a relevant wave model must be used. For a regular wave, the kinematics can be obtained solely based on the following wave parameters: period, height, and depth. The irregular waves can be modelled based on a sum of wave components. Here the wave components necessary are related through the dispersion relation. However, when reading through the section it becomes clear that there is no influence from wind included. This is also evident because the wind and wave are split into two sections in the recommended practice and two subsections in the standard.

In conclusion, the direct effect of the wind field on the wave field is not accounted for in the design standard presented above. The JONSWAP spectrum can define the spectral density of the sea state, which is used in the design of offshore structures. To define a JONSWAP spectrum, a period and a wave height are necessary. If site-specific data are utilized instead of the JONSWAP spectrum, the standard suggests using at least 10 years of data from the site. This corresponds to the findings of \citet{jacobsen2005offshore}.

Using either the JONSWAP spectrum or the site-specific data to define a sea state, a representative wave model can be selected with respect to the sea state and water depth. The wave kinematics can be generated from the wave model and then used in a force model to find the hydrodynamic loads, which are then combined with the wind loading on the offshore structure. Therefore, uncertainty could be present in the above-presented design, depending on how the wind field affects the wave field, which this thesis will investigate.

1.3 Extreme wave events

The extreme wave events afflicted on offshore structures are of great interest as the wave load is an essential part of the design. Especially the extreme wave events are of importance as these can be governing for the design of the substructures of offshore wind turbines, \citet{bredmose2016derisk}. Looking at the occurrence of extreme waves, the present design criteria might underestimate the frequency of these events. In 2012 two waves exceeding the existing 10,000 year return period, abnormal event design criteria were documented in the Tyra field for the same storm. These observations triggered an extensive study aiming at mapping the occurrence of these extreme wave events and eventually led to the ceased production of the Tyra East and West fields, \citet{tychsen2016summary}. The study also found that the loads from these extreme events will have an impact on the exceedance probability at 10^{-3} to 10^{-4} rather than for the exceedance probability of 10^{-1}. Hence, these types of events could have a significant impact on the failure mechanisms of offshore structures, \citet{tychsen2016summary}.

Looking at past accidents related to extreme waves, a small number of events have led to fatalities. Such an event happened on the 30th of December in 2015 on the semi-submersible drilling oil rig COSL Innovator, which at the time was operating in the North Sea at the Troll Field working for Statoil. The oil rig was hit by a large wave which led to one fatality and four injuries, \citet{kvitrud2018observed}. As can be read from the article, the accident involving the COSL Innovator is luckily the only recent event that has lead to fatalities. However, the paper has found 29 reported wave accidents involving 17 platforms in the period, 2000-2017. The COSL Innovator was built in 2011 and was certified to operate in the North Sea. As a result of the accident, Statoil made a technical report, \citet{Techreport}, to investigate the weather conditions and parameters on the day of the accident. In the report, the Petroleum Safety Authority Norway (PSA) concludes that the weather conditions on the day of the accident probably were within the limits of the design of the oil rig. This raises the question of whether or not the design used is estimating the waves correctly based on the weather parameters. This accident will be a part of this thesis as a large scale simulation based on the weather conditions reported within \citet{Techreport} will be made. This is done to analyze if the direct influence of the wind could affect the wave load in a way that the present design does not include.

1.4 Effect of wind

Due to the complexity and high degree of nonlinearity of ocean wave behavior, especially concerning wave breaking, the problem of modeling the interaction of wind and ocean waves is still an ongoing research topic that is troubling researchers. Multiple theories have been proposed to describe the phenomenon. One of the broader accepted and used theories is the one presented by John Miles in 1957, \citet{miles1957generation}. The mechanism presented by Miles is a quasi laminar model of the transfer of energy from a turbulent shear flow to a surface wave, \citet{touboul2006freak}. The wave growth is correlated to the shear profile of the wind above by assuming the pressure to vary with the wave slope. The original mechanism has been further studied and improved and is considered an excellent method to couple wind-wave interaction, \citet{touboul2008interaction}.

However, with the increasing research interest in extreme wave events, a different mechanism is widely used. Studies, e.g., \citet{touboul2006freak}, suggest that Jeffreys's sheltering mechanism is more relevant in coupling the wind-wave interaction, especially for waves with unusual characteristics, such as rogue waves. The original mechanism, first presented by Harold Jeffreys in 1925, \citet{jeffreys1925formation}, is based on a difference in pressure between the leeward side and windward faces of the waves induced by airflow separation over steep wave crests, \citet{touboul2008interaction}. Hence, this method assumes that the energy transfer occurs because of airflow separation over steep waves. \citet{reul1999air} investigated the evolution of the instantaneous airflow structure over an unsteady breaking wave by the use of particle image velocimetry (PIV) measurements. It was found that during breaking, the recirculation zone of the separated flow, placed on the leeward side of the wave, takes the form of a well-organized vortex. The phenomenon is seen on Figure 6.

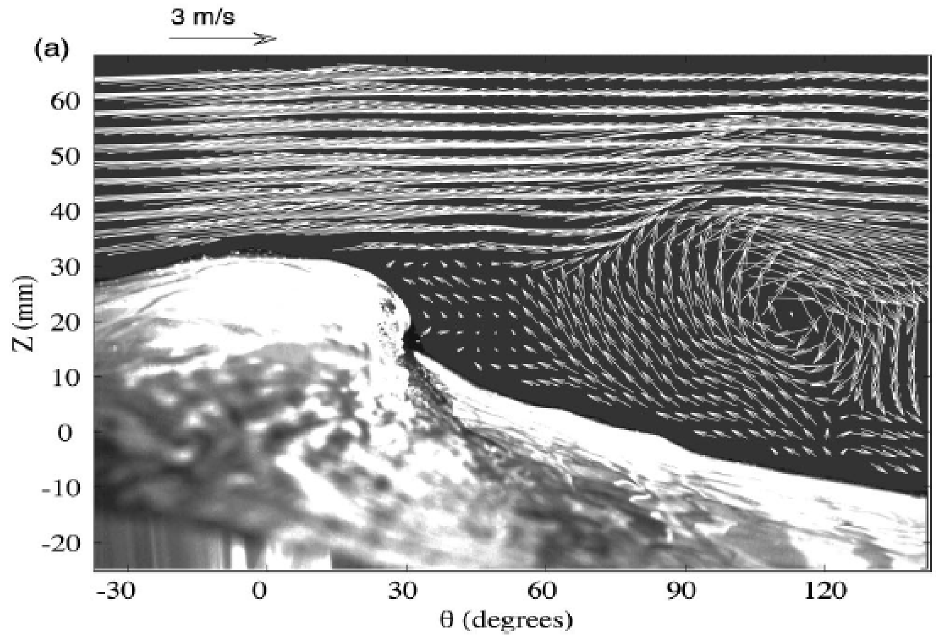

Figure 6: Air-flow instantaneous velocity distributions in the laboratory frame. Source: \citet{reul1999air}.

The experiments also proved the development of a vortex even when the waves were non-breaking, however, at a smaller scale.

The vortex creates a pressure imbalance between the windward and leeward sides of the wave and is the reason behind the form drag, \citet{hasan2018numerical}. The aforementioned PIV study supports the hypothesis of the sheltering mechanism. According to Harold Jeffreys, the pressure at the interface $z = \eta(x,t)$ is related to the local wave slop according to the following expression

$$\mathrm{p}_a = \rho_a s(U - c)^2 \frac{\partial \eta}{\partial x} \tag{1}$$

Where constant s is the sheltering coefficient, U is the wind speed, c is the wave phase velocity, ρ_A is the atmospheric density, and $\partial\eta/\partial x$ is the local spatial slope of the wave, \citet{jeffreys1925formation}.

To implement the mechanism into a numerical model and only apply the effect on steep wave events, the steepness of each waveform must be known. This implementation procedure is in many recent studies called modified Jeffreys's sheltering mechanism, e.g., \citet{chambarel2010generation} and \citet{touboul2008interaction}, and is also the procedure followed within this thesis. Recent studies have investigated the direct effect of wind on ocean waves, particularly extreme wave events, using a modified Jeffreys's sheltering mechanism. Based on both experimental and numerical investigations, numerous studies reach multiple similar conclusions regarding the phenomenon.

\citet{touboul2006freak} carried out numerical as well as experimental investigations on the direct effect of wind on a freak wave event generated by the use of a dispersive spatio-temporal mechanism. They found that the focus point of the generated wave group is shifted downstream while the height of the extreme waves is increased. Another recurring result during research on the phenomenon is the change in the duration of the extreme wave event. \citet{kharif2008influence} carried out experiments on the formation of extreme waves in the Large Air-Sea Interaction Facility in Marseille, France. Further, they carried out corresponding numerical simulations, which showed a qualitatively good agreement with those obtained experimentally. Results showed that the presence of wind modifies the wave group's kinematics and dynamics characteristics. One of the changes is the time duration of the extreme wave event, which seems to be sustained for a longer time. Their findings showed them an increase in time of a factor of 1.75.

Similar numerical investigations were carried out by \citet{chambarel2010generation}. To explore the direct effect of wind, they ran simulations of wave packets propagating with and without wind, enabling investigation of the dynamic differences. Besides rediscovering that wind increases the amplitude and lifetime of the highest waves and shift down the focus point of the wave group, they found that the introduction of wind led to an increase in the speed of the overturning crest of the waves. This result was illustrated by the following Figure 7. The resulting plots are shown for a numerical simulation with wind speed of U = 10 m/s and a critical wave slope of $\partial\eta/\partial x = 0.25$.

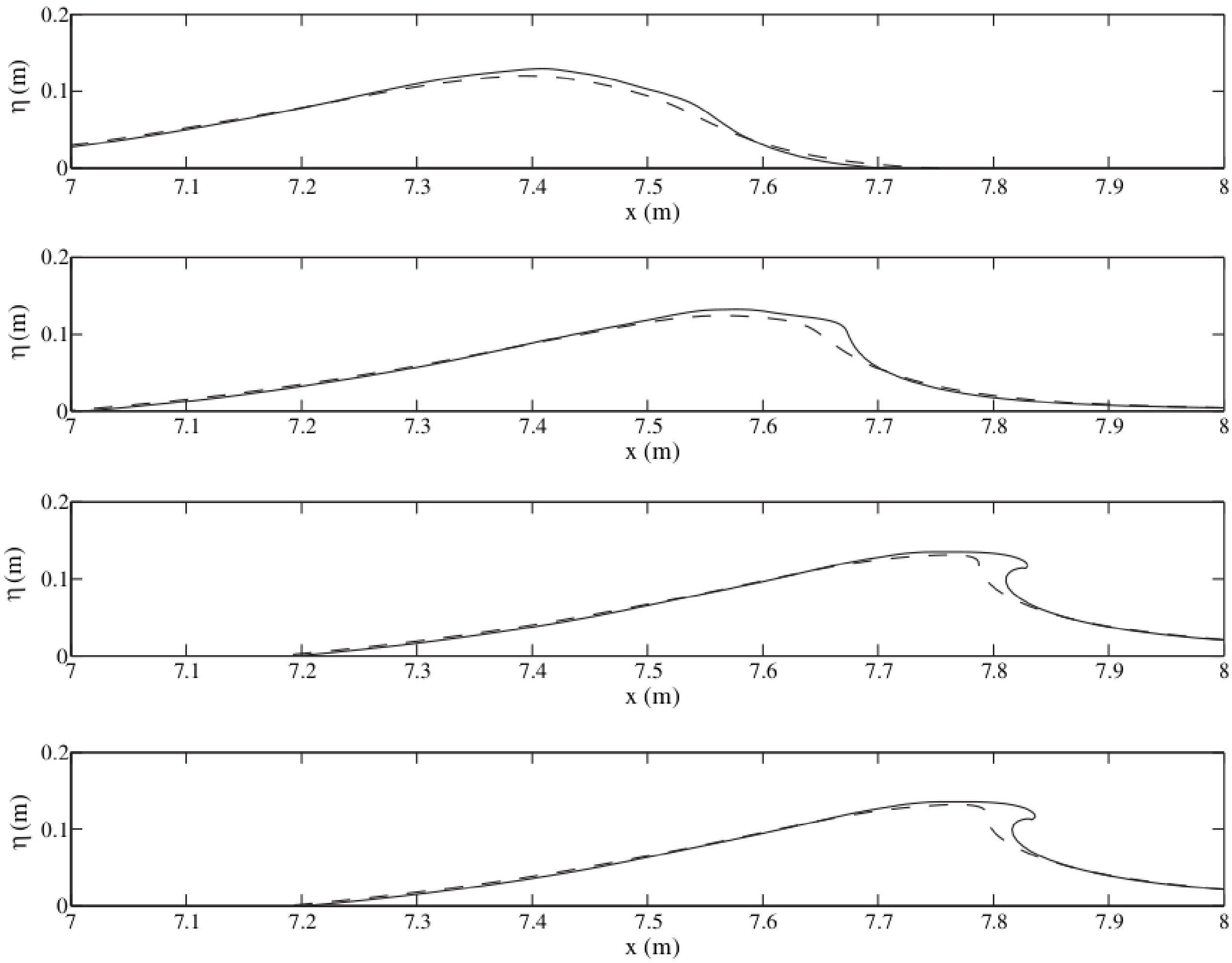

Figure 7: Spatio-temporal evolution of breaking waves with wind (solid line) and without wind (dashed line). Source: \citet{chambarel2010generation}.

While Figure 7 shows a slight increase in wave height for the case with wind, some studies suggest that for breaking waves, stronger winds may lead to lower wave crests and wave heights, \citet{yan2010numerical}. The reason for this is most likely because wave breaking caused by stronger winds ends up dissipating a more significant portion of energy than for lower wind speeds. However, for steep initially non-breaking waves, the wind might be capable of increasing the surface elevation and the wave-induced load, \citet{kristoffersen2018preliminary}. In the findings of \citet{kristoffersen2018preliminary}, numerical simulations show that for stronger winds, the surface elevation might be decreased due to activation of the breaking filter in OceanWave3D, thus resulting in lower surface elevation but obviously with an increased wave load due to breaking.

This latter mentioned study is a rare example of investigations towards the wind effect on wave-induced loads and how it alters the load statistics. As stated in the previous sections, current design methods are potentially not to a sufficient level accounting for the altered load stemming from the direct effect of wind on ocean waves. This is further substantiated by studies investigating extreme wave events and the impact it has on structural reliability, \citet{tychsen2016summary}. \citet{tychsen2016summary} presents a similar conclusion to that Section 1.2, namely that existing industry methods do not correctly estimate the wave loading, and thus the failure probability for collapse mechanisms. Specifically, the study states that the present conditions of the Tyra structures are outside of the acceptance criteria for manned operation.\\

Some current studies are working on investigating the influence of the direct effect of wind on the wave-induced load and the statistics hereof, \citet{kristoffersen2018preliminary}. The experimental investigations by \citet{JCKInPress} seek to enlighten whether airflow separation and vortexes in the wind field alter the physical properties of the waves, such as the steepness, number of breaking waves, and thus the depth-integrated force. This is done by conducting wave basin testing for unidirectional irregular waves in the Large Air-Sea Interface Facility at the Luminy University of Marseille, France. Through analysis of 4 sea states, the study found that the front steepness of the waves was increased with the introduction of wind and continued to increase when increasing the mean wind speed. Further, an important finding was that the detection of breaking waves was increased with the wind applied to the wave groups. Moreover, the experimental results showed that the tail of the exceedance probability curve for depth-integrated force showed larger values when the wind was present for some of the sea states.

1.5 Aim and scope of the thesis

The overall aim is to specify tendencies as accurately as possible and eventually come up with estimates of how the wave characteristics and the wave-induced load for extreme wave events are altered under the presence of a wind field. The study seeks to describe the effect of the local wind, which eventually will result in a more accurate definition of wave-induced loading of extreme sea states, which potentially could help the offshore industry as a whole. The study will investigate, by means of numerical simulations in open source software, OceanWave3D, the wind's effect on unidirectional irregular waves and how the wave characteristics are affected. Characteristics such as crest height, significant wave height, and steepness are investigated, but perhaps most importantly, great attention will be paid to the wave-induced load. Various relevant statistical tools will be utilized to reveal the scope of the wind effect accurately. In particular, exceedance probability curves will be used, as it is the waves with lower exceedance probabilities in which the wave-induced loading has the potential of governing the load statistics and thus the reliability of offshore structures.

The works of this thesis are subdivided into two overall stages. The first stage includes numerical simulations based on the experimental setup of \citet{JCKInPress}, to verify the correlation between experiments and the numerical solver OceanWave3D. The second stage of the thesis aims at investigating the topic by adopting a large scale numerical approach, i.e., simulations with a domain length of several kilometres and a depth of multiple hundreds of metres, will be carried out. This is done to investigate tendencies on large scale simulations resembling real-life extreme wave events.

2. OceanWave3D

This chapter will present a brief description of the OceanWave3D model, with the background for the model, a short explanation of the underlying hydrodynamic model, the wind application, and some of the limitations of the model, as well as a listing of the hardware components for the computers used to run the simulations in OceanWave3D.

2.1 Motivation

In 1976, Peregrine derived a first Boussinesq model for efficient simulation of free surface flow over variable depth in coastal and offshore engineering, however only accurate for shallow waters, \citet{AllanPEn65:online}. Later on, this was extended to cover deep waters, which led to the development of several modified forms of Boussinesq-type equations, \citet{AllanPEn65:online}. Based on these findings \citet{engsig2009efficient} developed a robust and efficient flexible-order finite-difference model based on a fully nonlinear and dispersive potential flow model, hereafter referred to as the OceanWave3D model.

The open-source OceanWave3D model has been developed at the Technical University of Denmark since 2006 as a part of an ongoing research effort with Associate Professor Allan P. Engsig-Karup. The OceanWave3D model can be viewed as a discrete free surface model of the fully nonlinear and dispersive potential flow equations. The range of applications is only limited by truncation errors related to the discretization procedure and limitations due to underlying assumptions stemming from potential flow theory. The model was constructed and further developed to enable fast computations for arbitrarily sized domains, including large scale problems. Significant focus has been put on the efficiency and robustness of the model.

2.2 Version

The OceanWave3D software exist in different versions, Fortran 90 and C++, whereas the present study is using the former, running on the Linux distribution, Ubuntu.

As the software is open source, a free version of the program can be downloaded and installed from https://github.com/apengsigkarup/OceanWave3D-Fortran90. However, in this version of the model, the transfer of energy between the wind and the waves is not considered. The present study uses a version of this program, which can take this energy transfer into consideration. This is implemented by incorporating a modified Jeffreys's sheltering mechanism to the model, as done in \citet{kristoffersen2018preliminary}.

2.3 Hydrodynamic model

The OceanWave3D model is employed to calculate the wave kinematics at all desired locations. The model solves the three-dimensional Laplace equation for the velocity potential, Φ, and the free surface elevation, η. The model uses a flexible order finite difference method to discretize the continuous derivatives. A structured grid is employed, enabling non-uniform grid spacing, thus allowing for the clustering of grid points. Nonlinear boundary conditions are applied at the free surface and impermeability conditions at the seabed. Equations describing the above are:

$$\frac{\partial^2 \Phi}{\partial x^2}+\frac{\partial^2 \Phi}{\partial y^2}+\frac{\partial^2 \Phi}{\partial z^2}=0, \text{ for } -h \leq z < \eta \tag{2}$$

For every time step, surface elevation, η, and velocity potential, Φ, is calculated by applying dynamic and kinematic boundary conditions at the free surface:

$$\frac{\partial \eta}{\partial t}=\frac{\partial \Phi}{\partial z}-\frac{\partial \Phi}{\partial x}\frac{\partial \eta}{\partial x}-\frac{\partial \Phi}{\partial y}\frac{\partial \eta}{\partial y} \quad \text{for } z=\eta \tag{3}$$

$$\frac{\partial \Phi}{\partial z}=-\frac{\nabla\Phi\cdot\nabla\Phi}{2}-g\eta=0, \quad \text{for } z=\eta \tag{4}$$

To find the vertical velocity $w=\partial\Phi/\partial z$ at the free surface and solve the equations forward in time, requires solving the Laplace equation in the fluid domain with a known velocity potential and surface elevation together with the impermeability conditions at seabed:

$$\frac{\partial \Phi}{\partial z}=-\frac{\partial h}{\partial x}\frac{\partial \Phi}{\partial x}-\frac{\partial h}{\partial x}\frac{\partial \Phi}{\partial x} \quad \text{for } z=-h \tag{5}$$

As the free surface is a time-dependant moving boundary, the physical z-coordinate of the grid points change with time. Therefore it is convenient to make a change of variable in the vertical direction which will map the time-varying solution to a time-invariant domain, \citet{engsig2009efficient}. Recalculation is thus avoided, by use of the a sigma-coordinate transformation, that changes the (x,y,z) coordinate system to a (x,y,σ) system. The vertical coordinate, σ, is given by:

$$\sigma \equiv \frac{z+h(x,y)}{\eta(x,y,t)+h(x,y)} \in [0,1] \tag{6}$$

Once the potential is solved, the velocities and accelerations can be found by differentiating the potential in different directions.

Clustered grid in the vertical direction is utilized due to the findings of \citet{engsig2009efficient}, where it was found to bring larger convergence when compared to an evenly spaced grid. Further in the study of \citet{engsig2009efficient}, an alternative method to satisfy the boundary conditions along the solid boundary was presented. The alternative method is based on the insertion of computational points outside of the fluid domain, so-called *ghost* points. These fictitious points are used to express the derivatives at the boundary, which are used to satisfy the impermeability condition. By then solving the boundary condition equations explicitly, the ghost point contributions are removed from the Laplace equation at the boundary. Hence, both the Laplace equation and boundary condition are satisfied at the same time. Waves are generated at the domain's left boundary, and OceanWave3D can implement different wave generation techniques. For example, it is, e.g., possible to impose regular linear waves using the monochromatic setting or generate linear irregular waves based on the JONSWAP spectrum.

The use of nonlinear boundary conditions generates nonlinear waves. The nonlinear terms are turned on or off in the equations based on the desired wave type. To the right in the domain, waves are 'absorbed' numerically. OceanWave3D implements a linear friction damping applied to the tangential velocity, dissipating energy and minimizing reflections, \citet{pierella2020derisk}.

To prevent instabilities from near-breaking waves and overcome the fact that only one point can be simulated at each time step, OceanWave3D utilizes a breaking filter to simulate breaking waves. The breaking filter is based on a compact spatial Savitzky-Golay filter. The breaking filter dissipates energy whenever the downward particle acceleration exceeds the input value, β, multiplied by the gravitational constant. In the study by \citet{pierella2020derisk}, this value is chosen to 0.5 as investigations towards the recreation of experiment results showed good agreement with this value. Furthermore, previous findings have demonstrated well-correlated simulations and experiments with this value, hence β = 0.5 will also be used in the present study.

If the calculated downward acceleration exceeds the threshold at a certain point, the model smooths a 10-point region centered at the point with a 3-point filter, where the i^{th} free surface elevation is computed as, \citet{pierella2020derisk}:

$$\eta_i = 0.25\eta_{i-1} + 0.5\eta_i + 0.25\eta_{i+1} \tag{7}$$

The surface conditions are evolved in time by use of a classical fourth order Runge-Kutta time-stepping scheme. In relation to this method, the model has incorporated the Courant-Friedrichs-Lewy (CFL) condition. The CFL condition is often employed in numerical investigations involving explicit time integration tasks, as it ensures coherency between space- and time-domain. More specifically, the condition relates the length of the time-stepping to the spatial interval length and the maximum speed with which the information, in this case, the waves, travel. Hence, to accurately compute the kinematics of the waves for discrete time steps, it must be ensured that the duration of these time steps is smaller than the time in which the wave travels between two adjacent spatial points. This is achieved by ensuring a maximum Courant number of 1. This relation is easily deduced from the one-dimensional form of the condition:

$$C = \frac{c \cdot \Delta t}{\Delta x} \tag{8}$$

C is the dimensionless Courant number, Δt is the time step, Δx is the length interval, and c is the celerity.

2.4 Wind application

The original OceanWave3D model is extended by the possibility of enabling wind pressure. Practically speaking, this is seen in terms of an extra input line in the OceanWave3D input file. The wind pressure is modeled by the use of Jeffreys's sheltering mechanism, as mentioned in Section 1. According to \citet{jeffreys1925formation}, the pressure at the interface $z = \eta(x, t)$ is related to the local wave slope according to the following expression:

$$\mathrm{p}_a = \rho_a s(U - c)^2 \frac{\partial \eta}{\partial x} \tag{9}$$

Where constant s is the sheltering coefficient, U is the wind speed, c is the wave phase velocity, and ρ_a is the atmospheric density. $\partial\eta/\partial x$ refers to the local wave slope. To only apply the effect on steep wave events, the steepness of each waveform must be known. This is easily made possible by introducing a threshold of the local wave slope, which will activate the mechanism as soon as the threshold is exceeded. The mechanism is applied to the full extent of the wave, i.e., between two successive zero-up crossings, which hold one or more values that exceed the defined threshold. This is done as the pressure drag is produced by the attached vortex on the leeward side, \citet{hasan2018numerical}. The threshold value used in this thesis is based on findings in \citet{kharif2008influence}. Here they were able to register airflow separation for values exceeding 0.35. Furthermore, the wind was reported to be effective when the local slope is around 0.35. However, this study found that when running simulations on model scale with a threshold for the spatial slope of 0.35, β = 0.5 as the input value for the breaking filter and a mean wind speed of 5.5 m/s, the solution became unstable. Consequently, a sensitivity study was carried out to investigate what value should be used for the threshold instead. This resulted in a value of 0.4.

2.5 Application and limitation

As previously mentioned, OceanWave3D is a finite difference-based solver. It maps the time-varying physical domain into a time-invariant boundary-fitted computational domain to obtain time-constant discrete differential operators weighted by time-dependent coefficients.

The model is based on a Eulerian description of the flow. The Eulerian method is applied to answer what occurs at a given point in space occupied by fluid in motion. This is a crucial difference between OceanWave3D and computational fluid dynamics (CFD) and introduces one of the main limitations to the software, namely that only one point can be simulated at each time step. In other words, the solution of the surface elevation is a single-valued function of the horizontal coordinate. Therefore, the program cannot simulate an overturning wave, like CFD would be able to. This is the most vital aspect to be aware of when applying the model.

To accommodate for the above, an earlier mentioned breaking filter is applied to handle near-breaking waves. While the usage of a breaking filter is quite efficient, it does pose some complications. First, there is a risk of the potential solver becoming unstable before the wave overturns. This could, among other cases, happen if the breaking filter is turned off, and a wind field that transfers energy to the waves is simulated, resulting in an increased surface elevation until the solution becomes unstable. Another shortcoming of the numerical model structure with the incorporated breaking filter is that the overturning process of breaking waves itself is not modelled. For waves close to breaking, the model will start to dissipate energy upon exceeding the defined threshold. This introduces uncertainties in the process related to breaking. While this is not a physical approach to the problem of wave breaking, it does enable an effortless solution. It turns out that no study has proved a "correct" way to overcome the problem of limiting the near-breaking waves from a potential flow solver, \citet{PhDSchl}.

In relation to implementing Jeffreys's sheltering mechanism, a threshold for the spatial slope of the surface elevation, η, must be defined. For this study, the model posed some problems, as it was not possible to run simulations with a slope coefficient of 0.35, breaking filter at 0.5 and wind speed 5.5 m/s, as the solver would become unstable. Here the numerical stability of the model presents itself as a limitation to the present study. However, for this thesis, OceanWave3D presents many strong qualities. The model serves as a highly efficient tool for accurate numerical wave tank experiments. Simulating thousands of waves over large domains, like done in this thesis, is done rapidly and with a high degree of accuracy in predicting kinematics from the seabed to the free surface. This would not have been possible to do with CFD within the time frame and not without a requirement of extremely high processing time and power.

In terms of inaccuracy regarding the OceanWave3D model, this is introduced with the underlying assumptions stemming from potential flow theory. Potential flow is an idealized model of fluid flow that occurs in the case of the flow being both incompressible, inviscid, and irrotational. Additionally, the use of potential flow theory will introduce a truncation error, which can limit the application range of the program. Furthermore, as with all other discretization procedures in numerical tasks, a slight truncation error is introduced due to the discretization. To compare, CFD also deals with limitations and inaccuracies. Upon using CFD, one is solving a set of coupled partial differential equations (PDE), that if wrong values are provided, the solution will be inaccurate. The boundary conditions and initial conditions are an instance of the exact solution in time and space at those locations.

Although the model is highly efficient and fast in terms of computations, the computational time is for the present study still the most significant limitation. This applies to the large-scale part of the thesis work. In Section 4 run time for different discretization will be presented and here, the computational time is one of the vital parameters that influence the decision making in terms of grid size and time stepping of the large-scale domain.

2.6 Hardware specifications

OceanWave3D has, for simulations within the works of this thesis, been installed on 6 different computers. As these 6 computers do not have the same hardware specifications, simulations can not be directly compared in computation time. To create an overview of the different computers and provide information to potential future researchers, the following Table is created. The list is sorted by the fastest computers first, based on a test input file designed for the purpose. The run time has then been indexed relative to the fastest computer. The 'GPU' column in the table refers to whether or not the computer has a dedicated graphics processing unit. Further, it is essential to note that while all computers are running the OceanWave3D model on the same version of the Linux distribution, Ubuntu, computer number 5 and 6 do not have the operating system installed on the internal hard drive. Instead, an external drive is used to boot from, partly explaining the increased computational time.

Table 1: Overview of hardware specifications for the 6 computers used to run simulations.

		Specifications			
#	**CPU**	**Cores [-]**	**Ram [GB]**	**GPU**	**Speed factor**
1	i7 7820 @ 2.9 Ghz	8	32	Geforce GTX 940 MX	1.00
2	i5 8400 @ 2.8 Ghz	6	8	Geforce GTX 1060	1.03
3	i7 2860 @ 2.5 Ghz	8	16	Quadro 2000M	1.18
4	i7 6600 @ 2.6 Ghz	4	12	Quadro 2000M	1.20
5	i5 6300 @ 2.3 Ghz	4	8	Geforce 950M	1.23
6	i7 6820 @ 2.7 Ghz	8	16	Geforce GTX 940 MX	1.65

3. Model Scale

This part of the thesis aims to replicate experimental results from experiments carried out at the Large Air-Sea Interface Facility at Luminy University, Marseille. The experiments were conducted to investigate the effect of wind on the wave-induced loads, \citet{JCKInPress}. The comparison is made to validate the numerical model in OceanWave3D. The test facility consists of a 40 x 2.6 x 0.9 m wave tank with a 40 x 3.2 x 1.5 m airflow channel. The airflow channel is supplied with a turbulent grid, which uses convergent and divergent sections to create a homogeneous flow at the area near the wave paddles. This helps to achieve a natural development of the air boundary layer at the water surface. At one end of the tank, the waves are generated, and on the opposite end, an absorbing beach is present. The description of the experiment is from \citet{JCKInPress}. The irregular waves in the tests were generated from a JONSWAP spectrum, with peak frequencies in the range of 0.8 and 1.05 Hz. A sketch of the test setup is seen on Figure 8. The figure indicates the position of wave paddles, wave gauges, hotwire, the model itself as well as the absorbing beach.

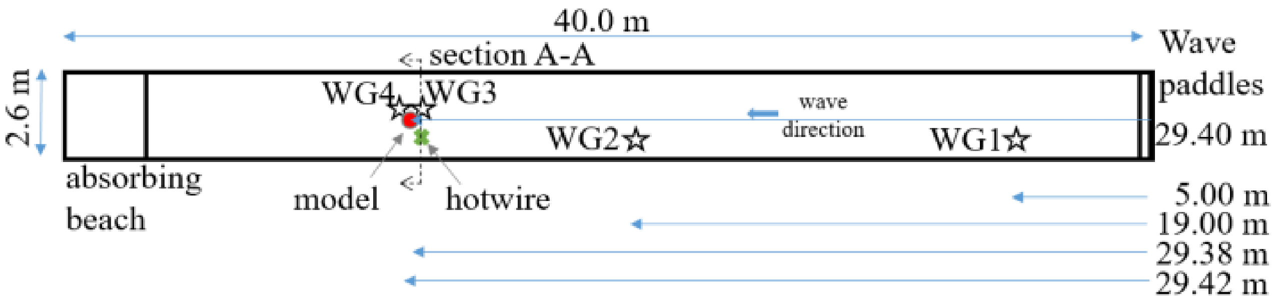

Figure 8: Test setup for experiments at the Large Air-Sea Interface Facility at Luminy University, Marseille, \citet{JCKInPress}.

Four different sea states were considered in the experiments, which each was carried out for three different wind velocities, namely W = 0, 5.5, and 7 m/s. Results have been provided to the current thesis in the form of surface elevation values for these sea states with varying wind velocities. For each sea state, 10 tests were run for each wind speed. Each test contained roughly 1,000 waves such that a total of 10,000 waves were obtained for each wind speed in each sea state. In the analysis of the experiment, \citet{JCKInPress} found that the front steepness of the waves and the number of breaking waves were increased when the wind was introduced, however, the force from the waves was only increased in some of the sea states.

For this thesis, only sea states A and B will be considered to validate the numerical model. Each sea state will be considered with a wind speed of 0.0 and 5.5 m/s. Drawing the diagram showing the validity of wave theories by \citet{le2013introduction} and plotting the two sea states will indicate the overall severity of the sea states. This is seen in Figure 9. In the diagram the non-dimensional values of $h/g\mathrm{T}^2$ and $H/g\mathrm{T}^2$ is plotted along the x and y-axis respectively. Red crosses indicate water depth, h, significant wave height, H_s, and peak period, T_p. Magenta dots indicate h, T_p and theoretical maximum wave height for 10,000 waves, $H_{10{,}000}$. For this thesis, only the final domain is described; the discretization of the domain will be $\{N_x, N_y, N_z\} = \{801,1,20\}$, with a time increment of $dt = 0.015625\ s$ and number of time steps of $N_t = 71042$.

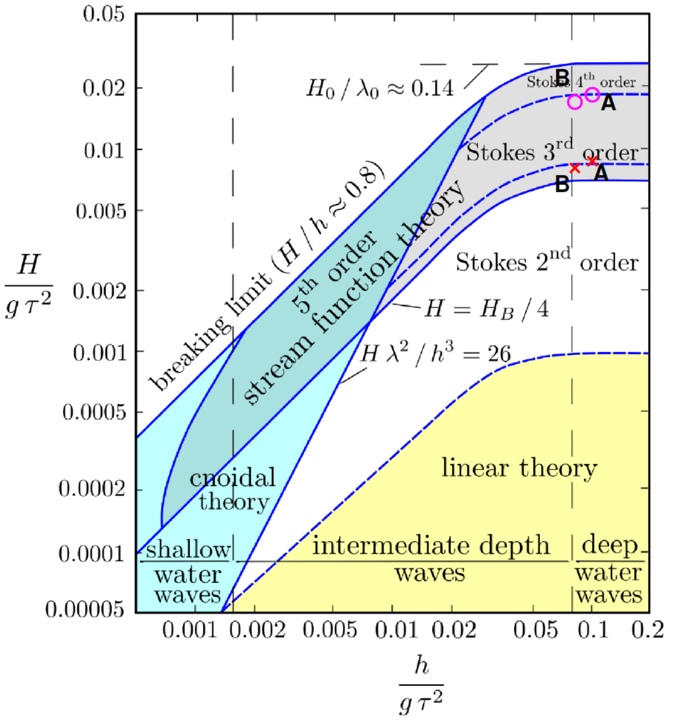

Figure 9: Diagram showing validity of the wave theories, \citet{le2013introduction}. Red crosses indicate water depth, h, significant wave height, H_s, and peak period, T_p. Magenta dots indicate h, T_p and theoretical maximum wave height for 10,000 waves, $H_{10,000}$. A and B indicate the two sea states.

3.1 Validation of the numerical model

For each test from the experiment, a simulation will be made. For each simulation, the measured surface elevation for the tests without wind, from wave gauge 1 is down sampled and used as input in the simulation. The wave kinematics from the simulation is then taken out at a later x value and compared to the measured experimental data from wave gauge 3. When running simulations for the experiments with wind, the measured surface elevation from wave gauge 1 without wind is used as input. However, the energy transfer from the wind is enabled, with a threshold value of 0.4. Two of the simulations became unstable with this threshold. To remain within the threshold described in \citet{kharif2008influence} (0.3-0.4), the first 10 seconds of the simulations were removed. 1000 waves were still obtained for the two simulations.

3.1.1 Spatial and temporal shift of the reference point

Before comparing the statistics of the crest and depth-integrated force between the experimental data and the numerical data, it is investigated whether the simulation introduces a spatial or temporal shift. This investigation is carried out by obtaining the wave kinematics from multiple locations before and after wave gauge 3. The correlation between the experimental data and the numerical data will be calculated, and the best-correlated location and corresponding time shift will be based on the highest correlation values. Here both the correlation values for surface elevation as well as force will be considered.

The correlation values for the surface elevation is found in Table 2. Here each row in the table represents a location, while each column represents a time shift. The correlation values reported in the table is the mean values for all tests in both sea states without wind, thus averaging over a total of 20 values.

Table 2: Correlation values for surface elevation with both spatial and temporal shift.

x values [m]	Time shift factors of dt = 0.015625 [s]							
	0	3	6	9	12	15	18	21
29.10	-0.1756	-0.3899	-0.5677	-0.6950	-0.7629	-0.7677	-0.7111	-0.5995
29.15	-0.0195	-0.2497	-0.4554	-0.6196	-0.7296	-0.7778	-0.7621	-0.6856
29.20	0.1400	-0.0962	-0.3218	-0.5171	-0.6662	-0.7577	-0.7855	-0.7492
29.25	0.2951	0.0638	-0.1719	-0.3908	-0.5742	-0.7069	-0.7791	-0.7862
29.30	0.4378	0.2221	-0.0130	-0.2461	-0.4564	-0.626	-0.7412	-0.7934
29.35	0.5604	0.3705	0.1470	-0.0897	-0.3182	-0.5181	-0.6725	-0.7689
29.40	0.6570	0.5016	0.3003	0.0711	-0.1651	-0.3869	-0.5747	-0.7127
29.45	0.7233	0.6088	0.4387	0.2277	-0.0053	-0.2389	-0.4522	-0.6264
29.50	0.7572	0.6870	0.5550	0.3717	0.1530	-0.0814	-0.3104	-0.5133
29.55	0.7586	0.7340	0.6447	0.4967	0.3020	0.0777	-0.1563	-0.3785
29.60	0.7302	0.7492	0.7043	0.5968	0.4343	0.2301	0.0020	-0.2295

By looking at the table, it is clear the correlation values do not indicate a time shift. However, a spatial shift is indicated. For the surface elevation the best correlated location is found at x = 29.55 m and x = 29.5 m, where 29.5 only differs 0.18 % compared to 29.55. In general, the correlation is increasing while the location of the reference point in the numerical tank is shifted downstream when compared to the experimental reference point of 29.38 metres.

In Table 3, the correlation values from the depth-integrated force is shown. The rows are representing different locations, while the columns are representing time shifts. The correlation values in the table are mean values for sea states A and B for all tests without wind, averaging over 20 values.

Table 3: Correlation values for depth-integrated force with both spatial and temporal shift.

x values [m]	Time shift factors of dt = 0.015625 [s]							
	0	3	6	9	12	15	18	21
29.10	0.1312	-0.1027	-0.3243	-0.5152	-0.6602	-0.7484	-0.7742	-0.7373
29.15	0.2858	0.0544	-0.1789	-0.3940	-0.5729	-0.7015	-0.7704	-0.7755
29.20	0.4309	0.2123	-0.0228	-0.2536	-0.4602	-0.6256	-0.7367	-0.7855
29.25	0.5588	0.3632	0.1369	-0.0998	-0.3260	-0.5223	-0.6726	-0.7651
29.30	0.6628	0.4990	0.2919	0.0599	-0.1762	-0.3958	-0.5800	-0.7138
29.35	0.7383	0. 6137	0. 4352	0. 2184	-0.0172	-0.2508	-0.4618	-0.6325
29.40	0.7821	0.7015	0.5593	0.3676	0.1431	-0.0943	-0.3233	-0.5241
29.45	0.7923	0.7582	0.6581	0.4998	0.2966	0.0665	-0.1703	-0.3928
29.50	0.7702	0.7824	0.7276	0.6091	0.4361	0.2234	-0.0103	-0.2446
29.55	0.7184	0.7745	0.7656	0.6907	0.5548	0.3687	0.1483	-0.0871
29.60	0.6407	0.7359	0.7713	0.7416	0.6474	0.4956	0.2982	0.0723

Here, some of the correlation values indicate a time shift, where the correlation value increases for the last three locations. The highest correlation is found at x = 29.45 m followed by x = 29.40 m, where 29.4 is 1.29 % lower than 29.45. Thus looking at the correlation values for the force, there are still indications of the reference point being shifted downstream. However, a smaller shift than for the surface elevation.

The best location on which the following analysis will be based is chosen considering both the correlation of surface elevation and force. Here the best location is x = 29.5 m. This value is chosen as it is the second-highest value for surface elevation and the third largest for depth-integrated force. For the force, a time shift of three times the time increment would increase the depth-integrated force by 1.5 %, where the surface elevation would decrease the correlation with 9.2 %. The small increase in the force correlation is neglected due to the larger decrease in the correlation seen for the surface elevation. Looking at Table 2 and Table 3, the only clear trend is that the reference point is shifted downstream when compared to wave gauge 3 in the experiments, which was placed at x = 29.38 m. An explanation for this could be that in the experiments, friction is experienced at the boundaries of the wave tank, which slows down the waves. No friction is introduced in the numerical wave tank, thus making the waves faster than in the experiments.

The chosen location will also be used as output for the simulations with wind.

3.1.2 Validation of the numerical model through exceedance probability plots

Exceedance probability curves for both crest height and depth-integrated force will be made for both the simulations and experiments and be compared. To find the crest height, the maximum value of the surface elevation between two subsequent zero-down points is found. Here values of less than 0.005 m are disregarded as waves of this magnitude are not of interest for this thesis. From each test, the crests and force peaks are collected into a long vector, which is sorted in ascending order and plotted against the corresponding exceedance probability. The exceedance probability is calculated through the following equation, \citet{JCKInPress}:

$$P_{Ex} = \frac{1-(i-1)}{\mathrm{N}}, \text{ for } i = 1,2,..,N \tag{10}$$

Where N is the number of observations. The normalization of the crest height is done by dividing the crest height with the significant wave height. The significant wave height is found as the mean value of the 30 % highest wave heights. The normalization of the depth-integrated force is done by dividing with the corresponding significant wave height, the water density, the gravitational acceleration constant, and the radius of the structure squared. When looking at the following exceedance probability plots, the focus in the present thesis will be on how the numerical data and the experimental data compare. Thus, if the numerical model can reproduce the experimental data to a trustworthy degree, the model is validated. The change in the data when the wind is introduced will only, to a small degree, be commented upon. Here the reader is referred to \citet{JCKInPress}, where the work is focused on the change in the data due to the wind being introduced.

3.1.2.1 Exceedance probability plots of normalized crest heights

The exceedance probability for normalized crest heights, for sea state A can be seen in Figure 10 and for sea state B in Figure 11.

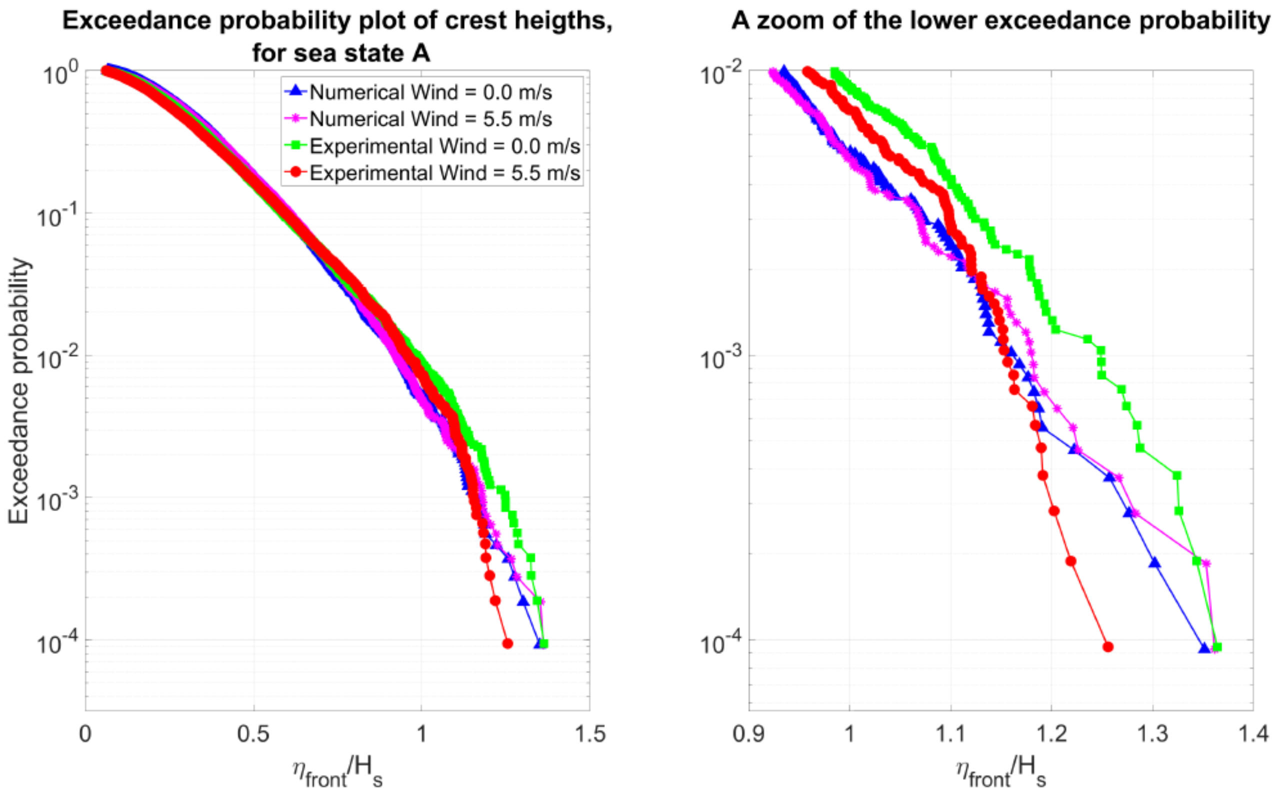

Figure 10: Exceedance probability for normalized crest height, sea state A

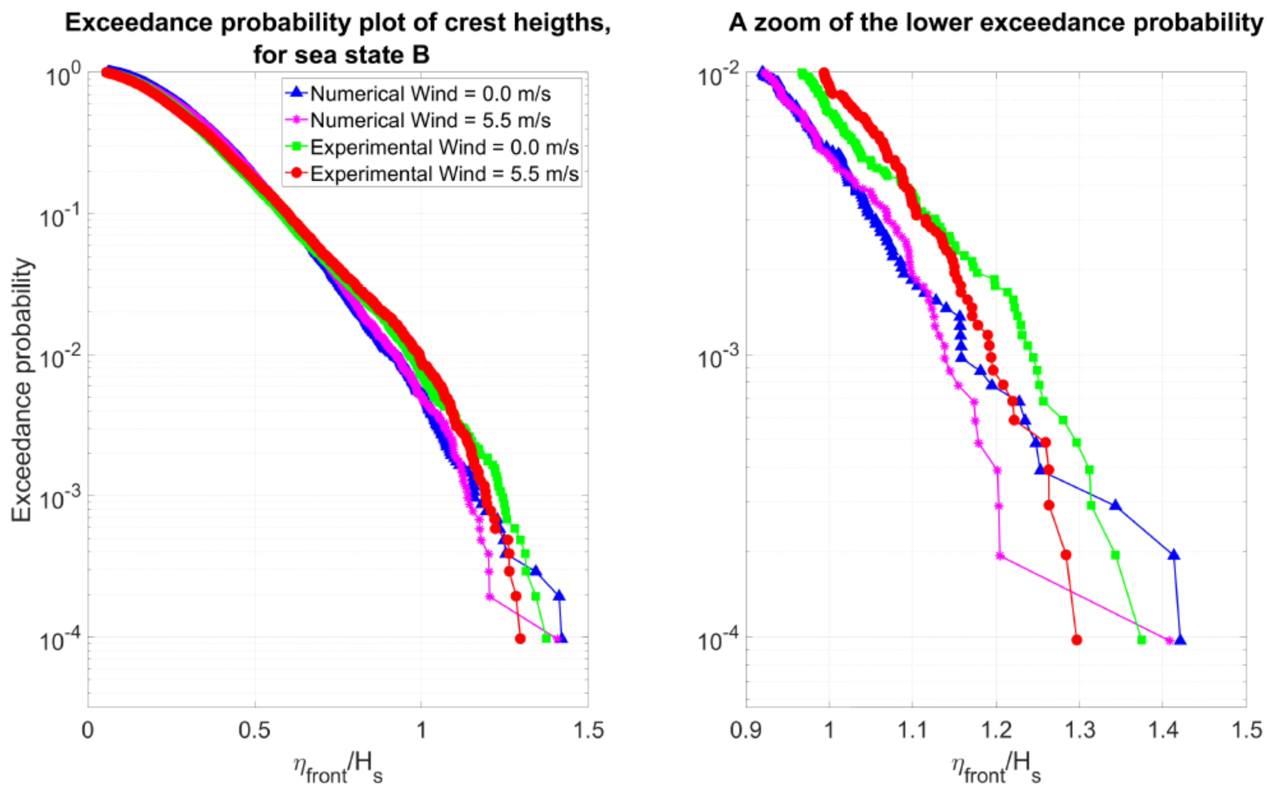

Figure 11: Exceedance probability for normalized crest height, sea state B.

Looking at the two figures, the general shape of the exceedance probability plot is concave, which is captured well with the numerical data. When looking at the magnitude, the numerical data seems to underestimate the crest height values at exceedance probabilities of 10^{-2} to 10^{-3} for both sea states. For sea state A the mean crest height with and without the wind of the experimental data is a factor 1.03 and 1.06, larger than that of the numerical. For sea state B, the factors are; 1.06 (with the wind) and 1.05 (without wind).

Focusing on Figure 10, some alignment and discrepancies between the experimental data and the numerical data are found. Looking at the lower exceedance probabilities (from 10^{-2} and lower), the experimental data shows larger values for the case without wind, with a large difference between the two wind speeds. The largest difference is found at an exceedance probability of $4\cdot 10^{-4}$, where the case without wind is a factor 1.11 larger than the case with the wind. In the numerical data, the two wind speeds follow one another closer, with the case with the wind being a little larger from exceedance probability of $2\cdot 10^{-3}$and lower, showing the opposite of the experimental data at the tail. Within this range, the mean value of the case with wind is a factor 1.01 larger than the mean value for the case without wind. Thus the effect of wind is underestimated within the simulation when compared to the experiments.

Looking at Figure 11, and comparing exceedance probabilities of $3\cdot 10^{-4}$and lower, the mean of the experimental data with wind is a factor 1.01 larger than the experimental. This large coherency is mainly due to the last value of the numerical case. For the case without wind, the numerical data is a factor 1.04 larger than the experimental data. In the experimental data, the normalized crest heights for the case with wind are higher than without wind in the exceedance probability range of $2\cdot 10^{-2}$ to $3\cdot 10^{-4}$. For the lower exceedance probabilities, the case without wind is higher. In the numerical data, the case with the wind has larger magnitudes down to an exceedance probability of $1.5\cdot 10^{-3}$. At lower exceedance probabilities the case without wind shows higher values of normalized crest height. Thus the numerical model seems to capture the effect of wind well within the simulation. As can be seen from the two exceedance probability plots, the tails are associated with large variations. To minimize these variations, another exceedance probability plot for the normalized crest is made, with exceedance probabilities in the range of 1 to 10^{-3}. This is obtained by bundling the data in bundles of 10. A mean and standard deviation is found for each bundle and used to generate the exceedance probability curve. These exceedance probability plots can be found in Figure 12 and Figure 13 for sea state A and B respectively.

Looking at Figure 12 and focusing on the tail of the exceedance plot, the discrepancies commented upon for the exceedance probability curves in Figure 10 are still valid. Nevertheless, the standard deviation indicates that the numerical simulation, to a satisfying degree, captures the magnitude of the experimental data. Within one standard deviation from the mean values, there is an overlay between the experimental and numerical data, both for the case with and without wind. For exceedance probability of 10^{-2} and lower, the mean crest height from the experiment without wind is a factor 1.06 larger than the numerical. When the wind is introduced, the factor is reduced to 1.02. This indicates that the numerical case with wind is better at recreating the magnitude from the experiments. However, the numerical data still finds that the crest height at the tail is increased when the wind is introduced, where the opposite is found in the experimental data.

Looking at Figure 13 the mean of the experimental data is a factor 1.05 larger than the numerical without wind, and a factor 1.06 with wind, in the exceedance probability range of $3\cdot 10^{-2}$ and lower. At the end of the curves (the last bundled mean value), the experimental case without wind is only a factor 1.01 larger, while with the wind, the factor is decreased to 1.03. Thus the effect of averaging did not change the overall tendencies seen in Figure 11. At the tail, the case with wind and without wind changes in having the largest magnitude. This is the case for both the experimental and numerical data, ending with the wind being the lowest. This indicates that for sea state B, the simulation captures the effect of the introduction of wind. By including the standard deviation, it is seen that the mean values of the experimental and numerical data are

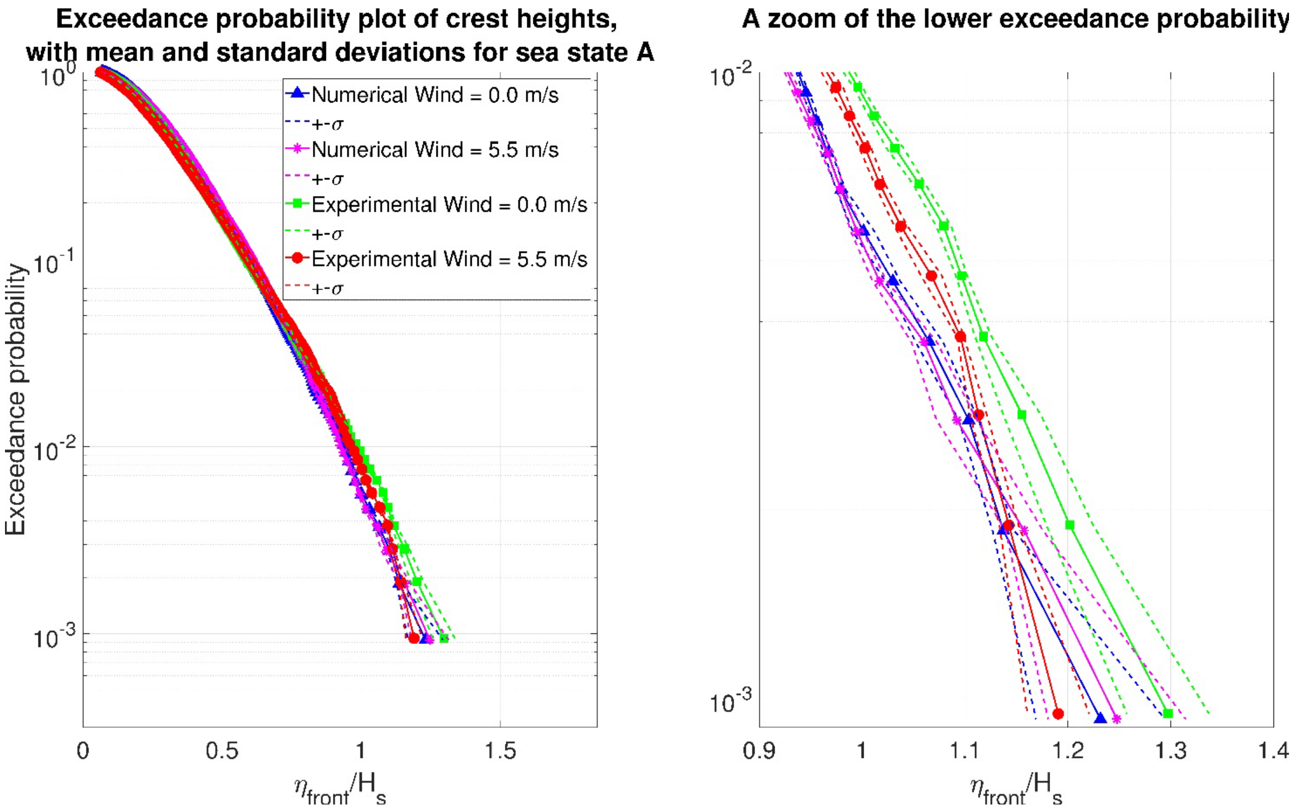

Figure 12: Exceedance probability for normalized crest height with mean and standard deviations, sea state A.

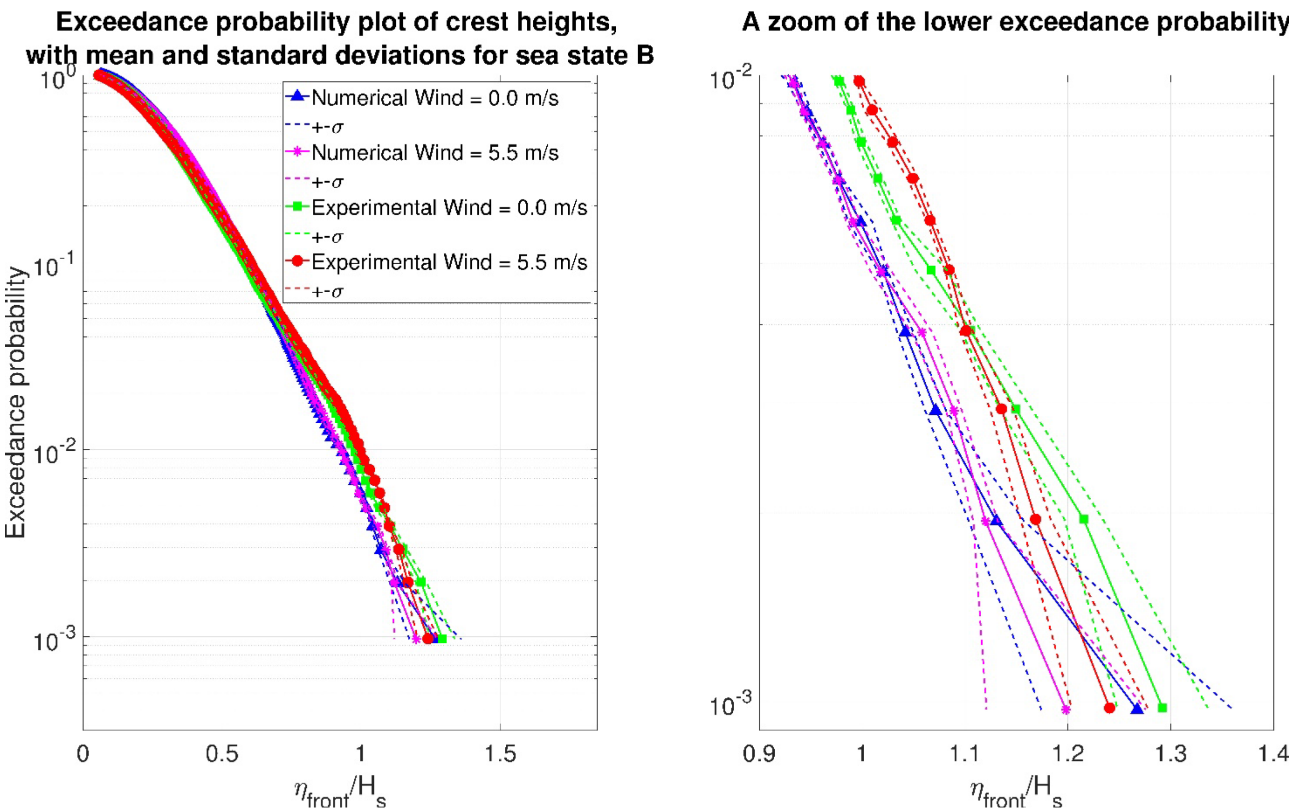

Figure 13: Exceedance probability for normalized crest height with mean and standard deviations, sea state B.

within one standard deviation from one another for the case without wind. For the case with wind, the experimental mean is within one standard deviation of the numerical mean. In contrast, the opposite is not the case, as the mean of the numerical data is just outside the range of one experimental standard deviation. The crest height of the extreme events in the simulation is well aligned with experiments. The factor between the numerical and experimental data decreased with and without wind when averaging values.

3.1.2.2 Exceedance probability plots of normalized depth-integrated force peaks

The exceedance probability of depth-integrated force peaks, for sea state A can be seen in Figure 14 and for sea state B in Figure 15.

First, by looking at the two figures, the overall shape is concave for both the numerical and experimental data. Looking at the magnitude of the depth-integrated force, there is a good coherency between the experimental and numerical data for both sea states. At the tails, a larger variation is seen.

Focusing first on Figure 14 the experimental and numerical data follows one another well. This is seen as the mean of the numerical data for the whole curve only is a factor 1.01 (with the wind) and 1.04 (without wind) larger than the experimental data. For the normalized crest height, the mean of the numerical data for the whole curve was a factor 1.06 (with the wind) and 1.04 (without wind) larger than the experimental data. This indicates that the magnitude of the depth-integrated force is better estimated than the crest height. In the experimental and numerical data, the largest values of depth-integrated force shift between the case with and without wind when the exceedance probability decreases. For the experimental data, the case without wind ends up with the largest value at the tail. When comparing the mean values of the depth-integrated force in the exceedance probability range of $3\cdot10^{-4}$ and lower the numerical value is a factor 1.14 (with the wind) and 1.02 (without wind) larger than the experimental mean. Even though a small factor is observed for the depth-integrated force, larger discrepancies are found at the tail, especially for the case with the wind. The smaller factor without wind at the tail is mainly due to the large value of the last observation.

Looking at Figure 15 the experimental case with wind at an exceedance probability of $2\cdot10^{-2}$ to $3\cdot10^{-4}$ becomes significantly larger than the remaining three curves. The mean of the depth-integrated force is 1.09, 1.10, and 1.08 larger than the three other cases (experimental without wind, numerical with wind, and numerical without wind, respectively). However, looking at the factors, this indicates that the three other cases lie close. Thus it seems as if the force is well aligned for the case without wind, where the numerical and experimental data follow one another.

When looking at the case with wind, the trend with the wind increasing the depth-integrated force is seen in the numerical and experimental data. From an exceedance probability of $5\cdot10^{-2}$ and lower, the numerical case with the wind has larger values than without wind. This indicates that even though the magnitude of the numerical case with wind is different from the experimental data, the trend of increasing force, when the wind is introduced is captured well within the numerical model. At the tail of the exceedance probability, the numerical data with the wind also seems to estimate better the magnitude of the depth-integrated force when compared to the experimental data. From an exceedance probability of $3\cdot10^{-4}$ and lower, the numerical case with wind shows significantly larger values than the case without wind. Comparing the mean values of the numerical and experimental data in this range, the factor between the numerical and experimental data is reduced to 1.00. However, for the case without wind in the same range, the numerical data is 1.09 larger than the experimental. These increased values are close to the experimental case with the wind.

Thus, in general, the case without wind is a better match for the higher exceedance probabilities, where the effect of wind is underestimated in the simulation. At the tail, the simulation without wind overestimates the

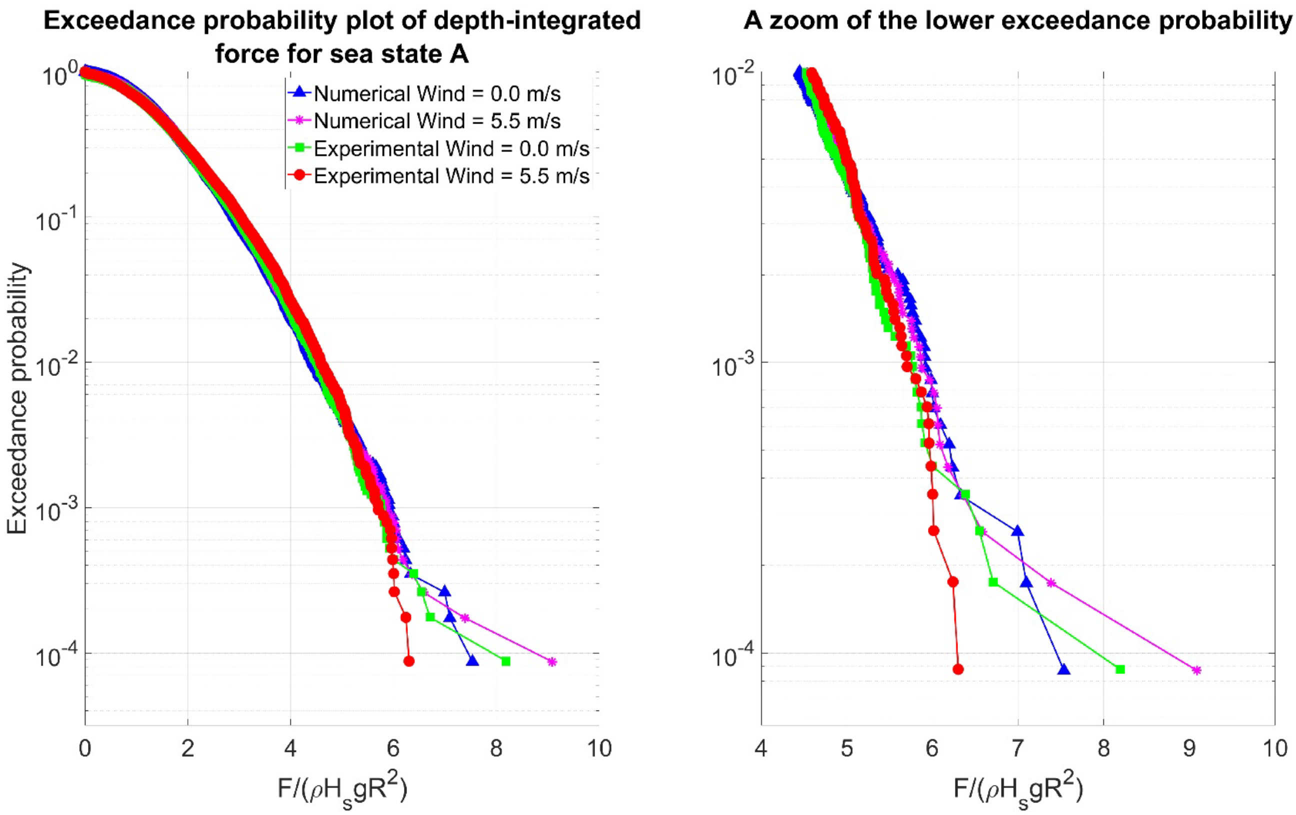

Figure 14: Exceedance probability of depth-integrated force, normalized, sea state A.

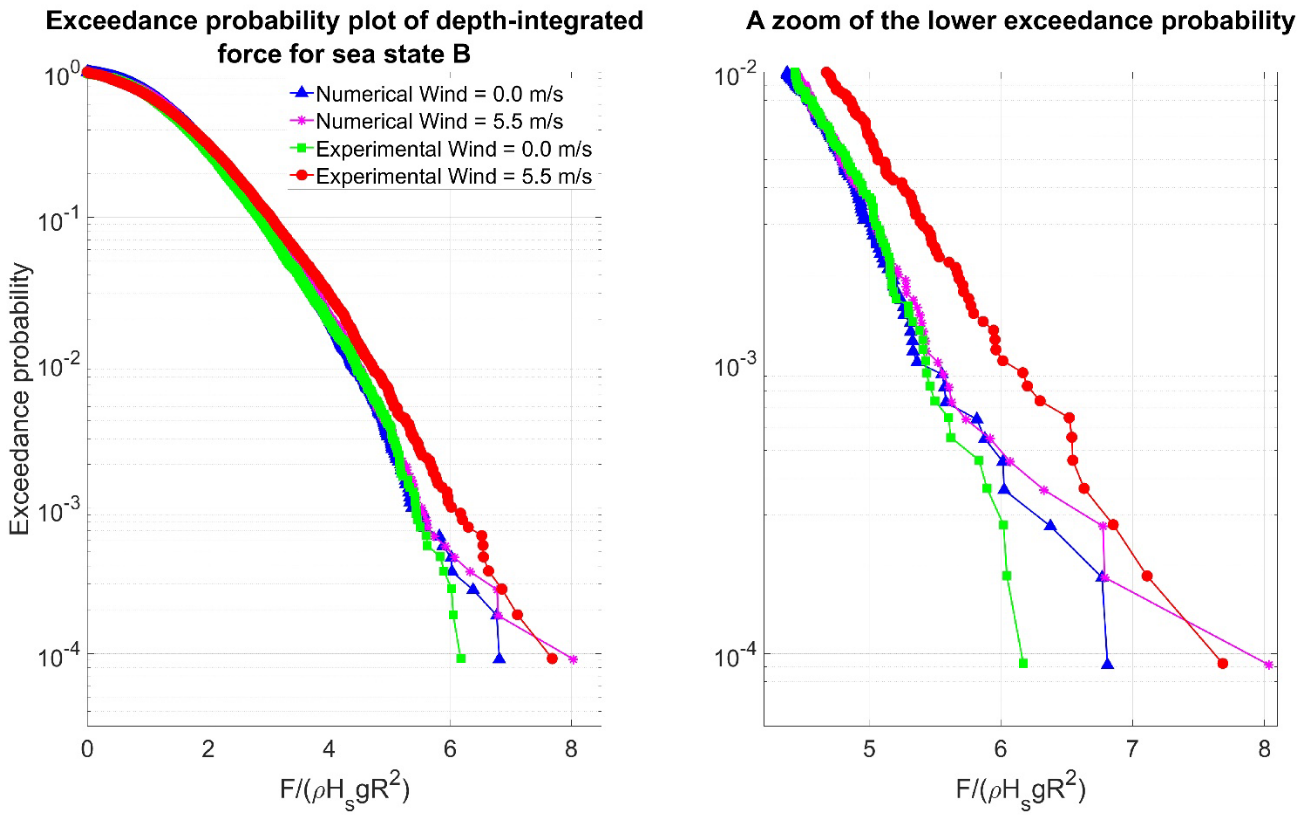

Figure 15: Exceedance probability plot of depth-integrated force, normalized, sea state B.

extreme events, where however the case with wind is more aligned. Looking at the effect of applying the wind, this is captured well within the simulation.

The bundled exceedance probability for depth-integrated force can be found in Figure 16 and Figure 17. Here the focus again is to generate a smoother exceedance probability plot in order to investigate if the discrepancies seen in the two figures above is due to large variations.

First, by focusing on sea state A, Figure 16, the effect of bundling does not change the overall shape and tendencies of the data. However, at the tail, the effect is relatively straightforward, as the significant variation seen in Figure 14 at the tail is removed. The experimental case with the wind has a larger magnitude at exceedance probability of 10^{-2} to $5 \cdot 10^{-3}$ when compared to the experimental case without wind. The same observation is made for the numerical case in the exceedance probability range of 10^{-2} to $7 \cdot 10^{-3}$. At lower exceedance probabilities, the case with the wind has a lower magnitude than the case without wind, except the numerical case, where the last value is larger.

By including the standard deviation and focusing on the tail (exceedance probability of 10^{-2} and lower), the mean values for the case without wind, the numerical and experimental data is within one standard deviation from each other, indicating a good numerical replication of the experiment. However, when looking at the case with wind included, a larger difference is found, where the mean of the depth-integrated force of the numerical data is a factor 1.01 larger than the experimental. At the end of the tail, the numerical data has a larger variation, where the range of plus-minus one standard deviation is 5.6 to 7.6. For the experimental data, the range is 5.8 to 6.1. This indicates that the simulation for the case with wind introduces a larger variation than what is seen for the experimental case.

At the lower exceedance probabilities, the magnitude of the case with wind is higher than the case without wind, which is the case of both numerical and experimental data. Thus the numerical simulation seems to capture the trend within the experimental data.

The corresponding exceedance probability plot for sea state B, is found in Figure 17. Again the main tendencies within the data are still present, the overall shape is concave, and the experimental case with the wind still has a larger magnitude than the other cases.

When comparing the tail for the two cases without wind (exceedance probabilities of 10^{-2} and lower), the numerical and experimental data are well aligned through all exceedance probabilities. Taking the mean of the depth-integrated force for all exceedance probabilities, the factor between the numerical and experimental is found to 1.00. Only at the last value, some difference between the two cases is observed. Here the numerical is a factor 1.05 larger than the experimental values. Even so, the mean values of the two cases lie within one standard deviation from one another. This indicates that the simulation has recreated the experimental data well.

When focusing on the case with wind, there is a larger difference in the magnitude between the numerical and experimental data at exceedance probabilities of $5 \cdot 10^{-3}$ and lower, where the mean of the experimental data is a factor 1.06 larger than the mean of the numerical data. However, at the end of the tail, the difference is decreased, and the mean values of the experimental and numerical data lie within one standard deviation. The factor between the mean of the numerical and experimental data is decreased to 1.05. Disregarding the magnitude issue, the overall trend is that wind increases the force, which is seen in numerical and experimental data.

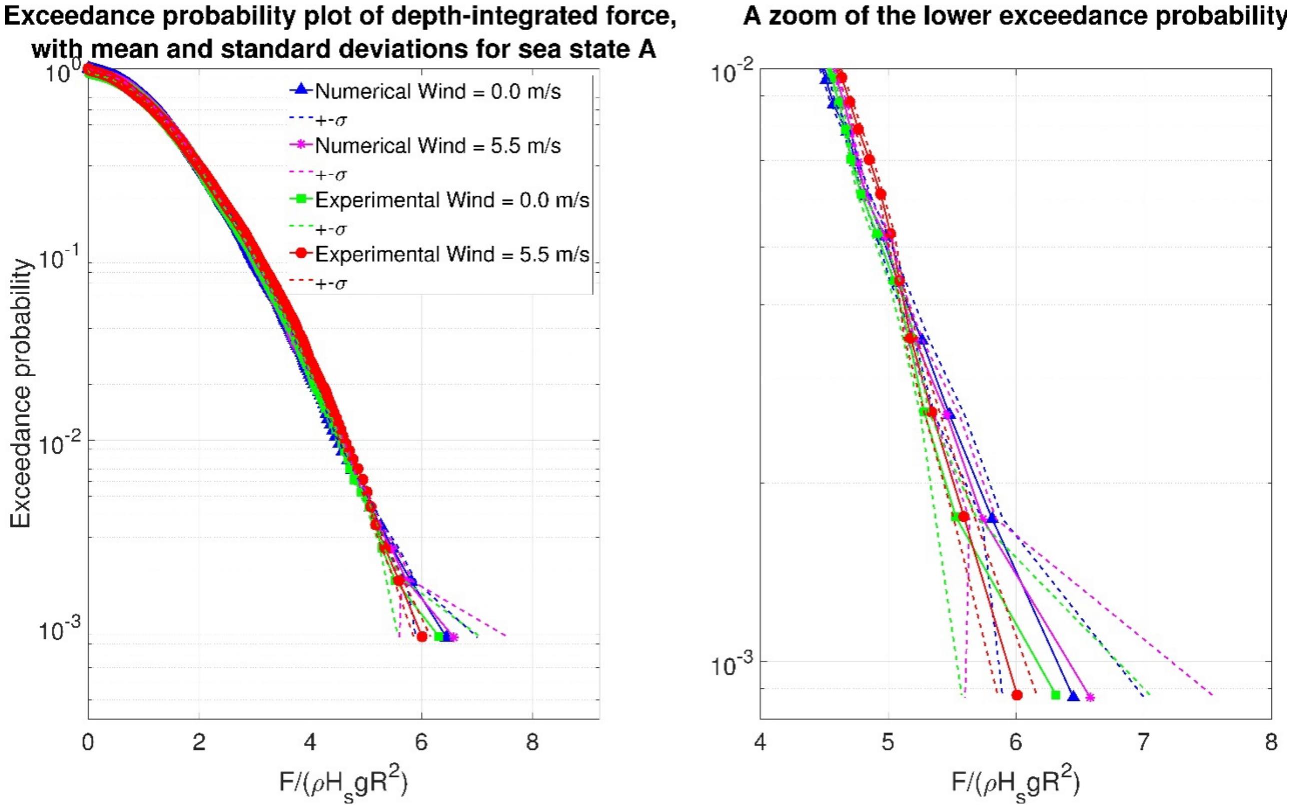

Figure 16: Exceedance probability of mean depth-integrated force peaks, normalized, sea state A.

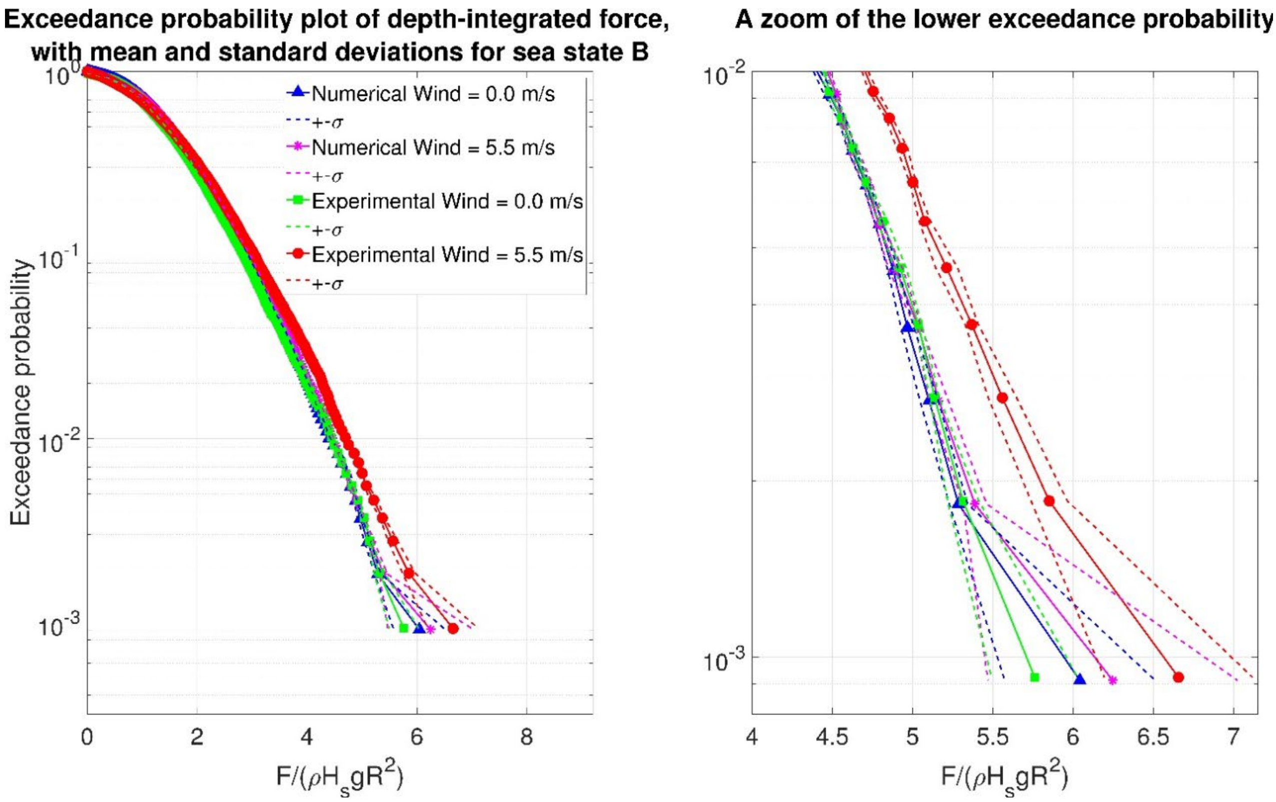

Figure 17: Exceedance probability of mean depth-integrated force peaks, normalized, sea state B.

3.2 Summary of results

The numerical domain was based on the experiments. At the same time, the discretization in the x-direction ensured at least 30 points per peak wavelength, with a total of 801 points in the x-direction. A total of 20 points was included in the z-direction, and the time increment was set to dt = 0.015625 s, which was downsampled from the experiments. The interval and the time increment resulted in Courant numbers of approximately 0.5 for both sea states, which is below the theoretical maximum value of 1.

Based on correlation values of the crest and force, a spatial shift downstream was found for the reference point. The new reference point was based on the correlation values of both crest height and force. The correlation values for the force also indicated a time shift, where the correlation increased by 1.5 %. However, such a time shift would decrease the correlation of the crest height by 9.2 %. Thus, in conclusion, no time shift was included.

By comparing the experimental data with the numerical data in the four exceedance probability plots, it is found that the overall trends in the experimental data are to a satisfying degree present within the numerical results for both sea states. For sea state A the numerical data was well aligned with the experimental data when no wind was present. Introducing the wind, the simulation indicated an increase of the extreme events at the tail for both crest and depth-integrated force. The opposite was observed within the experimental data.

Comparing this to sea state B, a difference in magnitude was observed for the crest height and the depth-integrated force. For the crest, a height difference was observed both with and without wind. For the depth-integrated force, a difference in magnitude was mainly observed when the wind was introduced. Looking into the effect of introducing wind, the experimental crest and depth-integrated force were increased at the end of the tail. This was also seen in the numerical data. At the intermediate exceedance probabilities the experimental data showed an increase in crest height, but for the extreme events the case without wind showed higher crests. The same trend was found in the numerical data. For the depth-integrated force in the experimental data, the overall curve was increased when the wind was introduced, with a significant difference in magnitude. In the numerical data, the same was present, however, with a less pronounced difference in magnitude.

As the effect of the wind is better aligned between numerical and experimental data for sea state B, this sea state will be scaled to large scale and used for further simulations.

4. Large Scale Model

This part of the thesis investigates ocean wave behavior on a large scale by simulating 1,000 waves with and without wind for three different sea states. Through this work, trends will be identified, and wave characteristics and wave-induced loads will be analyzed.

The size of the numerical wave tank will be chosen large enough to mimic real-life extreme wave events. The domain to be simulated will be based on thorough investigations, consisting of a detailed convergence study and evaluation of proceedings in earlier studies. This will be explained later. Parameters for the large scale simulations will be based on a study of previous extreme wave events and scaled parameters from the experiments treated in the previous model scale section. This will be explained in the next section.

4.1 Sea states

A total of three sea states will create the basis for the large scale analysis.

To enable an analysis of extreme wave events, input parameters for the simulation must have characteristics stemming from extreme sea states. Such a sea state was present in the Troll field in the North Sea on 30th of

December 2015. Here, the mobile drilling unit COSLInnovator was struck by a large wave that killed one and injured four others. 17 windows were smashed, and water intrusion caused extensive damage, \citet{Techreport}. If more personnel had stayed in their cabins, the death toll of the accident had most likely been larger. The investigation team presented a report,\citet{Techreport}, on the 6th of July 2016, which included a description of the weather on the day of the accident. The following main weather parameters were assumed to be prevailing on the time of the accident:

- Significant wave height: $H_s = 8.5 – 9.5$ m
- Wave spectrum peak period: $T_p = 12 – 14$ s
- 10-minute mean wind speed: W = 24 – 26 m/s

As the platform was operating within the Troll field at the time of the accident, the depth is varying between 300-330 metres, \citet{FieldTRO16:online}. For this study, the depth is chosen to 300 metres. The higher values of the interval for weather parameters are selected, i.e., a peak period of 14 s and a significant wave height of 9.5 m are chosen. Thus for the first sea state, efforts will be made to recreate the conditions of the Troll field of the 30th of December 2015.

The second sea state is based on the a scaled version of sea state B from the model scale investigations. This is seen in following Table:

Table 4: Comparison of parameters between sea state B in model scale investigations and second sea state of the large-scale simulations.

	Hs [m]	Tp [s]	d [m]
Sea state B model scale	0.09	1.05	0.9
Second sea state of large scale simulations	9.0	10.53	90

The scaling of the sea state is based on Froude scaling to obtain dynamic similitude. Here the linear dimensions, such as height and depth, uses a scale factor of λ, while the period uses a scale factor of √λ. As can be appreciated from the table, a factor of 100 is applied to the significant wave height and depth, while the period is scaled with a factor of 10, thus complying with the rules of Froude scaling. Further, the slender cylinder, in which the load is calculated and investigated, is scaled with λ as well, thus obtaining a diameter of 10 m.

The third and last sea state will be based on parameters stemming from the 10 m significant wave height storm at the Danish Tyra gas field, in which surprising data showed unusual large plunging breaker waves. Photo and video recording revealed two plunging, breaking extreme waves with heights approximated up to 17.5 m, \citet{tychsen2016summary}. The concerning part of this was that both waves were recorded in the same storm at the same site, and both of them exceeded the 10,000 year return period, both for crest height and crest kinematics. While the data recordings present specified parameters, these are changed slightly in the simulations. This is done to create a stronger basis for comparison between the sea states. The slight change is outlined in the following Table:

Table 5: Comparison of measured parameters and parameters used for the third sea state of the large scale simulations.

	Hs [m]	Tp [s]	d [m]
Data recordings Tyra Field	10	14.50	45
Large-scale simulations	10	14.29	90

While the same significant wave height is maintained, the period is changed to match sea state 1 and the depth changed to match sea state 2. The following Table summarizes the parameter of the three sea states used in the large scale simulations:

Table 6: Overview of parameters for the three sea states.

Large-scale parameters	Hs [m]	Tp [s]	d [m]
Sea state 1	9.5	14.50	300
Sea state 2	9.0	10.53	90
Sea state 3	10.0	14.29	90

To indicate the severity of the sea states, a diagram showing the validity of wave theories is inserted with the three sea states indicated, as it was done for the two sea states on model scale. This is seen on Figure 18. The further to the left and top of the diagram, the more nonlinear the waves. The position of the sea states on the diagram is two-fold, as the peak periods and depths are applied with both the significant wave height and the theoretical maximum wave height for 1,000 waves, H_{1000}. The red crosses are based on significant wave height, while the magenta dots indicate the maximum wave height for 1,000 waves. The latter is calculated by the following formula:

$$H_{1000} = H_s \cdot \sqrt{0.5ln(1000)} = H_s \cdot 1.86 \tag{11}$$

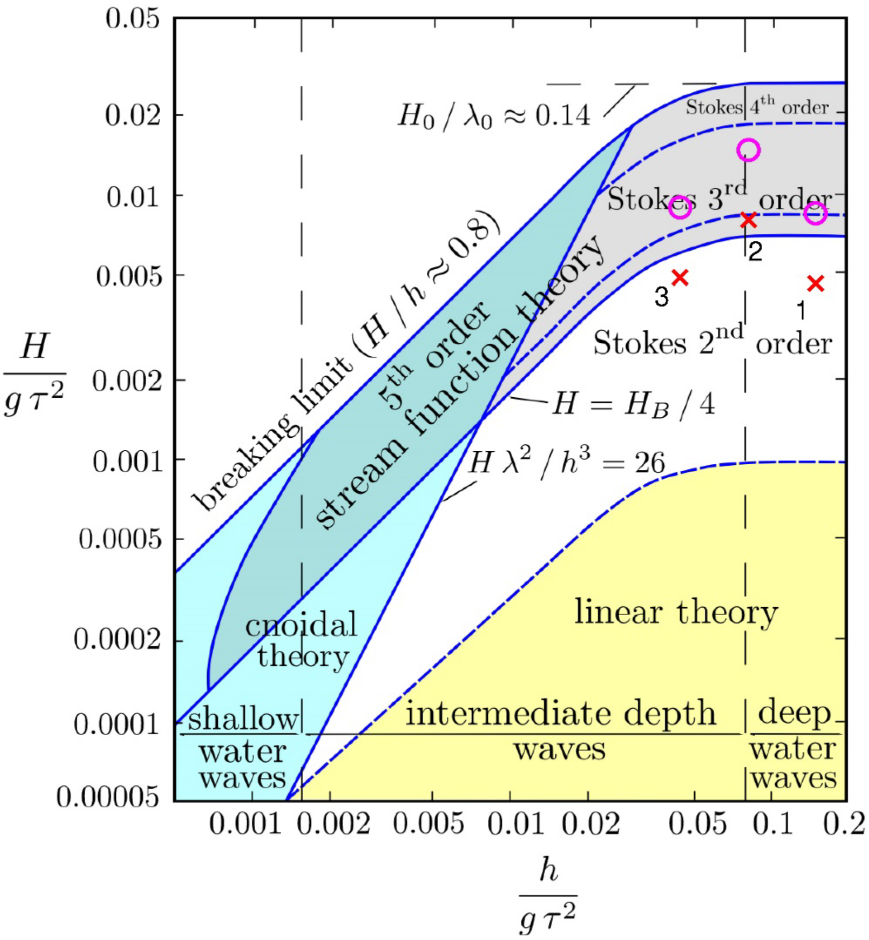

Figure 18: Diagram showing validity of the wave theories, \citet{le2013introduction}. Red crosses indicate water depth, h, significant wave height, H_s, and peak period, T_p. Magenta dots indicate h, T_p and theoretical maximum wave height for 1,000 waves, H_{1000}. 1,2 and 3 indicate the three sea states.

The first and most straightforward thing to conclude is that none of the sea states are accurately described by linear theory. The three sea states are ranging from high levels of intermediate depth to deep water. Further, the diagram shows, that the sea states become more nonlinear, as the depth decrease. Hence, Sea state 2 and 3 seems to be more nonlinear than 1, as their depth is defined to 90 m. Furthermore Sea state 2 reach the highest vertical position because of the largest significant wave height, but not as far to the left as Sea state 3 due to a lower peak period.

Simulations for the three sea states will be run with and without an instantaneous wind field above the waves. This allows for an analysis of the direct effect of the wind on the wave group. Furthermore, two different values for the mean wind speed will be used for the case with wind. The first wind speed will be based on the expected 10 minute mean wind speed present at the COSLInnovator on the day of the accident on 30th December 2015. The second wind speed will also be based on this wind speed but instead, be converted to a 3 seconds gust speed. This is done by use of a gust factor, G_{τ,T_0}, which is found by use of Table 1.1 from \citet{harper2010guidelines}.

With the Troll field being more than 20 km from shore and a reference period, T_0, of 600 s, the gust wind speed is found to:

$$W_{gust} = 24\,\frac{\mathrm{m}}{\mathrm{s}} \cdot 1.23 = 29.5\,\frac{\mathrm{m}}{\mathrm{s}} \qquad (12)$$

The three sea states will thus be simulated for wind speeds of 0, 24 and 29.5 m/s.

4.2 Domain size

This section will outline the procedures carried out to decide the domain size and discretization of the numerical wave tank for large scale simulation purposes. Some of the analysis will be inspired by recent similar numerical studies that have dealt with domain size analysis. The domain size investigations are based on the first sea state mentioned in the previous section.

First, the overall domain length will be investigated. This is found in the Sub-section underneath. The length of the wave generation zone and the damping pressure zone will be covered in this section. Subsequently, the grid spacing, i.e., the discretization in space in the x- and z-direction is covered, together with the discretization in time. Finally, an overview of the final domain is outlined.

4.2.1 Domain length

Determining properties for a numerical domain for numerical investigations like those carried out in this study can be quite complex and may not be as straightforward as first assumed. Many of the properties are dependant on one another, and the challenge can quickly seem somewhat iterative. If the wave generation zone length is changed, it influences the choice of length of the total domain and vice versa. When a parameter changes, it alters how the sea state develops and the corresponding time to develop fully. Hence, a systematic and consistent analysis procedure must be employed, and awareness must be paid to whether or not the methodology and procedure used are, in fact, the most correct.

For the present study, it was chosen to lock some of the parameters to shorten the list of changing variables. Therefore, the wave generation zone and damping pressure zone were chosen to be fixed lengths based on the expected longest wave obtained in the simulations. As such, first, the expected longest wavelengths of the simulations must be found. To do this, a JONSWAP spectrum based on the parameters for Sea state 1 mentioned in the previous section. The JONSWAP spectrum is drawn and depicted in Figure 19.

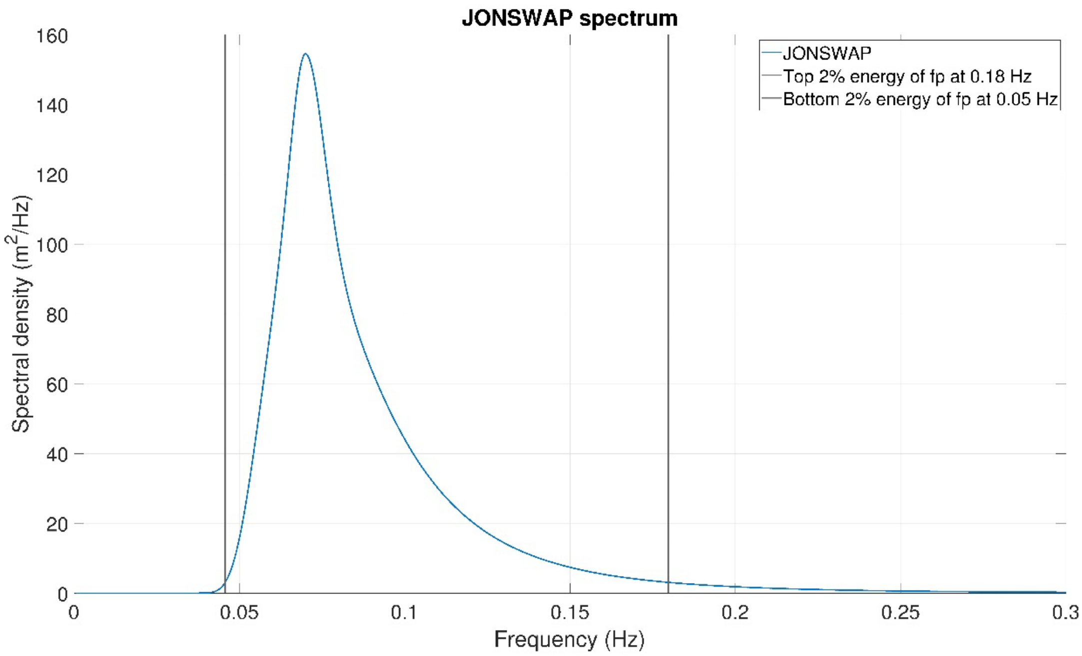

Figure 19: JONSWAP spectrum for large-scale simulations, H_s = 9.5 m and T_p = 14.29 s.

As can be appreciated from Figure 19, the peak frequency is found to 0.07 Hz. Further are the top and bottom 2 % of energy content at the peak frequency indicated by a black vertical line at 0.18 Hz and 0.05 Hz, respectively. These two values are used to calculate the expected shortest and longest wave. This way of approaching the problem is inspired by \citet{PhDSchl}, where a 2 % quantile is being used. The calculation of expected shortest and longest wave is approximately found by using simple regular wave theory:

$$\omega = 2\pi f \tag{13}$$

$$k = \frac{\omega}{c} \tag{14}$$

$$L = \frac{2\,\pi}{\mathrm{k}} \tag{15}$$

The celerity used in Equation (14) is calculated based on deep water wave theory:

$$c = \frac{\mathrm{gT}}{2\,\pi} = 1.56 \cdot T \qquad \text{if} \;\; 0.5 < \mathrm{d/L} \tag{16}$$

Furthermore, the celerity for the peak wave can be read from the log file of OceanWave3D if the CFL condition is enabled in the simulation. As stated in Section 2, the CFL condition couples the spatial discretization and the time discretization using the following equation:

$$dt = \frac{\mathrm{C{\cdot}dx_{min}}}{\mathrm{c}} \tag{17}$$

A threshold value between 0 and 1 is chosen for the Courant number, and together with a defined discretization, OceanWave3D will calculate the time increment. For the domain study, the value for the Courant number is initially set to 0.75. By verifying the simple deep water wave relation and using Equation 16 the wave celerity is found to c = 8.697 m/s.

By applying the equations above, length and celerity can be found for the 2 % of the energy content at peak frequency. These values are shown in the Table:

Table 7: Length and celerity of waves with respect to different energy contents of the peak frequency for sea state 1.

	2 % of energy at f_p	**Peak frequency, f_p**	**98% of energy at f_p**
Wavelength [m]	754.47	318.96	48.40
Wave celerity [m/s]	34.34	22.33	8.70

Following \citet{engsig2009efficient}, the wave generation zone is set as twice the longest wavelength. In the mentioned study, the investigation is centred around 3D application and propagation of steep regular nonlinear waves in deep water. However, it has been assessed that the rule of thumb is applicable for the present study. Hence, by rounding the wavelength for the 2 % of the energy at the peak frequency to the nearest 10 m, the wave generation zone will have a length of 1,500 m, divided into two generation zones. As the length of the damping pressure zone follows the wave generation zone length, this will have a length of 1,500 m as well.

In addition to using Figure 19 to calculate wavelengths and determine relaxation zones, it can be used to decide the cut off frequency, kh_{max}, necessary as input for the simulations. Here the top 2 % energy with the corresponding frequency of 0.18 Hz will be used. By using Equation 13 and Equation 14 to calculate ω and k the cutoff frequency kh_{max} can be found:

$$kh_{max} = k \cdot h = 38.95 \tag{18}$$

As such, the cut-off frequency used for large scale simulations is set to 38.95. To determine the total length of the numerical domain, multiple investigations have been carried out. These are based on analysis of simulation number 1, with parameters shown in the Table:

Table 8: Simulation parameters for the simulation used to analyze domain length. The simulation is run on computer number 2, per Table 1}.

Simulation no.	**Lx [m]**	**Lz [m]**	**Nx [-]**	**Nz [-]**	**Nt [-]**	**dt [s]**	**CFL [-]**	**CPU time [hr]**
1	20,000	300	4,120	15	54,650	0.16664	0.75	11.40

The parameters listed above results in a grid spacing in the horizontal direction (x-direction) of 4.85 m. The grid spacing in the vertical direction varies, as the clustering is enabled for nodes in this direction, resulting in less spacing closer to the surface.

The first point in which results were taken out was in 2,250 metres. This is equivalent to the length of the wave generations zone plus the longest wavelength based on 2 % energy content of peak frequency. Hereafter, results were acquired approximately every 1,000 metres until the last point in 18,252 m. The first 2,100 seconds of the solution is removed to ensure that the slowest waves have travelled to the endpoint of the numerical tank. By applying these settings and parameters, 580 waves are propagated through the 18.252 km mark. This number of waves is assessed to be sufficient for the study of domain length.

The purpose of the simulation is to analyse results to achieve a more precise indication of where in the numerical wave tank the sea state has developed nonlinearities. First, the results are investigated in the frequency domain by a power spectrum analysis and afterward inspected in the time domain. Figure 20 shows the power spectrum for the simulation mentioned in Table 8. The blue line indicates the raw original power spectrum, whereas the orange line is an averaged power spectrum. The latter is found by averaging bundles of 20 values at a time. This presents a more smooth-looking curve that still captures the trends without the large scatter that complicates the analysis procedure.

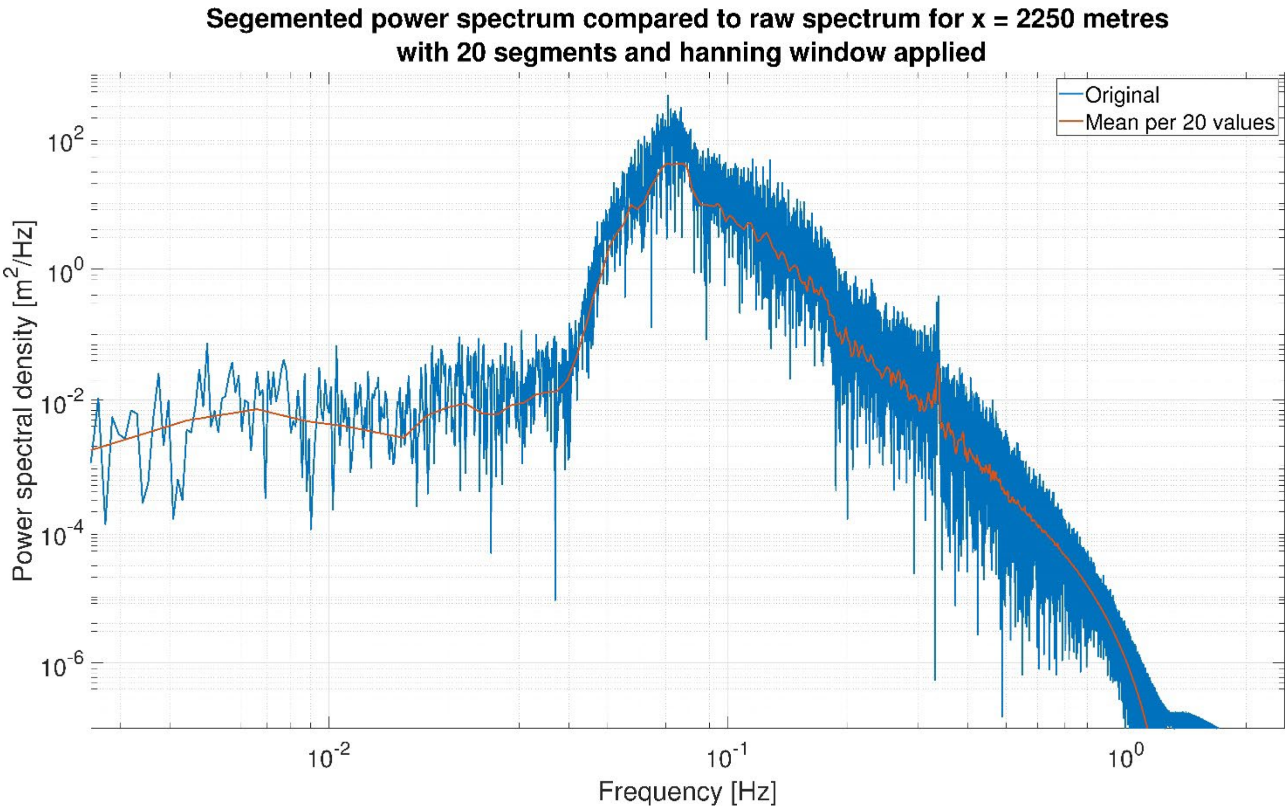

Figure 20: Power spectrum for simulation no. 1.

The power spectrum is created by finding the Fourier transform of the solution for the surface elevation at x = 1500 metres for all time steps. Before making the transform, it is good practice to apply a Hanning window. This is multiplied by the raw input signal in the time domain before finding the Fourier transform. This is done to avoid a smeared signal and spectral leakage, where it will appear as if energy is leaking from one frequency into other frequencies. The Hanning window follows a sinusoidal shape, resulting in a wide peak, but with low side-lobes.

From Figure 20 it is easily observed that the peak frequency of 0.07 Hz holds the most energy. Further, the low side-lobes are visible in the figure. Here, the main lobe is centred around the peak, with a large sudden decrease in density for lower frequencies, whereas the higher frequencies' density decreases a bit more gradually. As nonlinearity increases in wave realizations, the steeper the waves can be, and the more energy is likely to be relocated to higher and lower frequencies. In this case, more energy is relocated to frequencies just above the peak frequency than just below.

To investigate the development of the waves throughout the domain, the following Figure 21 is created. The figure contains four subplots with wave spectra plotted for four different locations, all compared to the end location at 18,252 metres. There is approximately 4 kilometres between each location.

The first subplot shows lower energy for the early location than the end location for the high-frequency range. Meanwhile, discrepancies are seen for the lowest frequency range as well. Further, a small spike in energy is seen at a frequency around 0.3-0.35 Hz. This spike occurs based on the defined value for the cut-off frequency. This spike is also observed for the next x-value shown, at x = 8,250 metres. Here the trend above the peak frequency is the opposite. Here the spectrum for the early location shows larger energy levels than that of the end location. This location is the only one showing larger values than the end location. A slight difference in energy level convergence is seen in the low-frequency range as well. This observation is common for the three first locations. For the third location, at x = 12,251 metres, the power spectrum is

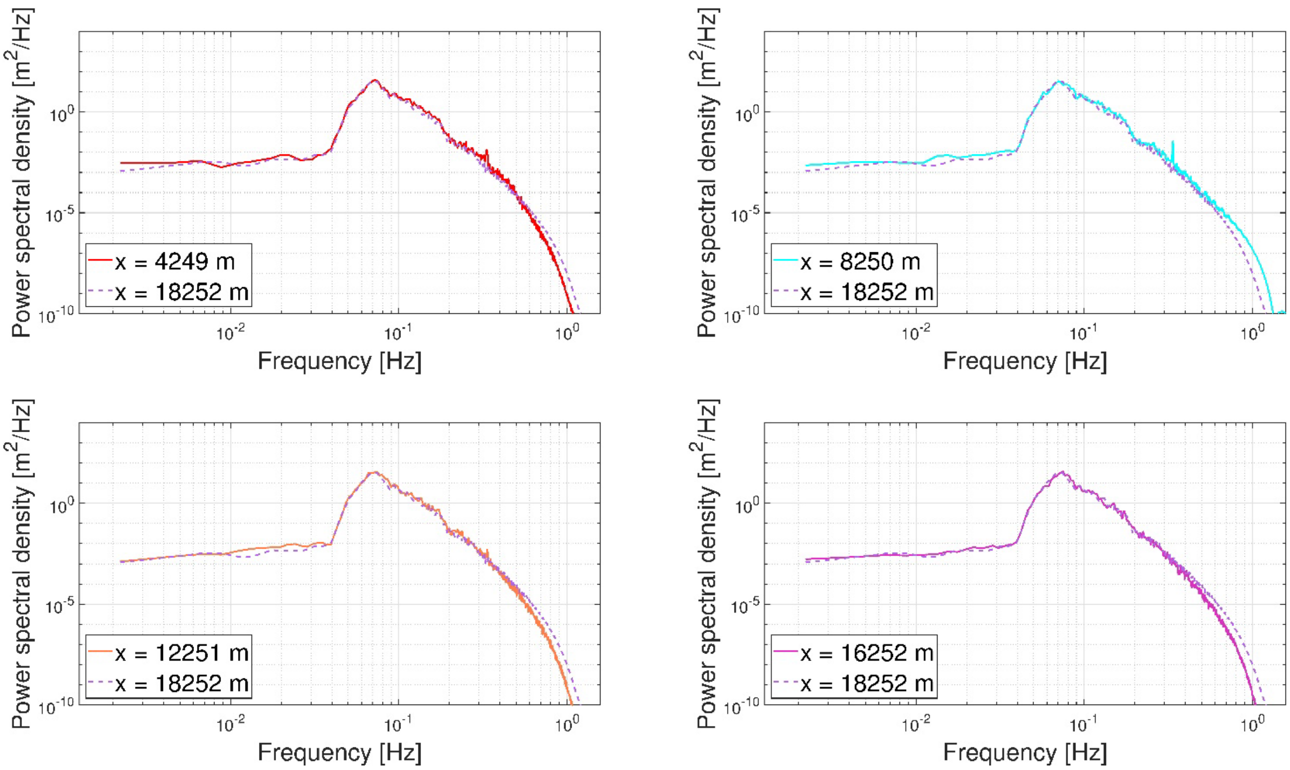

Figure 21: Power spectrum for 4 different locations in the numerical wave tank compared to the end location.

very well aligned with that of the end location from $4 \cdot 10^{-2}$ up until around $5 \cdot 10^{-1}$. Further, the spike between 0.3-0.35 Hz is removed at this location. The low and very high-frequency range is still subject to discrepancies, however smaller than at prior locations.

At the last of the four locations, the energy level for the specific location and the end location are well aligned until frequency levels of around $4 \cdot 10^{-1}$ Hz, where discrepancy is introduced, just as with the other locations. Based on these findings, despite the low and very high-frequency range is not perfectly aligned for the coordinate location, 12,251 metres is deemed the best location to move forward with. This position in the tank shows coherent energy levels at peak frequency and in the ranges just below and above. The fourth location does present a better fit at the lower frequency range. However, this comes with the price of another 2 km added in the domain size, and thus an increased computation time.

However, as the overall trend of the four subplots are not continuous, and since some discrepancy is showing on the logarithmic scale, further investigation is carried out in the time domain before anything is concluded. For the time domain analysis exceedance probability curves for crest height and depth-integrated force peaks are constructed for all available x-values from the simulation. The exceedance probability curve is created for normalized, averaged values for crest heights and depth-integrated force peaks by averaging values per 10 waves. Therefore, by initially investigating a bit more than 500 waves, corresponding to $2 \cdot 10^{-3}$, the exceedance curve now only reaches $2 \cdot 10^{-2}$.

The following Figure 22 shows the exceedance probability for normalized crest height normalized by the significant wave height at each location. The exceedance probability is calculated by Equation 10, as used in previous chapter. By inspecting the high exceedance probabilities, it seems as if there is a tendency towards the lower x-values having the extreme values. From 10^{0} to 10^{-1} minimum and maximum values are dominated by solid lines, thus indicating that the early and centred x-coordinates are over and underestimating the crest values compared to the coordinates further down in the tank.

To investigate the lower exceedance probabilities, a zoom from $9 \cdot 10^{-2}$ and downwards is shown in the right side of Figure 22. From here, it can be seen how the five largest values in the tail are dominated by values between 5,249 and 10,250, except 6,249. Hence, the early half of the coordinates still estimates the highest crests. The three lowest values at the tail end are made up of the first and third most distant x-value. However, the third-lowest value is the third earliest x-coordinate. Such jumps in location are seen multiple places in the tail of the exceedance curve.

A cluster is observed just above the 0.9 value for the non-dimensional crest. One of the coordinates in the cluster is the x-coordinate, x = 12,251 m, which was also investigated in the frequency domain. With non-dimensional values ranging from around 0.85 - 1, this point lies in the middle of that range. To further investigate the x-locations in the tank, the exceedance probability curve for depth-integrated force peaks is plotted for each value. As the force is related to the crest height, although not exclusively, it is expected to see somewhat similar trends. By looking at following Figure 23, it is quickly seen that it is related to Figure 22. Once again, the nearest locations produce the lowest and highest values, in this case, non-dimensionalized force, down to around 10^{-1}. Around this probability, the same coordinate, namely, x = 14,251 m, shows a spike in force as it did for the crest height. Further, the coordinate showing the largest non-dimensional crest height also shows the largest depth-integrated non-dimensional force, with a normalized value of 0.0038 at 10^{-1}. Looking at the zoom of the lower exceedance probabilities, shown on the right on Figure 23, the low valued part of the tail continues to be dominated by the distant x-coordinates, indicated here by the pink, green and blue dashed lines, as it was seen on Figure 22. The 6 highest non-dimensionalized depth-integrated force peaks are represented by x-coordinates for the first half part of the coordinate list. Further, the closely bundled coordinates, containing, x = 12,251 m, are still coincident on the figure, at values centering the extreme values, with normalized values between 0.0086 and 0.0087.

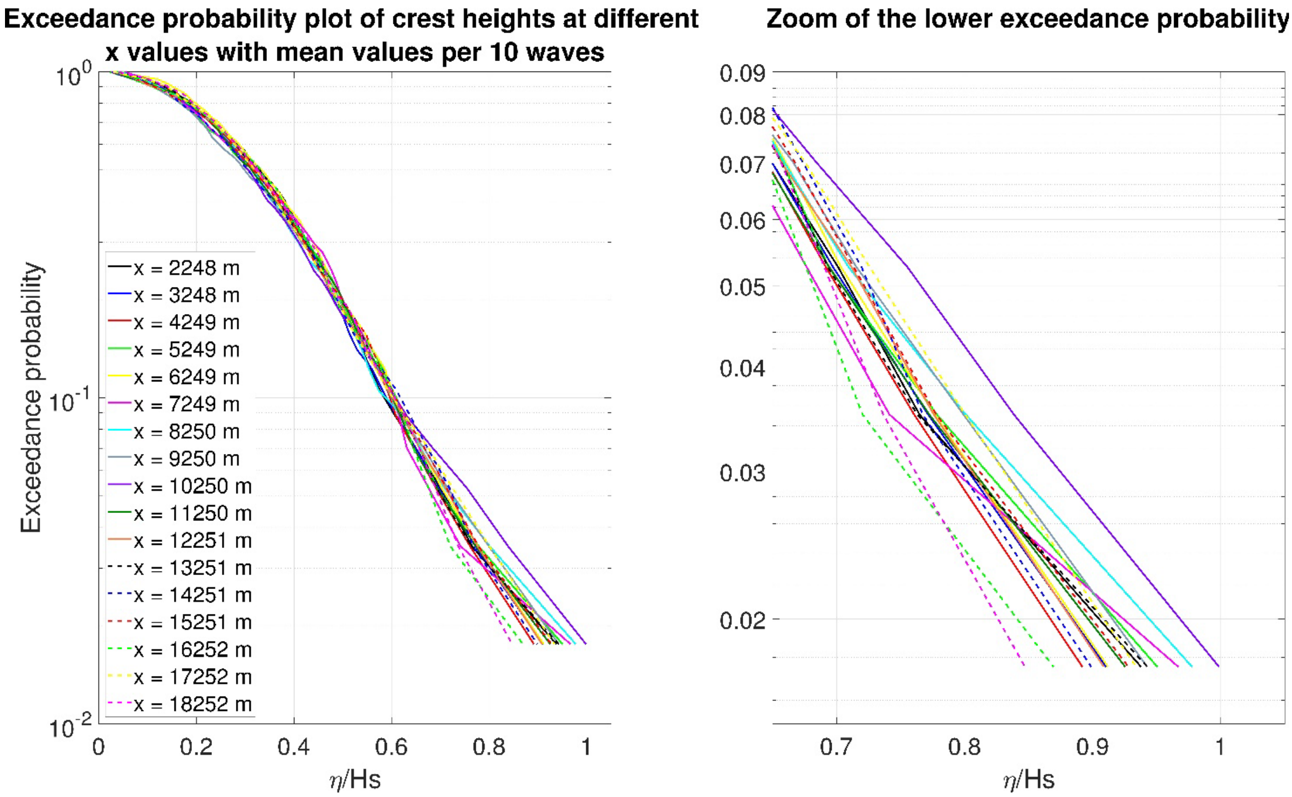

Figure 22: Exceedance probability curves for crest heights at different locations with mean values per 10 waves.

Based on the two types of exceedance probability plots above, there was no argument to oppose the findings in the frequency domain analysis, which pointed towards a domain length of 12,251 m. The time-domain study showed that the early to mid-range x-locations generally presented smaller crests and forces and that the locations toward the end showed decreased results for height and forces. However, some exceptions were present, e.g., the second last location presenting values for crest and height that positions around the average.

Therefore, the point in which results will be taken out from in the large-scale investigations will be placed 12,251 m down in the wave tank. To avoid any clashes between this point and the beginning of the damping pressure zone, the inner boundary of this zone is placed one maximum wavelength away, i.e., approximately 750 m away in 13,065 m. As earlier mentioned, the length of the relaxation zones is fixed, resulting in a total domain length of 14,565 m. Size ratio between relaxation zones and total domain length of the present study are in reasonable compliance with similar studies, such as \citet{PhDSchl}, with both present and mentioned study having relaxation zones making up roughly 20 % of the total domain length.

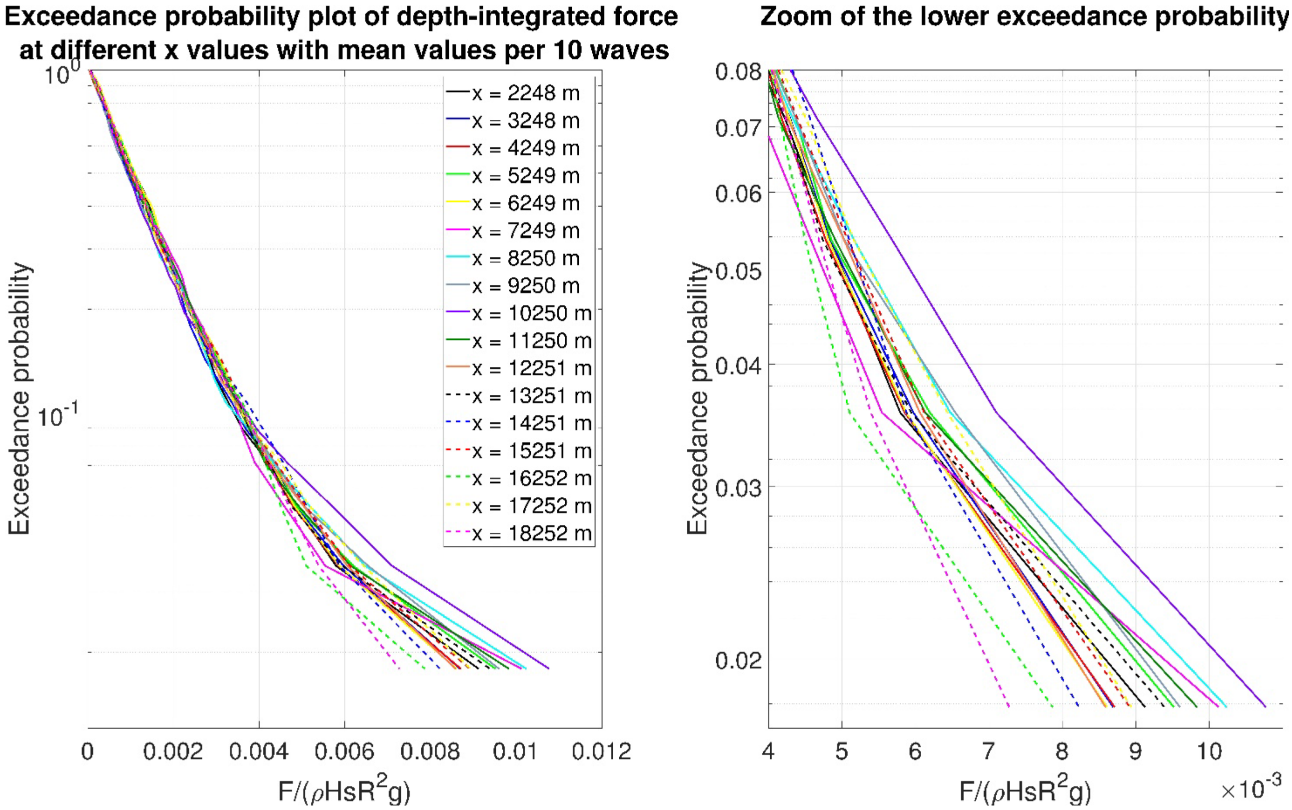

Figure 23: Exceedance probability curves for depth-integrated force at different locations with mean values per 10 waves.

4.2.2 Study of grid convergence: Horizontal direction

This section will describe and go over which steps were carried out to study the discretization in the horizontal direction (x-direction) of the numerical tank.

This section aims to create grounds for a well-founded decision on the optimal number of points per shortest wavelength. Most likely, the most accurate results would be obtained by the most refined discretization, i.e., the shortest wave being resolved into the highest number of grid points and thus the lowest grid spacing. However, the discretization in the horizontal direction is one of the most influential parameters of computational time, and the decision must, therefore, be made by balancing accuracy and computational time.

As the present study is centered around nonlinear irregular waves, it is expected that a higher number of points per wave is necessary than compared to that of regular linear waves, which often is accurately described by 10-12 points per wavelength. Hence, this convergence study will investigate a higher number of points, namely 10, 15, 20, and 25 per shortest wavelength. However, for the sake of comparison, 5 points per wavelength are simulated as well. The following Table 9 presents an overview of the simulation parameters for the simulations used to investigate the horizontal discretization. Simulation number 2 was run to create an input file for the remaining simulations. This is to ensure that the surface elevation in the study is the same for all simulations. Nx = 1501, 3001, 4501, 6001 and 7501 corresponds to the 5, 10, 15, 20 and 25 points per shortest wavelength. The time increment varies for the simulations, as this is included in the CFL condition, where the Courant number is locked at 0.75. Hence, the total number of time steps changes to obtain approximately the same number of waves for each simulation. Consequently, the surface elevation from simulation number 2 is resampled to fit the different simulations and their respective time increments. This is done by defining a fraction, p/q, which is modified according to the individual simulations. This is multiplied by the original surface elevation obtained in simulation number 2, and a polyphase anti-aliasing filter is employed. This way, the surface elevation from simulation number 2, acquired at x = 2252.7 m, is used as input for the remaining simulations in the study of the horizontal discretization.

Table 9: Simulation parameters for simulation used to analyze number of points per shortest wavelength. CPU time is listed for computer number 3, per Table 1.

Simulation no.	**Lx [m]**	**Lz [m]**	**Nx [-]**	dx [m]	**Nz [-]**	**Nt [-]**	**dt [s]**	**CFL [-]**	**CPU time [hr]**
2	14565	300	3001	4.86	15	51076	0.1664	0.75	6.69
3	14565	300	1501	9.71	15	25538	0.3328	0.75	1.78
4	14565	300	3001	4.86	15	51076	0.1664	0.75	6.69
5	14565	300	4501	3.24	15	76614	0.1109	0.75	16.07
6	14565	300	6001	2.43	15	102151	0.0832	0.75	34.92
7	14565	300	7501	1.94	15	127689	0.0666	0.75	92.84

As can be seen Table 9, the computational time is more than doubled every time the number of points is increased by 5 per wavelength. In fact, the computational time seems to follow an exponential trend. This is seen on Figure 24.

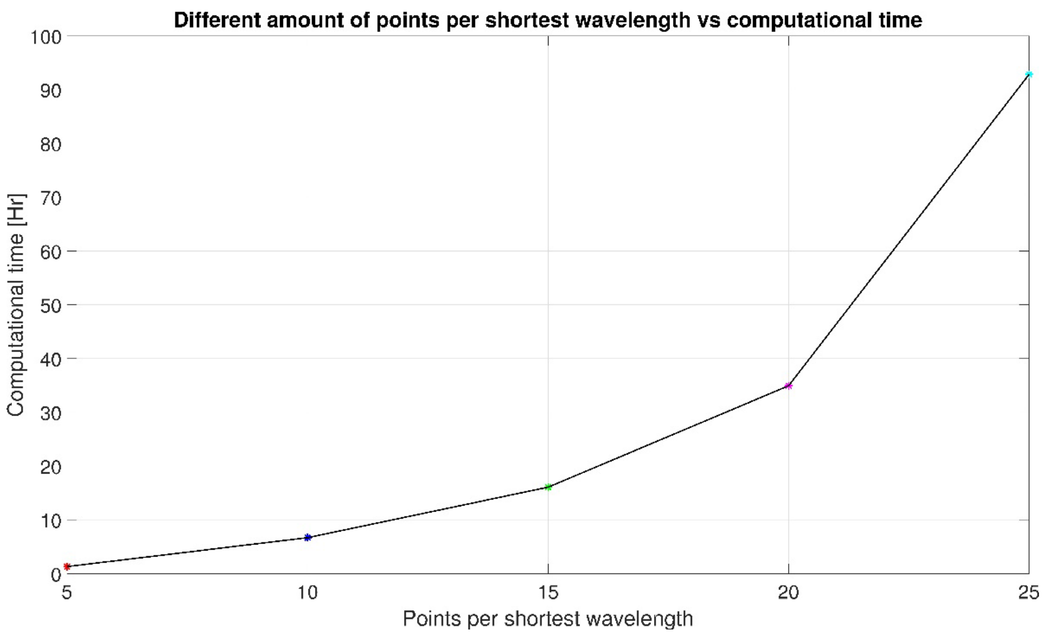

Figure 24: Computational time for different amount of Nx.

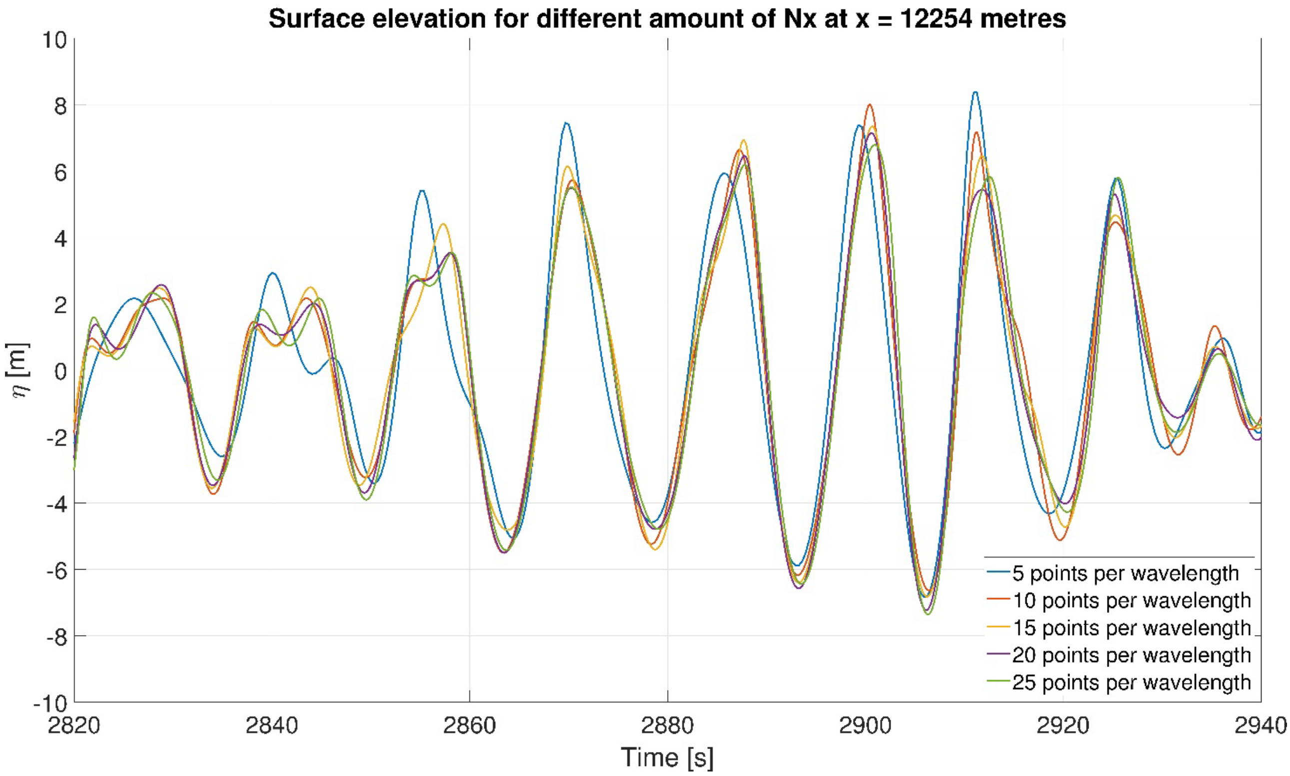

Figure 25: Zoom of surface elevation at x = 12,254 m.

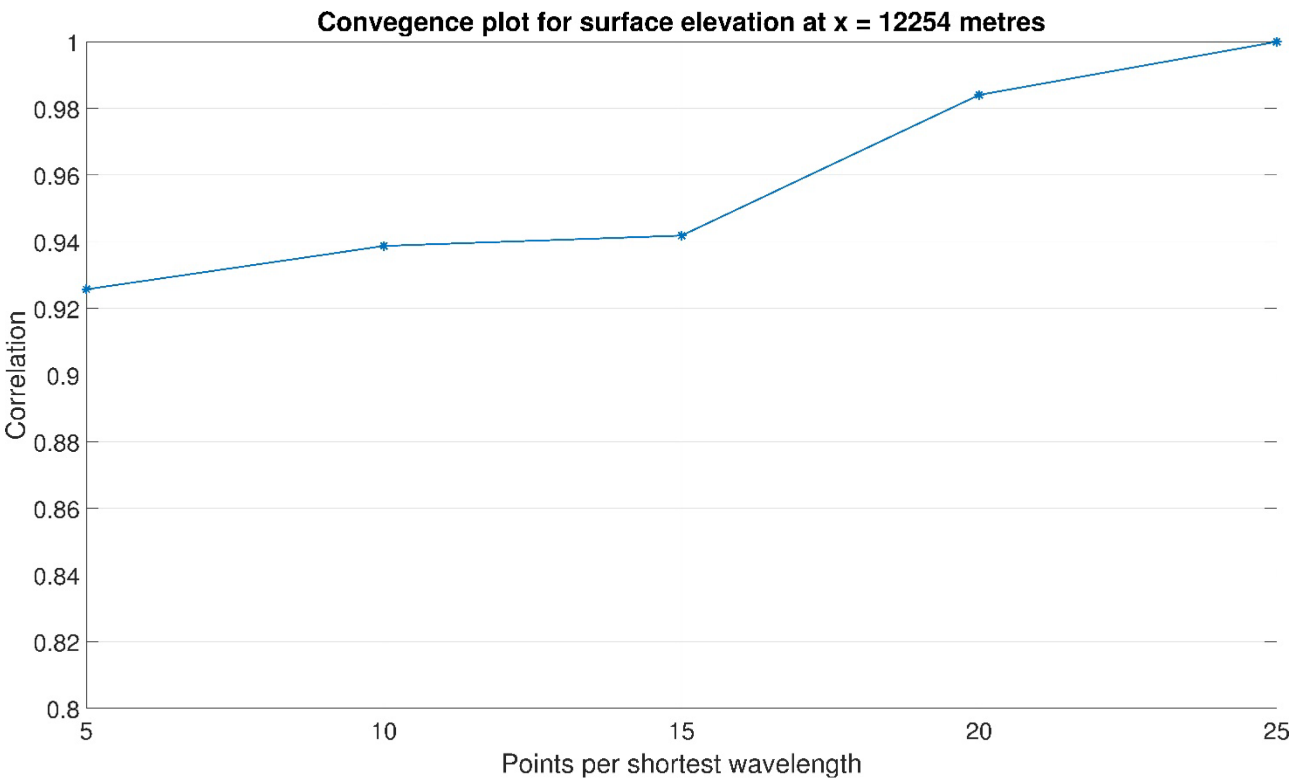

Figure 26: Correlation for different points per shortest wave, correlated to 25 points.

To get an indication of the overall wave realizations with different discretization, a zoom of the surface elevation at x = 12,254 m is shown in Figure 25. The figure is zoomed in to outline the trends of the different discretizations. The most obvious thing to notice is that the curve for the 5 points per wavelength is quite a poor fit compared to the rest of the curves, with a correlation coefficient towards 25 points per wavelength of 0.925. This especially applies to the crest height, where it seems to overestimate the height of approximately 2 m for the two crests between 2850 s and 2870 s.

However, it is not only this coarse discretization that presents discrepancies. For the large crest at around 2910 seconds, a relatively large difference in crest height between the realizations is present, with a crest height difference of more than 1.7 m between 10 and 20 points per wavelength. With discrepancies in this size region, it is interesting to see the correlation of the different discretizations towards the finest discretization of 25 points. This is shown on Figure 26.

The difference between 5, 10, and 15 points per wavelength is smaller than expected, with the correlation only increasing roughly 2 percentage points between 15 and 20 points. Hereafter, the correlation jumps to a factor just above 0.98. Hence, the biggest gain in correlation is seen when moving from 5 to 10 points per wavelength. However, it must be remembered that this correlation is only based on the surface elevation,η. To include and analyze on more wave kinematics, exceedance probability curves for depth-integrated force are investigated. This is seen on following Figure 27.

Just like in the study of the domain length, a portion of time is removed to assure that the shortest waves have propagated to the reference point of x = 12,254 m. In this case, the first 1,500 seconds are removed. For higher and intermediate probabilities, the curves are well aligned with no real striking tendencies. From 10^{-1} and downwards the curves for 15 and 20 points take on the lowest non-dimensional force values.

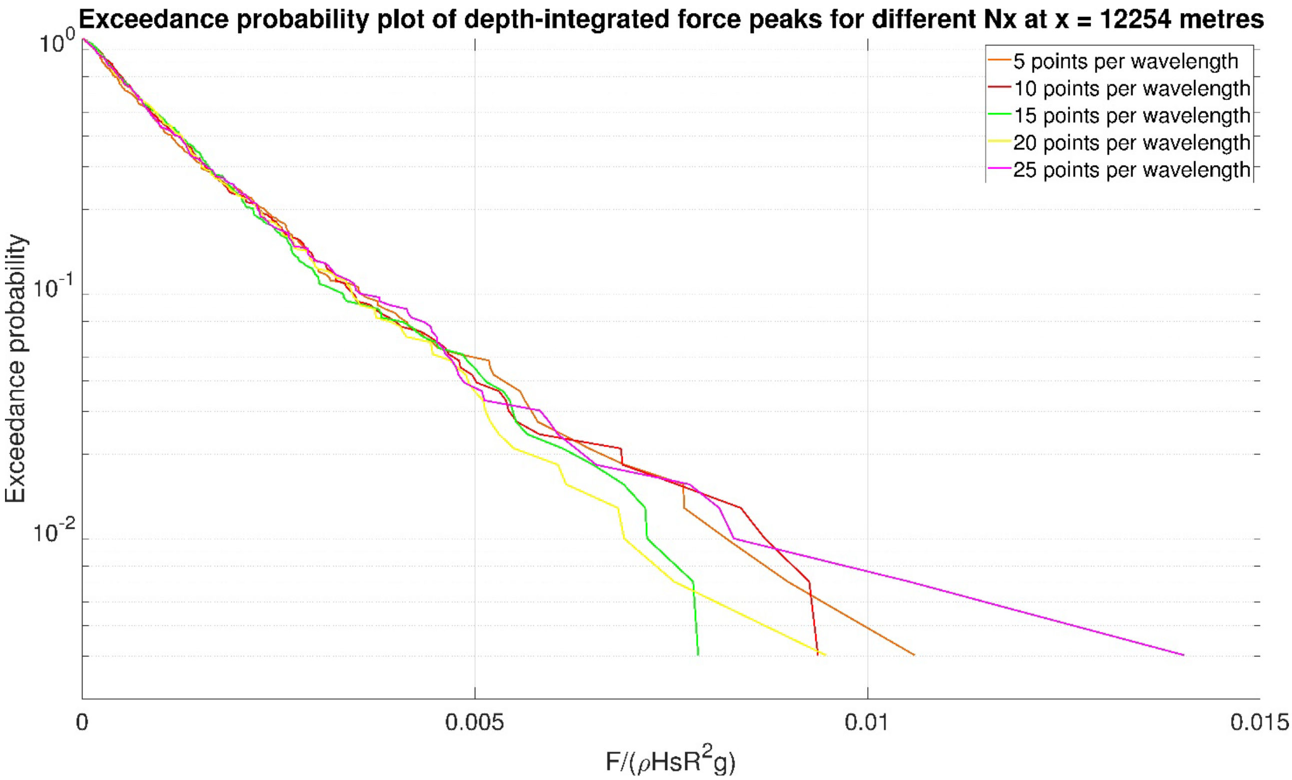

Figure 27: Exceedance probability curves for depth-integrated force peaks for different points per wavelength at x = 12,254 m.

For the lower probabilities, the most refined discretization follows that of the 5 and 10 points per wavelength until the tail is reached. The 25 points per wavelength has two values exceeding the other curves in magnitude by a large margin. For instance, the endpoint in the tail 32 % larger than the second largest, which is the case with 5 point per wavelength.

To clarify if these tendencies are recurring, the same plot as the above is made, however now with mean values for 5 x-values on both sides of the initial point of investigation in the numerical domain. Figure 28 is thus showing exceedance probability curves for depth-integrated force values averaged over 11 x-values, placed between 12,157 m to 12,351 m. The spacing between the coordinates in the numerical tank is 19.4 m.

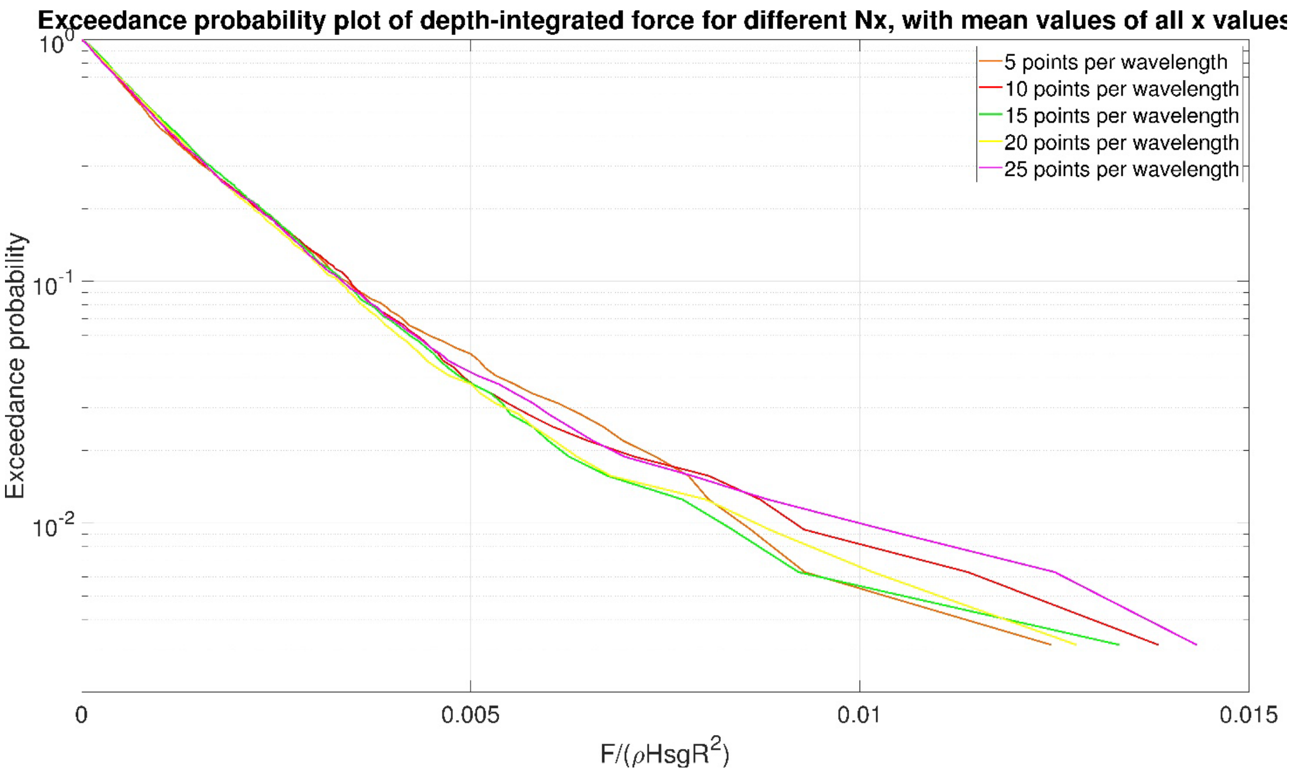

Figure 28: Exceedance probability curves for depth-integrated force peaks for different horizontal discretizations.

The first thing noticed is that the curves are smoother looking than those seen for one coordinate. However, the tendencies are quite alike. The distribution between the curves from 10^{-1} and downwards is similar, except the curve for 5 points per wavelength, which now overpredicts the force at the intermediate exceedance range. Meanwhile, the tail of the same curve is now positioned more to the left, relative to the other curves.

Generally, it is found that the curve for 25 points per wavelength has maintained its tail value, whereas the remaining curves have experienced quite an increase. Here the 15 and 25 points only result in 89 % and 93 % of the force predicted by the 25 points per wavelength. Further, the curve for the 10 points per wavelength, despite having the second-lowest correlation in terms of surface elevation, seems to be a better fit in terms of force.

The simulation results are now compared in the frequency domain by exploring wave spectra to investigate the different discretizations further. The following Figure 29 shows the wave spectra for the four different number of points per wavelength compared to the fifth and finest of 25. As in the domain length study, a

Hanning window is applied before the Fourier transformation. Further, the data is averaged over segments of 20 values. Finally, the 2 % energy content of peak frequency is indicated by a vertical black line.

Common for the 4 sub-figures is that a generally good correlation is seen at the frequency range around the peak frequency. Some discrepancies are observed for the lower frequency range, which, however, do decrease as the number of points per wavelength increases.

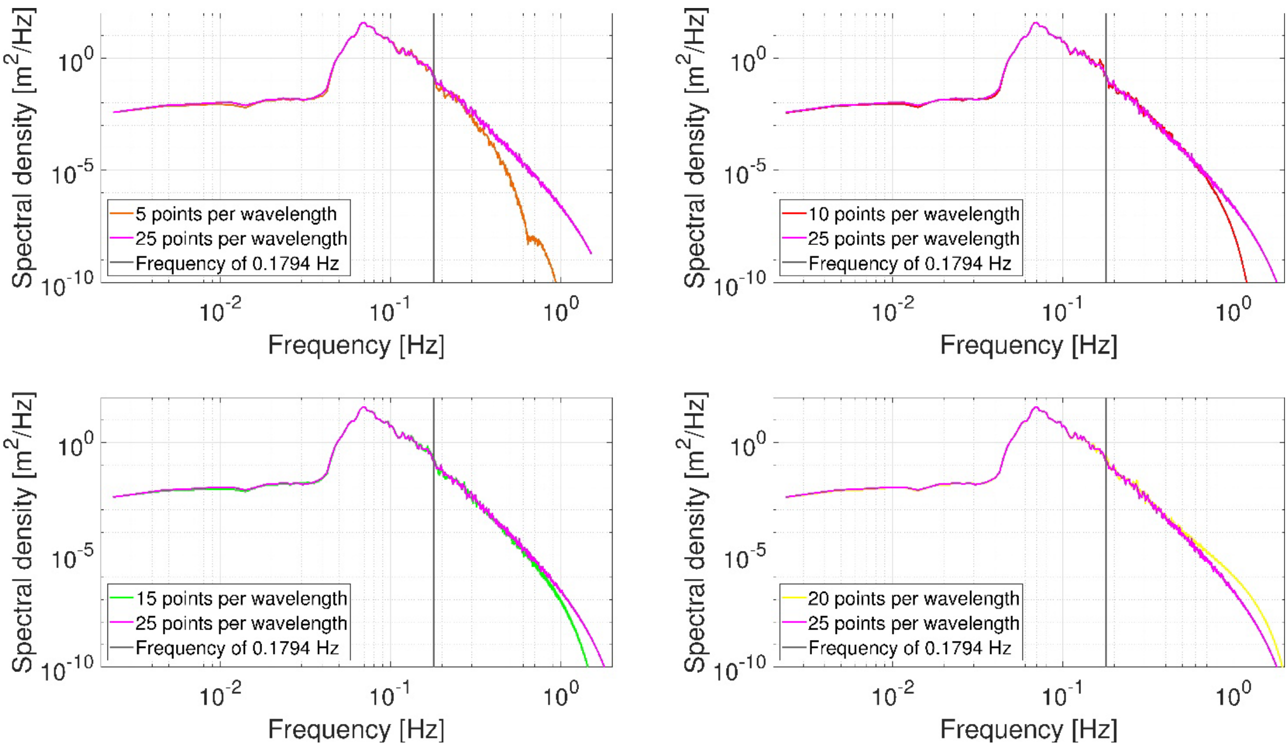

Figure 29: Segmented wave spectra for different points per wavelength compared to 25 points. Hanning window applied and top 2% of peak frequency energy indicated by the black line.

An interesting thing to notice is how 5, 10, and 15 points per wavelength underestimate the energy at the highest frequencies, while 20 points per wavelength overestimate it. For the latter case, it seems as if more energy is relocated to higher frequency levels, which could indicate these waves behaving more nonlinearly. However, it is noted that 15 points per wavelength match the wave spectrum of the 25 points per wavelength the best for this inspection. A convergence plot for the different power spectra is created to get a better overview of how well the different spectra converge towards the finest discretization. This is seen on Figure 30.

The red and blue lines indicate the entire power spectrum with and without segmentation. Naturally, the spectrum with the segmentation will show the highest levels of correlation, as the curve is smoothed when values are averaged. In this case, when averaging 20 values at a time, the correlation is virtually 1 for all points per wavelength. The correlation is much lower for the case without segmentation, but the tendency with the flat convergence curve prevails. Here the correlation is almost unchanged for the different discretizations, with a correlation value around 0.7. The black and green lines indicate the correlation for the 5 % to 1% energy content of peak frequency, again with and without segmentation. For the black line without segmentation, a more gradual increase in correlation is seen than for any other case. The most significant increase in correlation is seen when moving from 5 to 10 points, resulting in a correlation increase from 0.41 to 0.51. This is expected, as this corresponds to the case with the most significant relative increase in points.

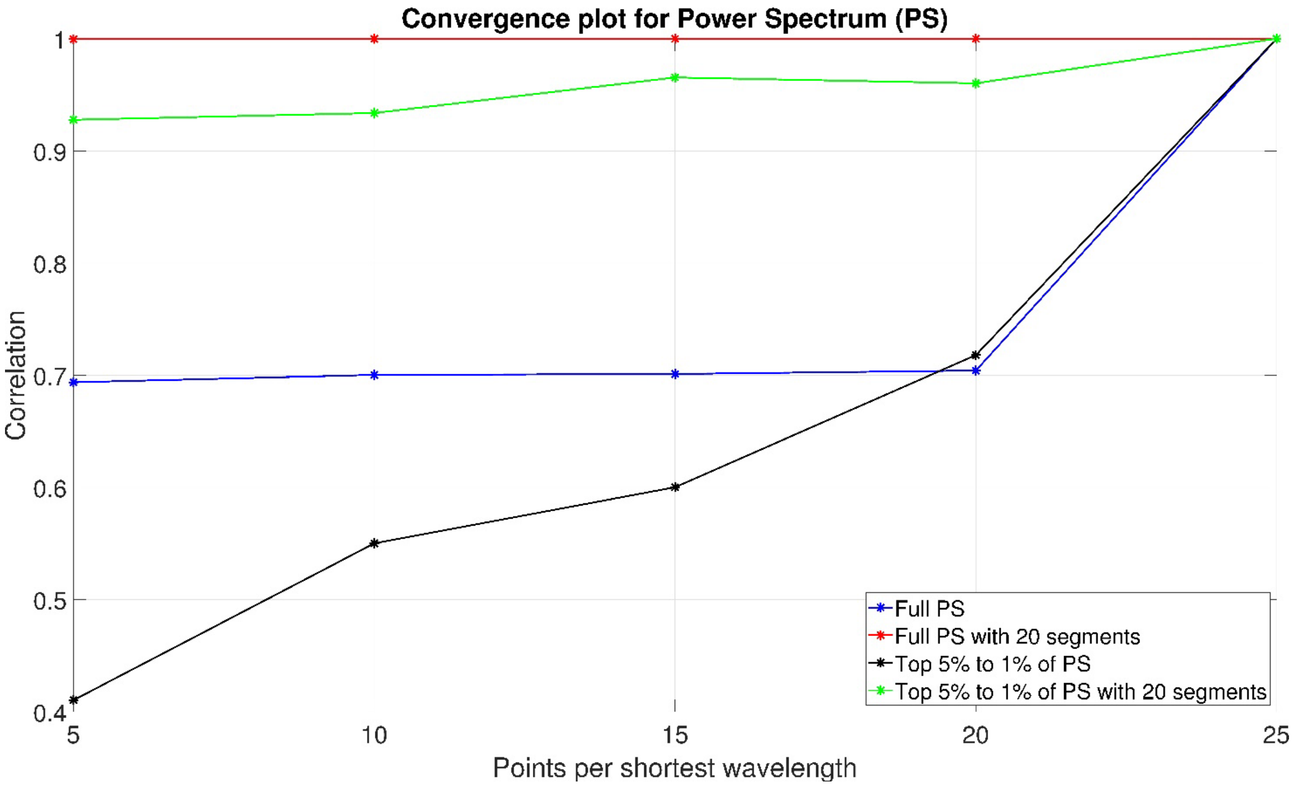

Figure 30: Convergence plot for power spectra with and without segmentation for both the entire spectra and the top 5 % to 1 % energy of peak frequency. Convergence towards the finest discretization.

For the case with segmentation (the green line), the correlation values are much larger, and the curve is much flatter, as it was for the case looking at the entire spectrum. However, by only looking at the high-frequency area, the correlation values have decreased slightly, to a level around 0.93 to 0.97. It is interesting to see how the curve presents a small spike around 15 points per wavelength, which holds a larger correlation value than 20 points. This could potentially be explained by the size of the data bundles, in which the data is averaged to create the segments. Therefore, to investigate the impact of the segment size, a small sensitivity study is carried out, with 3 different segment sizes.

The results are seen on Figure 31, where once again a convergence plot is shown, however this time it is exclusively demonstrated for the high-frequency range. Four lines are shown, corresponding to no segmentation and segment sizes of 10, 15, and 20 values.

The black and green lines correspond to the lines with the same color in Figure 30. The figure shows that a segment size of 10 does not smoothen the curve enough to achieve high correlation values. However, this segment size does seem to produce a more gradual increase in correlation. Meanwhile, it seems as if segments with data bundles of 15 and 20 values are somewhat converged, as these two lines are rather coincident. It is further seen that 15 points per wavelength still results in the highest correlation, regardless of segment size. Based on the lengthy investigations towards the horizontal discretization, it has been decided to choose 15 points per shortest wavelength. The frequency-domain analysis showed great coherency between the power spectrum of 15 and 25 points per wavelength. Even though correlating the different points per wavelength towards a higher number of points rather than a "true" solution is not necessarily correct, it still gives a great indication of behavior.

The time-domain analysis did not show the most convincing results for 15 points per wavelength, e.g., a correlation for the surface elevation of 0.94, where the 20 points per wavelength had a value of 0.98. Looking at the exceedance probability curve for the non-dimensionalized force with mean values of 11 x-values, the curve for 15 points per wavelength was lower than 25 points. However, this was the case for most of the exceedance probabilities, especially for the lower exceedance probabilities and at the tail, where 25 points presented relatively large values. Here the 15 points per wavelength were the median of the 5 discretizations. The computational time of the different discretizations is heavily influential on the decision. The computation time is more than doubled every time the discretization is increased with 5 points per shortest wavelength. As stated at the beginning of this investigation, the decision must be made by balancing accuracy and computational time. That is why 15 points per wavelength are chosen for the horizontal discretization.

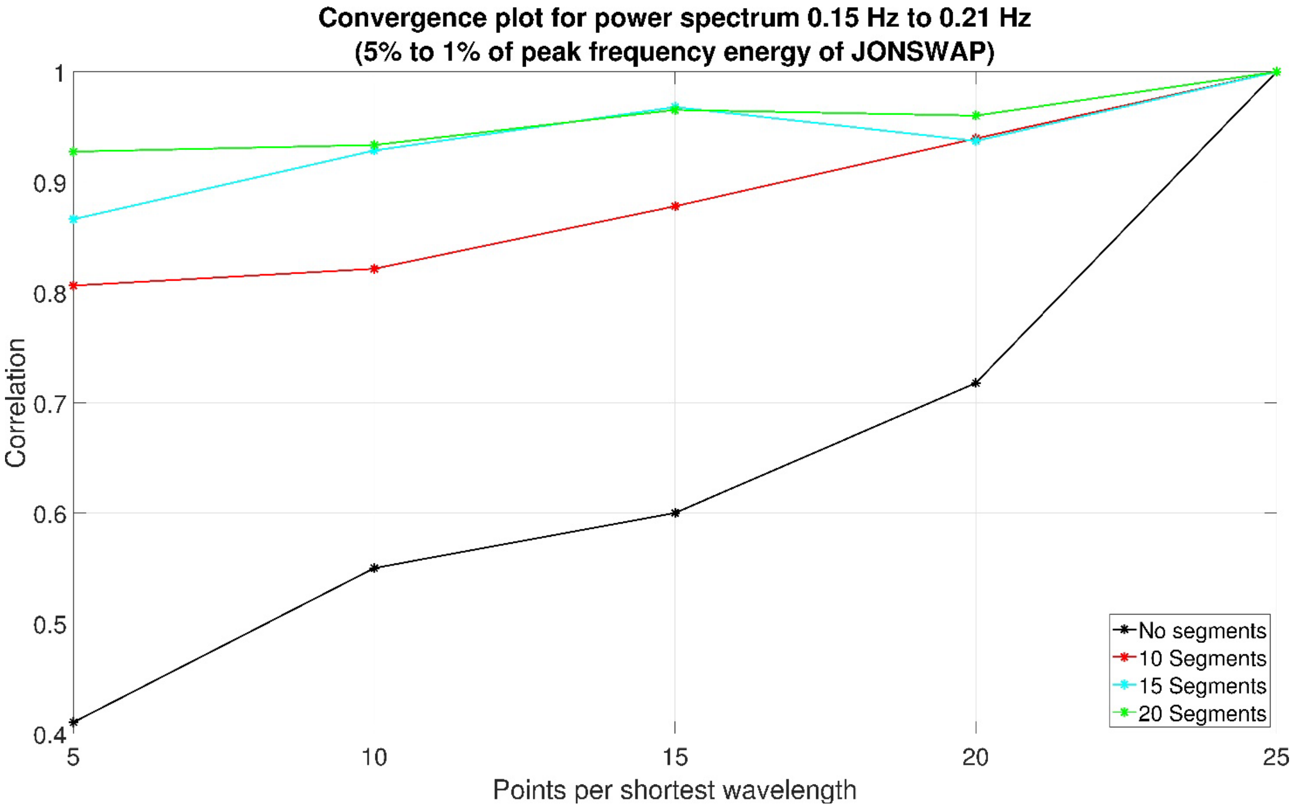

Figure 31: Convergence plot for power spectra with different segments for 5% to 1% of peak frequency energy.

4.2.3. Final domain

The domain analysis was based on Sea state 1, with parameters stemming from the COSLInnovator accident in December 2015. Sea state 1 was chosen as this sea state has the largest depth of 300 the sea state 2 and 3. As the same discretization will be used for all sea states simulations, it is reasonable to assume that solutions obtained for sea state 2 and 3 are more accurate, as the domain is smaller.

First, the overall domain length was investigated. The first step in this analysis was to let both the wave generation zone and damping pressure zone be fixed lengths. The length of the two relaxation zones was chosen to be equal to two times the expected longest wave. Through time- and frequency domain analysis based on results from 17 points throughout the numerical tank, the length was chosen to 14,565 m. This length includes the wave generation zone and damping pressure zone of 1,500 m each.

Hereafter the discretization in the horizontal and vertical direction, x and z, was investigated. It was chosen to investigate the two directions separately. As a result, the number of points in the vertical directions is only analyzed for one horizontal discretization. As the discretizations in the two directions are coupled, it could be argued that it could be relevant to investigate the discretizations simultaneously or investigate the vertical discretization for different horizontal discretizations. However, this study chose to handle the two studies separately, thus isolating the variables. By following this procedure, a more detailed indication of the impact of different vertical discretizations was achieved. The discretization in the horizontal and vertical directions were chosen to Nx = 4501 and Nz = 16 points.

Thus, the physical properties are in order, and the numerical domain can be illustrated. This is done in Figure 32.

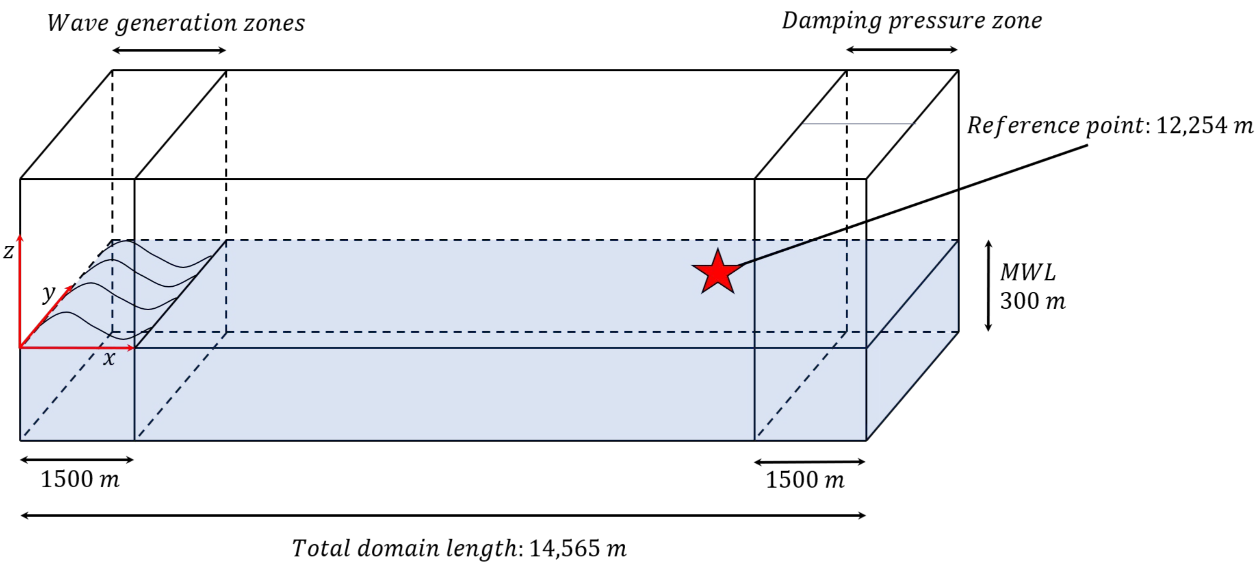

Figure 32: Illustration of the final domain for large-scale simulations of the three sea states. Note that the depth for simulations of Sea state 2 and 3 is 90 m, rather than the 300 m shown.

Up until this point, the entire domain analysis had been based on a Courant number of 0.75. As no real fluctuations on the convergence plot for surface elevation were observed, and the exceedance curves for crest height and depth-integrated force were well aligned for the different Courant numbers, a Courant number of 0.75 was chosen.

4.3. Analysis of simulation results

This section will present an analysis of the results from the simulations. All three sea states are run for the three different wind speeds. For convenience, the parameters for the three sea states are repeated in the following Table 10, which also presents computation time. The three sea states will be run for 0, 24 and 29.5 m/s, the latter corresponding to the 3 second gust wind, found in previous section on sea states. As for the domain analysis, results will be shown at location x = 12,254 m.

Table 10: Simulation parameters for large scale simulations.

Wind Speed [m/s]	Sea state	H_s [m]	T_p [s]	d [m]	Nt [-]	dt [s]	CPU time [hr]	PC no. [-]
W = 0	1	9.5	14.29	300	150,000	0.1109	37.29	1
	2	9.0	10.53	90	150,000	0.1109	31.15	2
	3	10.0	14.29	90	150,000	0.1109	37.32	3
W = 24	1	9.5	14.29	300	150,000	0.1109	36.67	1
	2	9.0	10.53	90	150,000	0.1109	30.27	2
	3	10.0	14.29	90	120,000	0.1109	32.46	3
W = 29.5	1	9.5	14.29	300	150,000	0.1109	46.90	4
	2	9.0	10.53	90	150,000	0.1109	48.71	6
	3	10.0	14.29	90	150,000	0.1109	41.20	5

As can be appreciated from the previous Table, the simulation for Sea state 3 with W = 24 m/s is only run with 120,000 number of time steps as opposed to 150,000 for the remaining simulations. The reason for this is that the simulation ran unstable past this point. The consequence of this is that only 960 waves are generated for that specific singular case.

4.3.1 Significant wave height, crest height, and steepness

This section will investigate the large-scale simulations' results and comment on trends in the data in terms of significant wave height, crest height, steepness of the waves, and particularly the wave-induced load.

The following Table 11 presents an overview of significant wave height for the different sea states and wind speeds. From the Table, Sea state 1 and 3 holds similar values for height and seem to follow the same trend. As the wind is applied, the significant wave height increases, and when the wind speed increases further, the height decreases. For Sea state 1, this decrease is negligible, but for sea state 3 increasing the wind causes a large decrease to a value lower than before the application of wind.

Table 11: Overview of significant wave height for the three sea states.

	Significant wave height [m]		
	W = 0 m/s	**W = 24 m/s**	**W = 29.5 m/s**
Sea state 1	8.89	8.95	8.94
Sea state 2	6.73	6.56	6.55
Sea state 3	9.14	9.18	9.03

Sea state 2 holds by far the lowest significant wave height. Unlike the other two sea states, Sea state 2 starts decreasing with the introduction of wind and seems to stabilize at a lower height, even though the wind is increased. While the sea state is initially defined by the lowest wave height, the explanation for the low height and behavior after wind application should most likely be found in the severity of the sea state, which will be further explored later in this section. As a reminder, Figure 18 showed the diagram for wave theory validity with the sea states indicated, where Sea state 2 was seen to be the most nonlinear sea state.

For the analysis of crest height of the three sea states, the following Figure 33 is used. For the first sea state, it is seen how the case with W = 0 m/s produces larger crests between exceedance probabilities of $2 \cdot 10^{-2}$ and $4 \cdot 10^{-3}$ than for the cases with the wind. This could indicate the waves breaking in this region, thus causing lower crest heights. However, looking at the tail, the wind speed of 24 m/s has the highest crests, followed by the gust wind speed. This overall trend is also observed for the second sea state, although, here, the gust wind speed produces higher crests until the exceedance probability of 10^{-2}. It seems as if the wind decreases the crest height for the second sea state from this point and downwards. However, by increasing the wind speed, the crests reclaim some of the lost height. Once again, the wind speed of W = 24 m/s results in the largest crest, again followed by the gust wind case, except for the very last point of the tail where W = 0 m/s has one exceeding value. Increasing the wind further for this sea state seems to increase the crest height but might eventually lead to further wave breaking. This could explain why the gust wind produces a lower crest at the last point of the tail than the case without wind.

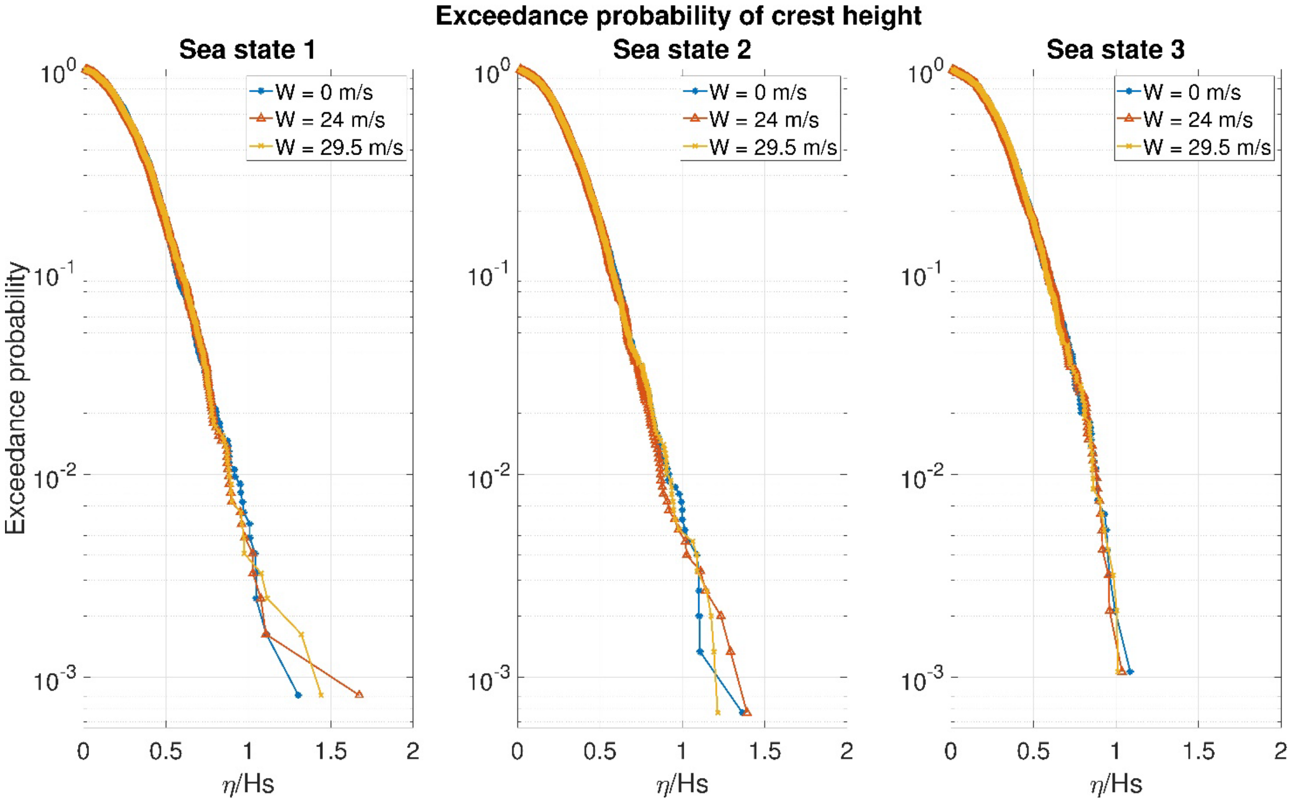

Figure 33: Exceedance probability curves for normalized crest height for the three sea states.

The third sea state shows a high correlation between the cases with and without wind. A likely explanation for this is that these waves are not steep enough to exceed the defined threshold for the wind application, and the wind is thus not applied. Hence results will be similar. This is common for all three sea states at the higher exceedance probabilities, where the values coincide.

For the three sea states, it is observed that when energy is transferred from the wind to the waves, there is a relatively high degree of correlation until exceedance probabilities around 10^{-2}, where the case without wind produces larger crests. Then, looking at the tail of the exceedance probability curves, the largest events are dominated by the crests with wind applied. Based on this, it is expected to see an increase in wave-induced load from extreme events. However, it is kept in mind that the largest events do not necessarily produce the largest forces. Thus, the steepness of the waves is investigated, as the highest loads usually come from the steepest waves.

As a measure of the steepness of the three sea states, the steepness of the front of the wave is used. This is calculated based on the definitions of \citet{kjeldsen1979breaking}. The crest front steepness is used instead of the total steepness (η/L) as for non-steady asymmetric waves, the total steepness is not accurate enough. Asymmetric waves can exist with the same total steepness but with very different steepness of the wave crest, \citet{kjeldsen1979breaking}.

The crest front steepness is found by:

$$\varepsilon = \frac{\eta'}{L'} \tag{19}$$

Where η’ and L' are indicated on Figure 34

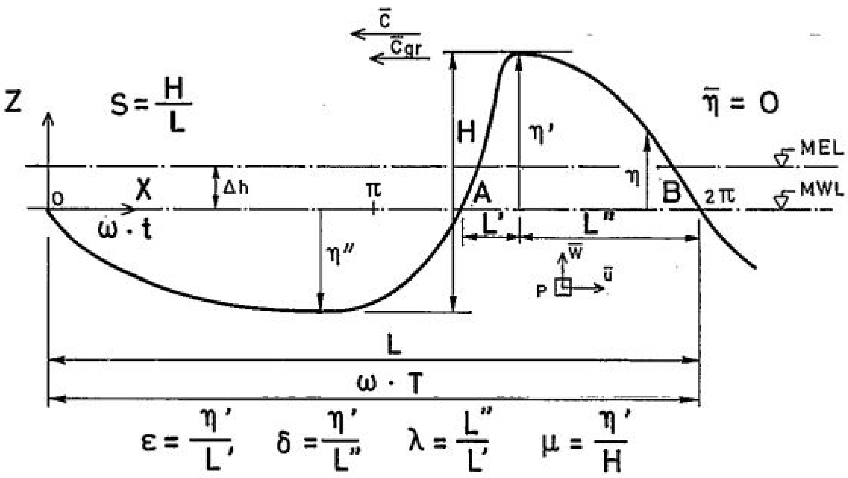

Figure 34: Definitions of wave characteristics according to \citet{kjeldsen1979breaking}.

Once these are found, scatter plots indicating crest front steepness can be generated for each sea state, the first of which are shown on Figure 35.

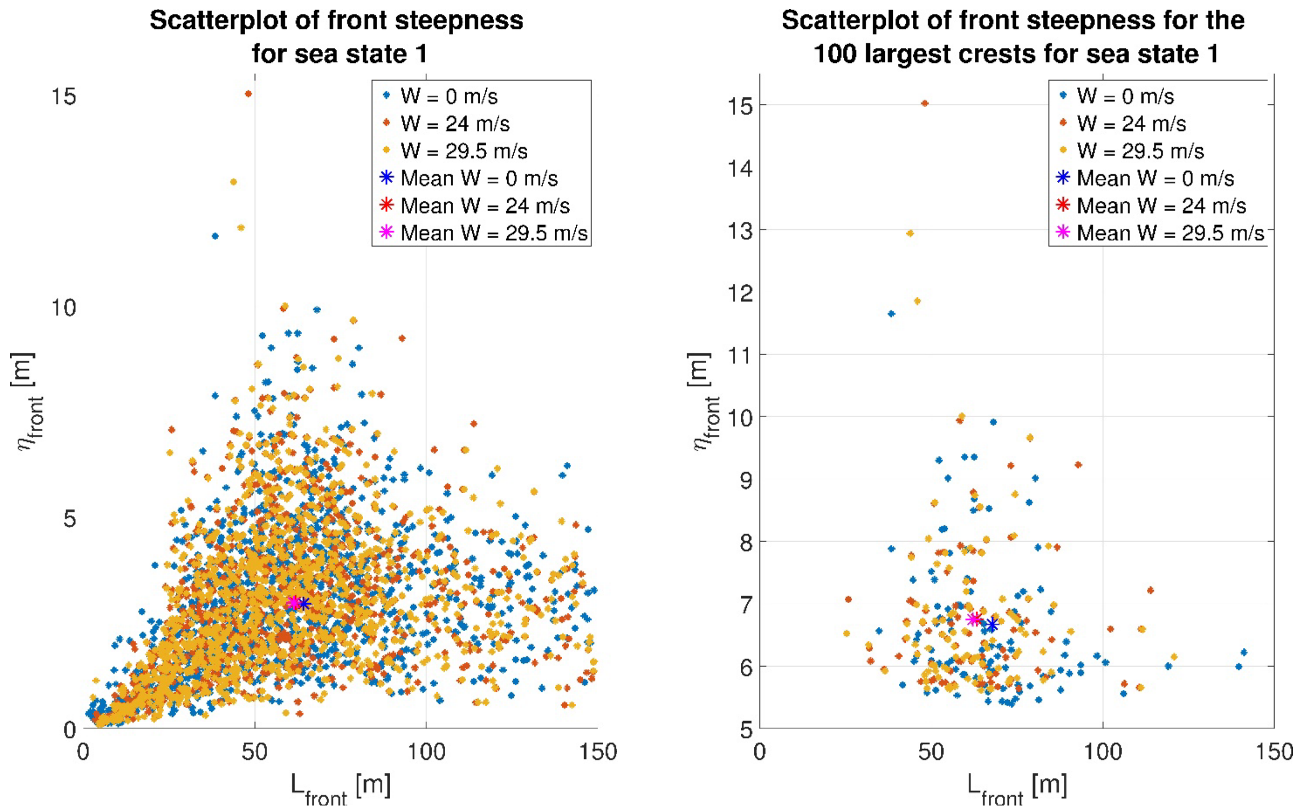

Figure 35: Scatter plot of crest front steepness for Sea state 1.

The left plot shows values for Sea state 1 for all three wind speeds for all crests, with a mean value for each wind speed. The plot to the right shows the same, but only for the 100 largest crest events. The trends are less pronounced when looking at all events than the 100 largest events, as these are the extremes. By observing the mean values for the 100 largest crest events, Sea state 1 is steepened by 7 % with the introduction of wind and further increased 2 % when increasing the wind speed. An overview of the front steepness values for all events and the 100 largest events is found within Table 12, where also the percentage increase or decrease is shown.

Table 12: Overview of mean crest front steepness steepness for the three sea states with different wind speeds for all events and 100 largest events.

	Factor of crest front steepness compared to W = 0 m/s					
	All events			**100 largest events**		
	W = 0 m/s	**W = 24 m/s**	**W = 29.5 m/s**	**W = 0 m/s**	**W = 24 m/s**	**W = 29.5 m/s**
Sea state 1	1.00	1.05	1.06	1.00	1.09	1.10
Sea state 2	1.00	0.97	0.98	1.00	0.91	0.95
Sea state 3	1.00	0.98	1.00	1.00	1.00	0.99
	Crest front steepness values					
Sea state 1	0.046	0.048	0.049	0.098	0.107	0.109
Sea state 2	0.055	0.053	0.054	0.137	0.124	0.130
Sea state 3	0.049	0.048	0.049	0.099	0.099	0.098

The mean values for the two cases for the largest 100 crest events with wind is shifted to the left and a bit upwards, hence also the crest height is slightly increased, with an increase of 1.3 % and 1.2 % for wind speeds of 24 and 29.5 m/s respectively. A slight increase in steepness is seen when increasing the wind from 24 m/s to 29.5 m/s. However, the change is negligible for this sea state. It is as if the sea state is saturated after the first wind speed application. However, as both the crest height and the steepness of the extreme events are seen to increase when the wind is applied, the wave-induced load is expected to increase as well.

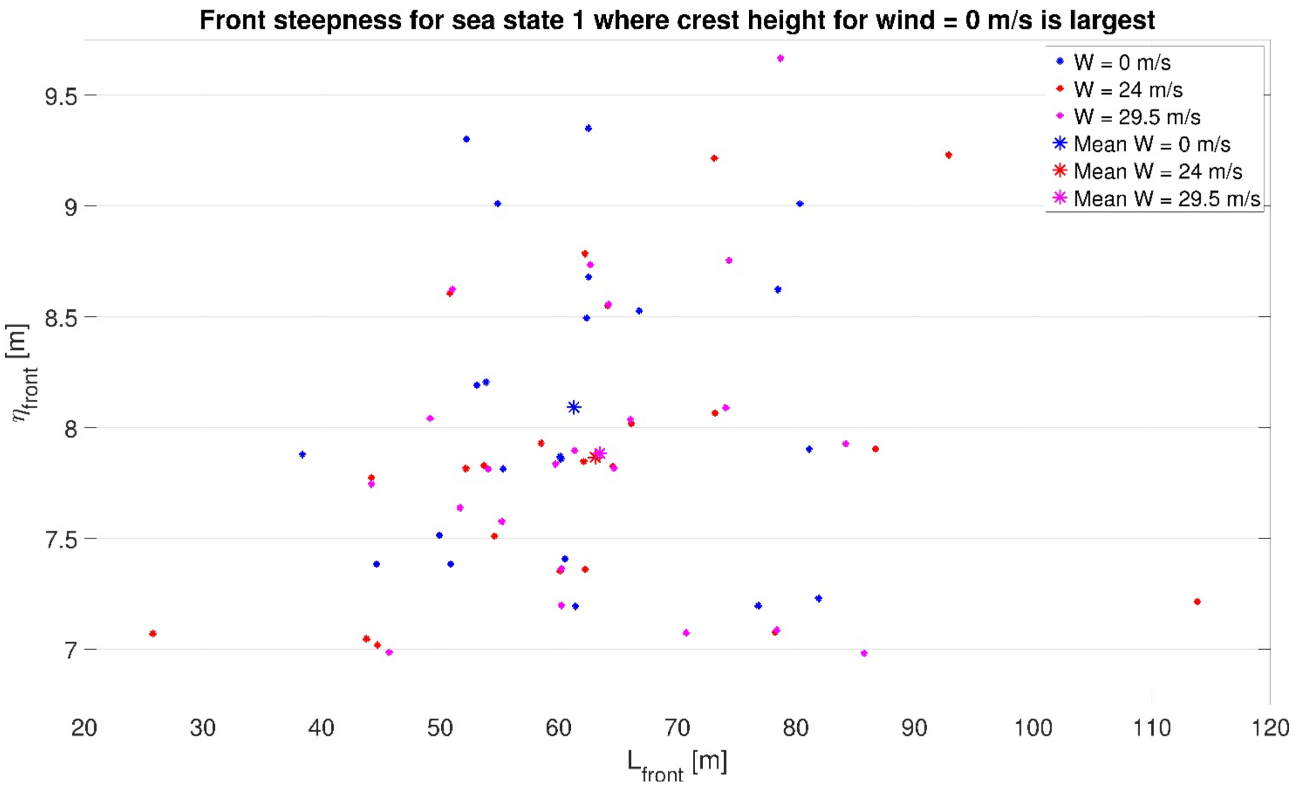

Figure 36: Scatter plot of crest front steepness for sea state 1 for waves with higher crest values without wind.

To investigate the steepness of the waves in the sea states for the wave cases where no wind results in the largest crests, the following Figure 36 is plotted showing crest front steepness of Sea state 1 for the three different wind speeds. Sea state 1 is chosen as sample, as it is for this sea state that the trend is most pronounced. The plot is based on waves from Figure 33, with exceedance probabilities between $2 \cdot 10^{-2}$ and $3 \cdot 10^{-3}$.

On Figure 36 it is seen how both the crest is decreased, and the length is increased, with the introduction of wind, thus resulting in a less steep sea state. An explanation of this could be that the portion of waves for inspection is already steep, based on the mean value shown on the plot, and waves are already breaking. By introducing wind, the same level of steepness is not obtained as the waves are already breaking, thus most likely leading to fewer breaking waves with wind for these waves. Breaking waves will be further discussed in the next subsection.

The scatter plot for the crest front steepness of Sea state 2 is seen on following Figure 37:

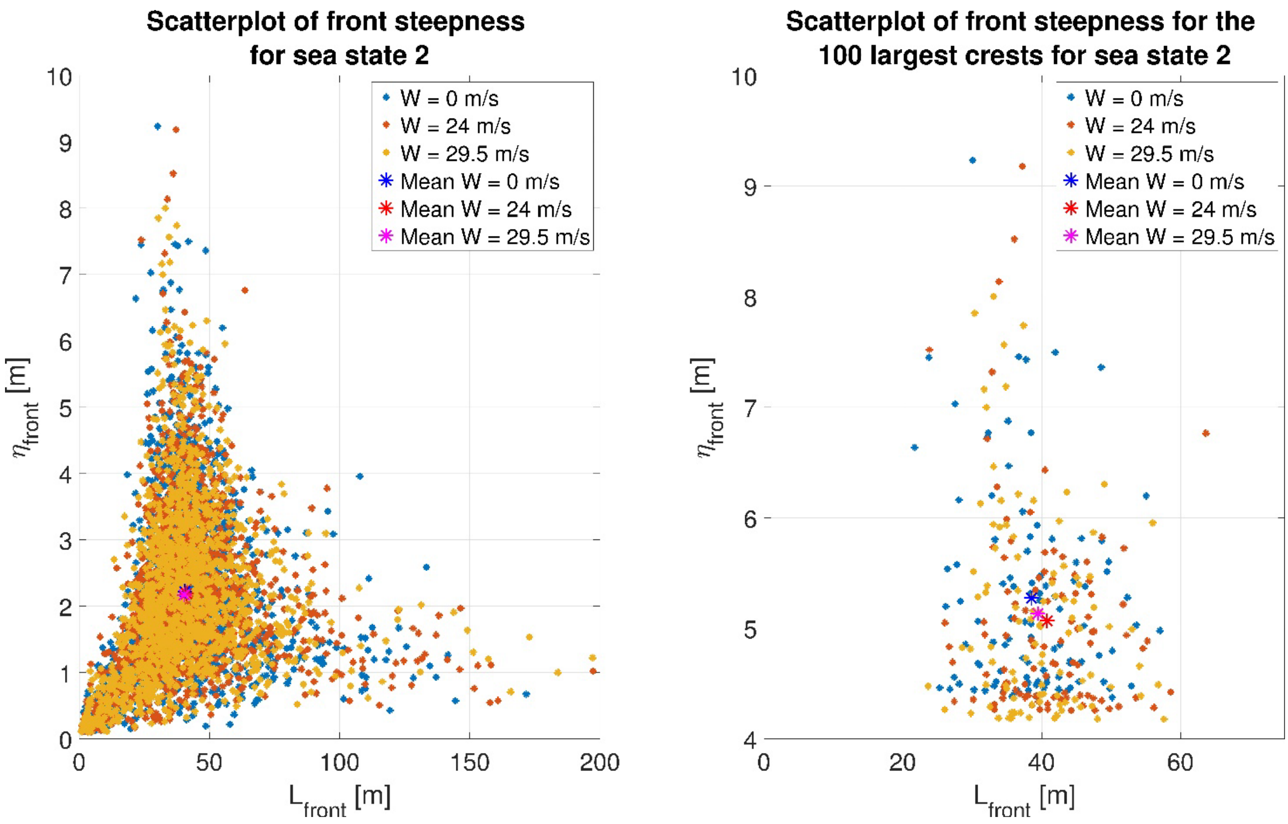

Figure 37: Scatter plot of crest front steepness for Sea state 2.

As it can be appreciated from the figure, the crest front height is decreased heavily compared to the previous sea state, just as it was the case for the significant wave height. However, the corresponding front wavelength is low, making Sea state 2 the steepest of the three sea states. Further, it is interesting to note that it is only for the largest 100 crest events that the crest height is increased when increasing wind from 24 m/s to 29.5 m/s. For the left plot of Figure 37, considering all crests, the crest height is in fact decreased when increasing the wind from W = 24 m/s to W = 29.5 m/s. Nonetheless, are the case is still steepened as the length of the front wave is decreased. Thus, as for Sea state 1, it is expected to see an increase in the wave-induced loads for the extreme events.

Sea state 3 follows the trend of Sea state 2, in terms of steepness for all crests. Applying wind decreases the steepness, but further increasing the wind increases the steepness once again. These trends are shown on Figure 38. However, looking at the largest 100 crest events, the steepness decreases with the introduction of wind and keeps decreasing with increasing wind speed.

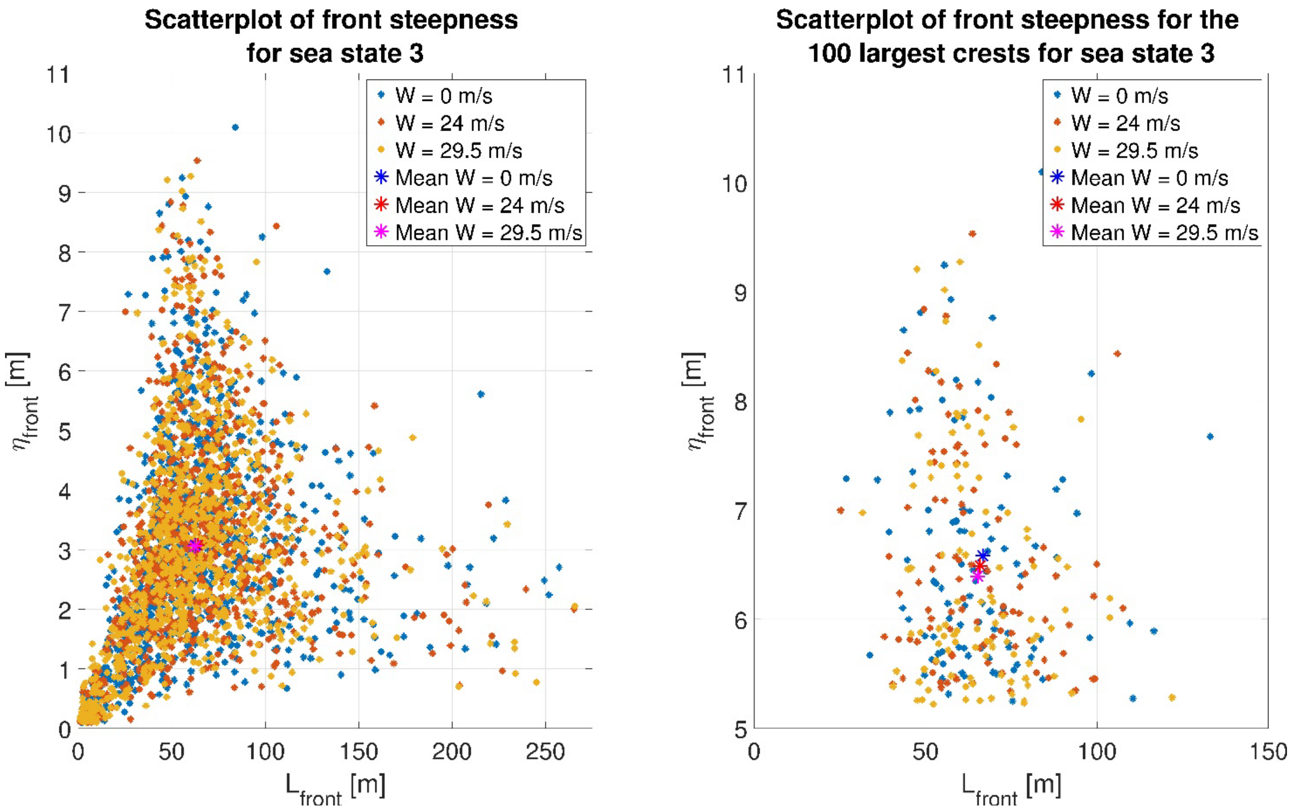

Figure 38: Scatter plot of crest front steepness for Sea state 3.

The main reason for the decrease in steepness for all crests when applying wind is that the length of the front of the wave is increased significantly, from 62.66 m to 63.82 m. Furthermore, the figure shows how the crest height decreases upon the introduction of wind and continues to do so when the wind speed is increased. As both the crest height and steepness of the extreme events are seen to decrease, it is expected to see a decrease in the wave-induced load.

Looking at the three figures, Figure 35, Figure 37 and Figure 38, the steepness of all events and the 100 largest events is affected when applying the wind. In Table 12 the average value of the front steepness is shown alongside the factor indicating the change in front steepness compared to W = 0 m/s for each sea state.

The effect of the wind is seen to have a more significant impact on the 100 largest events than all events. Here the change indicated at the top of the table, shows that applying the wind can both decrease and increase the front steepness, which is seen for Sea state 1 and 2, or do virtually nothing, which is seen for Sea state 3. The decrease seen in sea state 2 could be due to the sea state initially being steeper than the other sea states. However, the results of Sea state 1 and 3 were expected to be more aligned as the initial steepness for the sea states is similar. This is seen by the lower part of the table, where the values of Sea state 1 and 3 are coinciding.

4.3.2. Breaking waves

Breaking waves can not be modeled through OceanWave3D as it is built on a potential flow model. However, breaking waves and near-breaking waves are of interest as the slamming load can largely increase the force on offshore structures. Thus, another way of defining waves of interest is sought. The previous section showed an illustration with wave characteristics showing the crest front steepness, see Figure 34. A breaking criterion is defined within \citet{kjeldsen1979breaking} for the front steepness of the wave:

$$0.32 < \varepsilon < 0.78 \tag{20}$$

However, plotting the equation above, none of the largest 100 events could be categorized as breaking. An explanation of this could be that the breaking filter in the OceanWave3D model has activated. As the simulation runs, a log file is generated that records all instances when the breaking filter is activated. Each time the breaking filter is activated, the following is recorded; the time, the x position, the y-position, and the values of the downwards acceleration. The lines in the log file for the breaking filter are sorted with respect to time. A set of criteria is made to count the number of breaking waves within the log file.

First, if the new line presents a time value found in any of the previous lines, and the x values are within one peak length of one another, the line is not counted as a new breaking wave. Second, if the new line presents an x value found in any of the previous lines, and the time values are within one peak period of one another, the line is not counted as a new breaking wave. Third, if the new line presents a new x-position and time value, the difference in time compared to the previous lines is multiplied with the peak celerity. This distance is added to the x value of the line, and if the sum lies within one peak wavelength of any previous lines, the line is not counted as a new breaking wave. Besides the above criteria for a line to be considered a new breaking wave, only the instances happening within one peak wavelength on both sides of x =12,254 m is of interest. The time before the sea states is entirely generated at this location is also disregarded. The final number of breaking waves for each sea state at each wind speed can be found in Table 13 together with the parameters of the peak wave used to define a breaking wave.

Table 13: Number of breaking waves found from the log file from the breaking criteria and the wave parameters used to find the amount.

	Number of breaking waves			**Wave parameters**		
	W = 0 m/s	**W = 24 m/s**	**W = 29.5 m/s**	**λ_p [m]**	**T_p [s]**	**c_p [m/s]**
Sea state 1	31	3	2	318.96	14.29	22.33
Sea state 2	58	67	74	173.17	10.53	16.45
Sea state 3	85	110	137	318.96	14.29	22.3

Using the set of criteria to count the number of breaking waves from the log file, an indication of the number of breaking waves within each simulation is achieved. However, it is essential to keep in mind that the breaking filter implemented in the simulation is highly non-physical. Hence, the above table can not be treated as a correct number but only as an indicator of the amount of breaking in the simulations. The reason why none of the waves exceed Kjeldsen's breaking criteria could be that the breaking filter in OceanWave3D is limiting the development of the waves.

The original definition of the breaking criteria for front steepness as well as the 50 % and 75 % quantile are shown together with the 100 largest events for each sea state. The largest 100 front crest events of all wind speeds in each sea state are shown alongside the breaking criteria and the quantiles of this, in Figure 39.

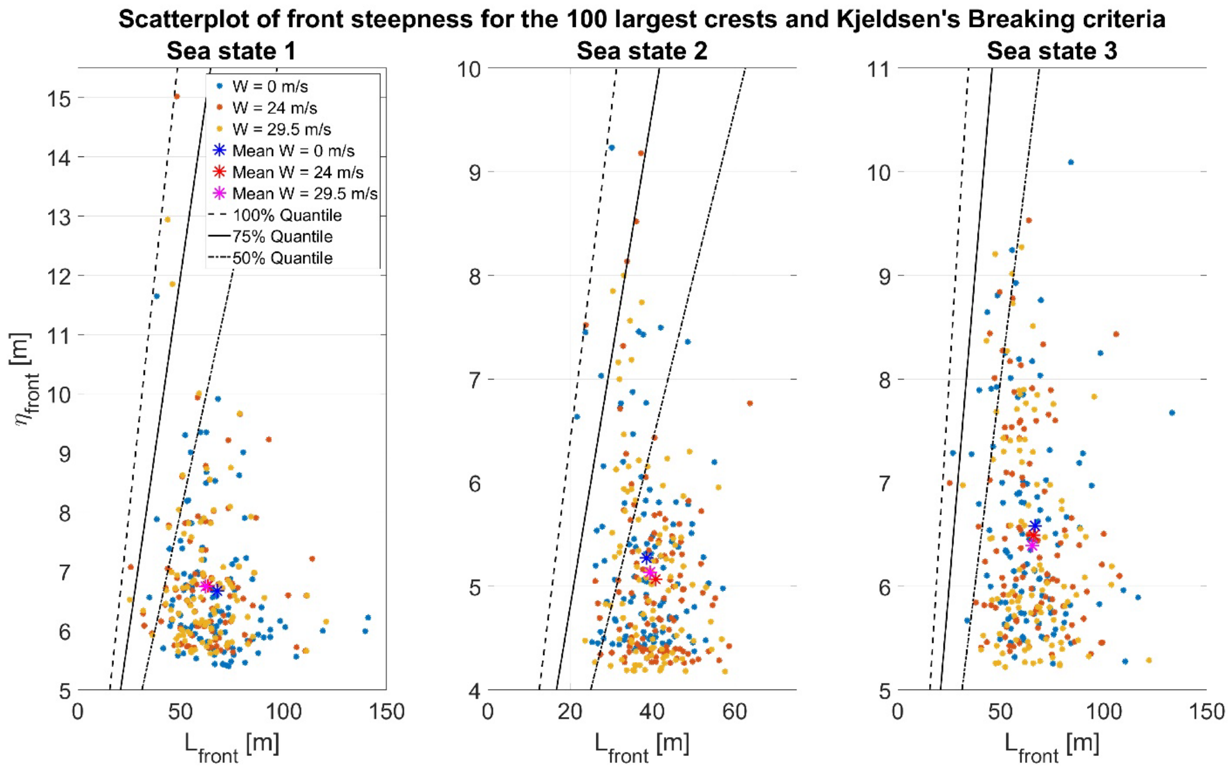

Figure 39: The largest 100 front crest events of each wind speed for all sea states compared to the breaking criteria of \citet{kjeldsen1979breaking} together with the 75 % and 50 % quantile.

Comparing Figure 39 with the number of breaking waves found from the log file, it is found that when the number of breaking waves increases in Table 13, the number of extreme events placed above the quantiles of the breaking criteria decreases. The number of waves above each quantile is found in Table 14.

Table 14: Number of extreme events above quantiles of Kjeldsen's breaking criteria, the \$100\%\$ quantile is not reported, as no event in any sea state exceeded it.

		Number of extreme events		
		W = 0 m/s	**W = 24 m/s**	**W = 29.5 m/s**
Sea state 1	75 % quantile	1	2	3
	50 % quantile	6	9	9
Sea state 2	75 % quantile	4	3	2
	50 % quantile	26	14	24
Sea state 3	75 % quantile	1	1	0
	50 % quantile	10	6	5

Correspondingly, for sea state \$1\$, the number of breaking waves decreases with the wind as seen in Table 13, and hence the number of extreme events placed above the quantiles increases as seen in Table 14.

From Table 14 the number of steep events is decreasing for Sea state 2 and 3, while increasing for Sea state 1. Therefore, the probability of a slamming load increases in two out of three sea states when the wind is introduced. By further increasing the wind, both Sea state 1 and 2 indicate that the extreme events are steepened, and for Sea state 2s, the number of steep events is almost the same as without wind. Thus, the risk of slamming loads from the extreme events is further increased. For Sea state 3, the number of extreme events above the quantiles decreases when increasing the wind. However, the number of breaking waves is increased, thus overall increasing the probability of slamming loads.

4.3.3. Force

For the force, both the exceedance probability curves for the depth-integrated force and the curves for the line force in specific depths will be shown. In this chapter, the exceedance probability plots for all three sea states are presented together. The exceedance probability curves for the depth-integrated force peaks are found in Figure 40.

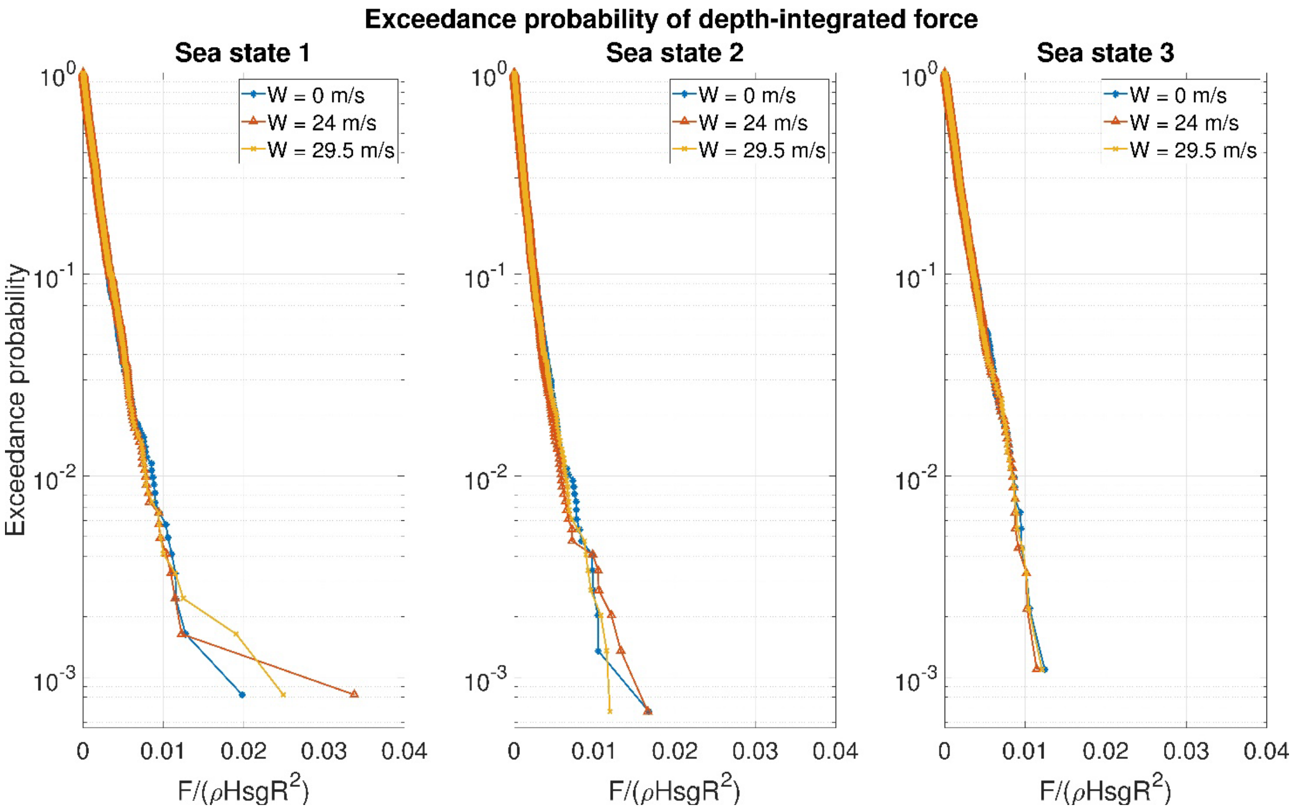

Figure 40: Exceedance probability curves for different wind speeds for each sea state.

For Sea state 1, the force at the tail is increased when the wind is introduced. A heavy increase in the last value is seen for both wind speeds. In Sea state 2, the force at the tail is also increased. However, at the last point, a slight decrease is seen for both wind speeds. An explanation of this phenomenon could be that when the wind increases above a threshold, the sea state becomes too severe, and the waves start to break. Therefore, this single extreme event must initially have been too severe to further increase in height, steepness, and force. For Sea state 3, a slight decrease is seen for W = 24 m/s, however besides this, no significant change in the tail of the exceedance probability curve is observed.

Table 15: Overview of force factor for the last three points of the exceedance probability curve relative to the case without wind.

	Factor of force compared to W = 0 m/s					
	W = 24 m/s			W = 29.5 m/s		
	3rd last	2nd last	Last	3rd last	2nd last	Last
Sea state 1	0.99	0.96	1.71	1.08	1.49	1.26
Sea state 2	1.16	1.27	0.99	1.04	1.10	0.71
Sea state 3	1.00	0.97	0.92	1.00	0.99	0.97

Thus, in conclusion, the exceedance probability curves of the depth-integrated force follow the exceedance probability for the crest. When the wind is applied above the wavefield, the forces are affected, and as expected, the largest variation is seen at the tail.

In the next figures, Figure 41 and Figure 42, the exceedance probability for the line force at two depths is shown. As the vertical direction is time-dependent, an interpolated function of the line force is created at each time step. Here cubic spline interpolation is used, as done in \citet{PhDSchl}. The function is then evaluated at the same z value for all time steps, making it possible to find the maximum line force at specific depths of each wave.

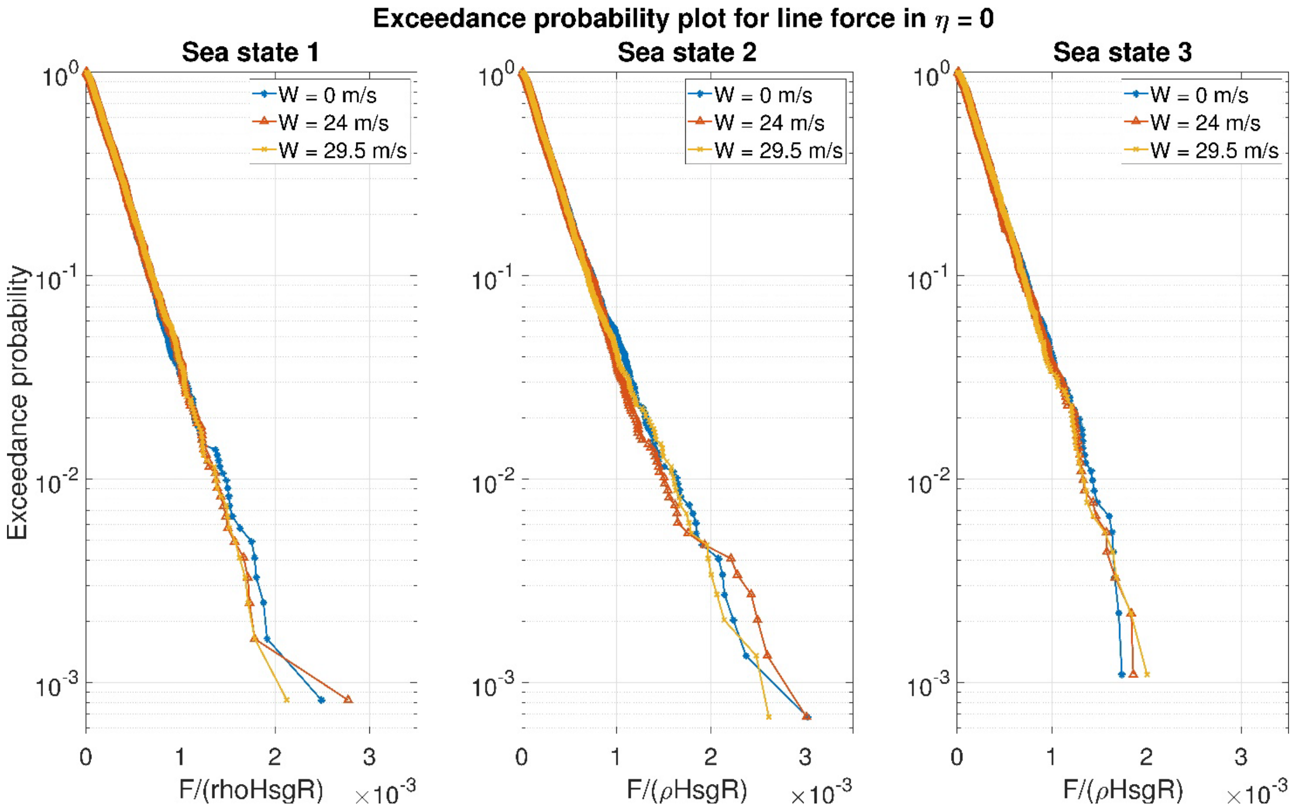

Figure 41: Line force at η = 0 m.

The value of η_{max} for each of the different simulations can be found in Table 16.

Table 16: η_{max} found within the different sea states.

	Highest surface elevation [m]		
	W = 0 m/s	W = 24 m/s	W = 29.5 m/s
Sea state 1	11.65	15.02	12.94
Sea state 2	9.23	9.18	8.00
Sea state 3	10.09	9.53	9.27

The line force found at the mean water level shows a slightly different picture of Sea state 1 compared to the depth-integrated forces, where the line force is decreased when wind is introduced. The tendencies in the line force for Sea state 2 and 3 is comparable to the depth-integrated forces. A possible explanation for the deviation between line force and depth-integrated force for Sea state 1 could be found in the increase of the surface elevation when wind is introduced. Here the maximum surface elevation increased with 28.93 % and 11.07 % for W = 24 m/s and W = 29.5 m/s respectively. When the crest increases, the overall water column above mean water level increases and the particle velocities at mean water level decrease. This could lead to decreased values for force at $\eta = 0$.

Looking at the exceedance probability plot for line force at $0.6{\cdot}\eta_{max}$, Figure 41, the effect of wind in Sea state 1 is seen to have significant impact for both wind speeds, however especially W = 24 m/s is seen to increase the line force greatly. This wind case presents force values well above the case without wind for exceedance probabilities up to as high as $4{\cdot}10^{-2}$. The factor difference for the last three points of the exceedance probability curves can be seen in Table 17. For Sea state 2, the characteristic spike around 10^{-2} is once again observed, just as it was seen for depth-integrated force peaks and crest height. Below this exceedance probability, the curve for W = 0 m/s and W = 24 m/s is seen to follow each other's paths, except for W = 24 m/s having a spike around $4{\cdot}10^{-3}$. The gust wind case lies well below the other two curves, with normalized line force values for the case making up between 72 % - 84 % of the normalized line force of W = 0 m/s.

Table 17:Overview of line force factors for the last three points of the exceedance probability curve relative to the case without wind.

	Factor of line force in $\eta = 0$ compared to W = 0 m/s					
	W = 24 m/s			W = 29.5 m/s		
	3rd last	**2nd last**	**Last**	**3rd last**	**2nd last**	**Last**
Sea state 1	0.92	0.93	0.85	0.91	0.93	0.85
Sea state 2	1.11	1.10	1.00	0.96	1.05	0.86
Sea state 3	1.00	1.08	1.07	1.01	1.07	1.15
	Factor of line force in $\eta = 0.6{\cdot}\eta_{max}$ compared to W = 0 m/s					
Sea state 1	1.27	1.30	1.33	1.10	1.54	1.81
Sea state 2	0.97	0.94	1.03	0.84	0.78	0.72
Sea state 3	1.05	0.90	0.82	1.03	0.88	0.82

The trend of the third sea state for line force in $\eta = 0.6{\cdot}\eta_{max}$ is seen to replicate the exceedance probability curve for depth-integrated force to a high degree. The minor discrepancies lie in a more pronounced variation around exceedance probability of 10^{-2} and a larger variation at the tail. As can be appreciated from Table 17 both cases with wind are seen to only make up 82 % of the normalized line force of the case without wind for the largest force events.

4.4. Summary of results

For the analysis of the large-scale simulations, three sea states were chosen. Sea state 1 and 3 are alike in terms of significant wave height and steepness, whereas Sea state 2 is steeper but with lower significant wave height. The wind is applied at two different wind speeds, 24 m/s and 29.5 m/s. For Sea state 1, the significant wave height, crest and steepness generally increase upon application of wind. Increasing the wind further increases the steepness while the crest and significant wave height do not increase.

Sea state 2 and 3 are initially 20 % and 7 % steeper than Sea state 1. For these initially steeper sea states, the steepness decreases with the introduction of wind, while the number of breaking waves increases. The significant wave height decreases when comparing 0 m/s to 29.5 m/s. Looking at the depth of the sea states compared to the peak wavelength, Sea state 1 and 2 fulfills the condition for deep water, while Sea state 3 only categorizes as intermediate water depth. This can possibly explain some of the differences in the effect of the wind when comparing Sea state 1 and 3. Furthermore, the larger depth in Sea state 1 can partly explain the considerable increase of highest surface elevation of the sea state, compared to Sea state 2 and 3.

No breaking waves could be detected with the breaking criteria of \citet{kjeldsen1979breaking}, which is assumed to be due to the activation value of the breaking filter in OceanWave3D. By counting the waves using the number of times the breaking filter was activated, the overall tendency is that by increasing the wind, the number of breaking waves increased. The number of breaking waves decreased heavily in Sea state

1 when introducing the wind and continued to decline with the gust wind speed. This is the opposite of what was expected. To investigate the matter further, it would be ideal to increase the amount of data being analyzed by running further simulations.

Looking at the wave-induced load upon applying wind, visible changes were seen for Sea state 1 and 2, while Sea state 3 showed little to no change in wave-induced load. The wave-induced load was seen to increase significantly for Sea state 1 when introducing wind with a speed of 24 m/s. Further increasing the wind led to further increases in the load for some of the extreme events, except for line force at $\eta = 0$ m. Looking into the wave-induced load for Sea state 2, an increase can be detected at a specific region in the lower exceedance probabilities. However, further increasing the wind speed decreases the load. The single most extreme force event is not amplified with the effect of wind. This can be explained by the front steepness of the sea state. The ever-increasing Sea state 1 was initially the least steep sea state, thus having a larger potential of becoming steeper as more waves have the potential of building up a steeper wave shape. However, for Sea state 2, the extreme events did not have the same potential to increase the wave shape further. This can be seen by the decrease of steepness in the 100 largest events, where the steepness decreased with 9 % and 5 % for 24 m/s and 29.5 m/s, respectively.

Sea state 3 generally presented minor changes, with only line force at $\eta = 0$ m showing slightly increased force for wind, and line force at $0.6 \cdot \eta_{max}$ showing a decrease in force with the wind. For line force calculations, the line force is estimated with an interpolated function over depth, namely a cubic spline interpolation. This can potentially present some inaccuracies stemming from interpolation errors.

In closing, it is seen that the wind has the potential to increase the wave-induced load, especially in extreme events. However, at certain levels of crest front steepness and wind speeds, the load decreases to similar levels as seen without wind, or in some cases, below. This was seen in the tails of the exceedance probability curves for the depth-integrated force of Sea state 1 and 2. This indicates that a level of initial front steepness exits, which will potentially limit the increase of wave-induced load when applying wind. With the data generated in the works of this thesis, it is observed that the effect of applying the wind is susceptible to the sea states. Sea state 1 and 3 were similar in parameters except for the water depth. However, the results of the simulations and the effect of the wind were different in magnitude in the two sea states. Hence, even though the front steepness of the waves plays a major role in the wind effect on the wave-induced load, the front steepness alone can not explain all trends in the data. By achieving more data, as done in model scale, it could be evaluated whether the extreme events are experiencing large variations or if the trends seen in the present thesis are representative.

5. Conclusion

This thesis has investigated the effect of wind on wave-induced loading using wave kinematics from 2D nonlinear, irregular waves generated by a potential flow model, OceanWave3D.
In the first part of the thesis, the hydrodynamic model within OceanWave3D is validated against experimental results by comparing simulated surface elevation and wave-induced load from simulations to wave gauge and load cell measurements, respectively. It was found that the reference point in the numerical model was shifted downstream compared to the experiments. Based on the exceedance probability curves for crest height and depth-integrated force, the numerical model was validated. Two sea states from the experiments were used in the validation. Here, sea state B was better recreated within the simulations than sea state A. Simulations for sea state A and B were well aligned with experimental measurements without wind. The effect of applying wind was better captured in sea state B than sea state A.

To investigate the phenomenon on large scale, three different sea states were considered for three different wind speeds. Two of the sea states consisted of parameters stemming from recent measurements of extreme waves to recreate these and conduct analysis hereof. The third sea state was a scaled version of sea state B used in model scale. Wind velocities used in simulations were 0 m/s, 24 m/s and a gust wind speed of 29.5 m/s. A study of the numerical domain size was performed to determine the size of the domain. Simulations were run for this purpose and the results were analyzed in both time and frequency domain. This lead to a domain size of {Lx,Ly,Lz} = 14,565 x 1 x 300 m for Sea state 1 and {Lx,Ly,Lz} = 14,565 x 1 x 90 m for Sea state 2 and 3, with a discretization of {Nx,Ny,Nz} = {4501 1,16} for all sea states. The results for the three sea states have been analyzed and compared for simulations resulting in approximately 1,000 waves based on the JONSWAP spectrum for all three sea states for all wind speeds.

Overall, the introduction of wind by means of the modified Jeffreys's sheltering mechanism was shown to influence the wave parameters, such as crest height, front steepness, number of breaking waves, and wave-induced loads. The extreme events were the most affected in all sea states. For Sea state 1, applying the wind increased the crest height and front steepness. By applying the gust wind speed, these parameters were generally further increased. For Sea state 2, an increase in crest height for the extreme events was found, while the front steepness of all events and the 100 largest events decreased. When gust wind was applied, the crest height was decreased compared to a wind speed of 24 m/s, but still increased compared to the case without wind. Further, the front steepness was increased compared to the wind speed of 24 m/s. However, both cases with wind decreased in steepness compared to the case without wind. For Sea state 3, the crest height of the extreme events was slightly decreased when the wind was introduced. When applying gust wind, the results were almost identical to a wind speed of 24 m/s. Comparing the front steepness of the three wind speeds, no significant change was found for any events.

The number of breaking waves were assessed based on the number of times the inherent breaking filter of OceanWave3D was activated. For two out of three sea states, the number of breaking waves increased with the application of wind. Hence, the overall risk of a breaking wave is increased when the wind is introduced. For the depth-integrated force, an increase of the extreme events was found for Sea state 1 for both wind speeds. The largest event increased by 71 % and 26 % for a wind speed of 24 m/s and 29.5 m/s, respectively. At $\eta = 0$, the line force was decreased when wind was applied, whereas the line force at $\eta = 0.6 \cdot \eta_{max}$ was increased.

For Sea state 2, the largest depth-integrated force was almost unchanged by the application of wind, while applying gust wind decreased the largest event. For events at lower exceedance probabilities, a slight increase in depth-integrated force was observed. The line force showed a similar picture, where the introduction of wind increased the line force, while the gust wind, in general, decreased the extreme events for both line forces analyzed. Sea state 3 showed insignificant changes in wave-induced load upon the introduction of wind. Only on the exceedance probability curve for line force in $\eta = 0$ m were the most extreme events slightly increased. The initial front steepness was found to be influential on whether the effect of wind increased or decreased the wave-induced load. With the application of wind, the least steep sea state, Sea state 1, was found to increase significantly in terms of crest height, steepness, and depth-integrated force for the most extreme events. While Sea state 2, which initially was 20 % steeper than Sea state 1, did experience some increase, there was no amplification of the most extreme event.

Reference

[1] Lars German Hagsten, Merle Rianne van Logtestijn, Henning Højgaard Laustsen: ”*Point foundation. Upper and lower bound solution for point load and upper bound solution for distributed load*”. Proceedings of the Danish Society for Structural Science and Engineering. No. 2, Nov 2022, page 1-14.

[2] M.P. Nielsen & L. C. Hoang: 'Limit Analysis and Concrete Plasticity'. Third edition. 2011. CRC Press

Danish Society for Structural Science and Engineering

Requests for membership of the society are submitted to one of the board members:

Kåre Flindt Jørgensen, Chairman of the Board
NCC Danmark. Mail: karjor@ncc.dk

Andreas Bollerslev, Vice Chair
Niras. Mail: anbo@niras.dk

Kirsten Riis, Secretary
Vejdirektoratet. Mail: kiri@vd.dk

Mikkel Christiansen, Cashier
AB Clausen. Mail: dsby.mc@gmail.com

Gunnar Ove Bardtrum, Board member
BaneDanmark. Mail: goba@bane.dk

Jesper Pihl, Board member
Cowi. Mail: jepi@cowi.dk

Dennis Cornelius Pedersen, Board member
MOE. Mail: dcpe@moe.dk

Jens Henrik Nielsen, Board member
DTU. Mail: jhn@byg.dtu

The purpose of the society is to work for the scientific development of structural mechanics - both theory and construction of all kinds of load-bearing structures - promote interest in the subject, work for a collegial relationship between its practitioners and assert its importance to and in collaboration with other branches of engineering. The purpose is sought realized through meetings with lectures and discussions as well as through the publication of the Proceedings of the Danish Society for Structural Science and Engineering.

Individual members, companies and institutions that are particularly interested in structural mechanics or whose company falls within the field of structural mechanics can be admitted as members.